Gravity, capillary and dilational wave mode resonance at a visco-elastic two-fluid interface

by

Susan Jayne Brown

B.S. Aeronautical and Astronautical Engineering
Purdue University, 1990
M. S. Aeronautical and Astronautical Engineering
Purdue University, 1992
S.M. Civil and Environmental Engineering
MIT, 1996

Submitted to the Department of Civil and Environmental Engineering
in partial fulfillment of the requirements for the degree of

Doctor of Science

at the

MASSACHUSETTS INSTITUTE OF TECHNOLOGY

February 2005

Author .....
Department of Civil and Environmental Engineering
October 4, 2004

Certified by .....
Dick K.P. Yue
Professor of Ocean Engineering
Thesis Supervisor

Certified by .....
Michael S. Triantafyllou
Professor of Ocean Engineering
Thesis Supervisor

Certified by .....
Chiang C. Mei
Professor of Civil and Environmental Engineering
Chairman, Thesis Committee

Accepted by .....
Andrew Whittle
Professor of Civil and Environmental Engineering
Chairman, Department Committee on Graduate Students

Gravity, capillary and dilational wave mode resonance at a visco-elastic two-fluid interface

by

Susan Jayne Brown

Submitted to the Department of Civil and Environmental Engineering
on October 4, 2004, in partial fulfillment of the
requirements for the degree of
Doctor of Science in the field of Hydrodynamics

Abstract

This thesis is a study of first order resonance between gravity, capillary and dilational wave modes. Gravity, capillary and dilational waves, occurring at a visco-elastic interface between two fluids, are different modes described by a single linear dispersion relation. Gravity and capillary modes arise due to the restoring forces of surface tension and gravity and result in oscillatory motions transverse to the surface. The dilational, or Marangoni, modes arise due to the elastic nature of the interface and result in longitudinal motion along the interface.

The visco-elasticity of the interface may be due to the interfacial nature of the two fluids or it may be due to the presence of a monolayer of surfactant, such as a film on the ocean surface. This visco-elasticity affects the interfacial stress balance and is accounted for in the dispersion relation via interfacial rheological parameters.

We described resonance as coalescence of the roots of the dispersion relation in complex frequency and wave number space. We used this description to explain numerical and experimental resonance phenomena noted in previous studies.

We classified some of the roots of the dispersion relation as primarily gravity, capillary or dilational modes. We numerically determined the dependence on interfacial rheology of root coalescence (resonance) and the boundaries of spatial stability of the modes. We used these diagnostic tools to characterize the conditions for both gravity-capillary and capillary-dilational modal resonances.

We developed an inverse method from which interfacial rheological parameters can be determined from experimental measurements of wave number, frequency and spatial damping coefficient. We used this tool to construct the dispersion relation solution space corresponding to experimental conditions to thereby interpret the experimental results. We tested this method on noisy simulated data sets and then applied it to published experimental data sets.

We designed an experimental set-up to measure wave number, spatial damping coefficient, and wave slope data for a $3 - 10$ hertz frequency range of transverse and longitudinal waves in a clean enclosed flume. We used kimball-mounted lasers

whose beams passed through optical glass in the tank and lid to capture transverse wave motion. The experimental conditions included waves traveling on fatty acid monolayers on aqueous solutions and also waves traveling on a visco-elastic fluid at a variety of temperatures. In addition to the wave data we obtained, we also measured in-situ surface tension.

Analyzing the experimental data, we demonstrated the effects of modulation of one wave mode on another. We obtained the rheological parameters for these experimental systems by the inverse method. We used the inverse method to construct the dispersion relation solution space corresponding to the experimental conditions. We used the diagnostic tools for root classification, spatial stability together with a graphical representation of the dispersion relation solution space to understand the physics underlying our experiments.

We demonstrated resonance phenomena experimentally with the wave data from the visco-elastic fluid and confirmed this resonance numerically: gravity – capillary resonance near 4.2 hertz and capillary – dilational resonance near 5.3 hertz as predicted.

Among the applications for the work in this thesis are air-sea gas exchange, chemical engineering manufacturing processes and ocean wave dynamics.

Thesis Supervisor: Dick K.P. Yue
Title: Professor of Ocean Engineering

Thesis Supervisor: Michael S. Triantafyllou
Title: Professor of Ocean Engineering

Acknowledgments

I would like to thank my committee members, Professors Dick Yue, Michael Triantafyllou, Chiang Mei and Howard Brenner, for so graciously giving me their time and insight. A special thanks I give to my co-advisors, Professors Dick Yue and Michael Triantafyllou for their intellectual and emotional support.

I was honored to have a National Defense Science and Engineering Graduate Fellowship through the Department of Defense for my two first years of this work. I would like to thank Professor Chiang Mei for the support of one semester through an Office of Naval Research grant and Dean Ike Colbert for a half term stipend this past spring. I would also like to thank Professor Dick Yue, Professor Patrick Jaillet and Dean Ike Colbert for funding for my final summer, thus allowing me time to finish writing.

Additional funding for my studies came through teaching assistantships and for these I would like to thank: Professors Kim Vandiver; Jerry Milgram; Gareth McKinley, John Heywood and Gang Chen; Steven Crandall and Neville Hogan; Nicolas Hadjiconstantinou; Tom Sheridan and Larry Young; and Ain Sonin.

I gratefully received additional scientific help with measurements from Trevor Ng, Michael Goldsipe and Erik Bock.

Professor Jerry Milgram, Doctor Jim Bales and Doctor Sean McKenna graciously loaned me equipment.

Iason Chatzakis kindly sketched a piece of equipment for me.

Finally, I would like to thank so many people who have meant so much to me while I was here: Rene, Klaus, Analia, Paul, Manuel, Lucas, Diane, Pulcherie, Zaid, Karsten, Yukiko, Jonathan, Johan, Kate, Wing, Luigi, Eileen and Janni, you were my friends and my happiness in my early years here - you made the stuggles more bearable and the joys sweeter. Thank you!

Chrissi, Lin, Susanna, Horacio, Zeina, Daniel, Paul, Frederique, Jonno, Katka, Bettina, Anne-Catrin, Al, Shannon, Tom, Adi, Ben, and Karl - I could not have borne the long mid-thesis hours without your smiles and your wits, your friendship

and encouragement. You were my strength. Thank you!

Adam, Malima, George, George, Janet, Dominique, Lydia, Alexandros, Konstantinos, Iason, Dee, Yannis, Lenka, Aggelos, Fabiola, Mats, Rogelio, Stephen, Tom and Rich you saw me through to the end with encouragement and kindness and deprecating wit and fun!! Thank you!

And those friends who I have known all along - Jim, Ann, Kathy, Kristen, Gina, David, Jimmy, Afedziwa, Lisa and Jill and those who have passed through my life, but I have lost, Bill and Gerald - you are amazing people who I am honored to have in my life! What were you thinking when you chose me?!

There are a few faculty members here who have made my stay here a real pleasure - Ain Sonin, Nicolas Hadjicontantinou, Jerry Milgram, Kim Vandiver, Tom Sheridan and Stephen Crandall. I would like to thank you with my committee members, Dick Yue, Michael Triantafyllou, Howard Brenner and CC Mei for inspiring me to love research.

And then I would like to thank my family: Jack, Karen, John, Stephen, Anna, Ally, Jake, Al, Henrietta, Jack, June, John, Joy, John, Joe, James, Jeff, June, Joe, David, Michael, Fatima, Bill, Alan, Brian, Lisa, Christopher, Ethan, Billy, Donny, Bill, Anne, Van, Gert, Fred, Carolyn, Texie and George and everyone's wives and husbands and children and all of my cousins in my very very large family. Well everyone, I'm finally done!

Contents

List of Figures

List of Tables

Chapter 1

Introduction

This thesis began as a small project to explain some phenomena in published numerical data which had been attributed to capillary-dilational resonance. Capillary and dilational waves are separate modes arising from a single linear dispersion relation at a visco-elastic interface of a two fluid system. These waves had been studied for the last 35 years by physical chemists. Recent numerical studies of the dispersion relation by Earnshaw *et al.* (1991) had shown some interesting behavior of the two modes. Under certain conditions the two modes exhibited simultaneous peaks and troughs in plots of spatial damping coefficients while at other conditions, the two modes appeared to switch character, a phenonmenon which the authors termed 'mode mixing'.

These phenomena were reminiscent of the effects of mode coalescence studied in vibrational systems by one of my thesis supervisors, Professor Michael Triantafyllou. My original project was to apply the complex analysis techniques used by Professor Triantafyllou for vibrational systems to this fluid wave system with the goal of elucidating how mode coalescence (resonance) between the two wave modes would result in the sort of behavior seen in Earnshaw's numerical study. The project was successful and the phenomena were well described by the complex analysis. Furthermore, the project was able to provide analytical conditions necessary for resonance. Quite a few published numerical studies and at least one set of experimental measurements attributed some unusual phenomena to resonance. However, before this project, nobody had ever quantified resonance for capillary and dilational waves. Now, with a

rigorous definition, it was for the first time possible to clarify when it was occuring.

In the process of pursuing this project, I became well acquainted with the dispersion relation describing the two modes and the sorts of applications it was used for. In physical chemistry, this dispersion has largely been used in conjunction with experimentation for the elucidation of surface rheology. Because the fluid interface is visco-elastic, this gives rise to entirely different boundary conditions than are typically studied in hydrodynamics. Both elasticity and surface viscosity are modeled into these conditions. The set of physical parameters describing the surface phenomena are called rheological parameters.

Because surface waves are measurable, the dispersion relation can be used to infer the surface rheology. The dispersion relation is, however, unwieldy. Commonly, researchers would approximate the values of the two roots or assume certain rheological parameters were negligible when trying to estimate other parameters. I realized two things from my work with complex analysis and resonance: these approximations would lose the physics of these waves near resonance events and the dispersion relation solution space appeared to be unique. If the solution space was indeed unique, then it would be possible to create a numerical inverse method using the entire dispersion relation to obtain a complete set of rheological parameters from wave measurements. This inverse method would have two values: first, it would provide a diagnostic tool for chemical engineers to find surface rheology and, second, it would provide me with a tool to study what was physically (and hopefully resonantly) happening with experimental data. The development of this inverse method and it's verification with both numerical and previously published experimental data (Bock, 1987) was published in the Proceedings of the Royal Society of London, Series A (Brown *et al.* 2002).

Although we had seen resonance in at least one numerical (Earnshaw *et al.* 1991) and one experimental (Bock, 1987) study, we had no idea how common it might be in physical systems. That it might be important, however, we knew. Resonant wave interaction has long been looked to as a mechanism for wave attenuation but has always been studied as a third order effect for gravity wave interaction. The dispersion relation for capillary and dilational waves is developed from linearized governing

equations. Capillary-dilational resonance is a first order effect. A substantial amount of research has gone into discovering how slicks at the ocean surface affect energy transport. Of course, these slicks are visco-elastic and give rise to both capillary and dilational wave modes. So, we hoped that by studying capillary-dilational resonance we might gain some insight into what was happening at the ocean surface.

To begin with, I needed to discover what rheological conditions give rise to resonance. This was done numerically by applying the analytical conditions for resonance from the original project. The results were rather interesting and a significant amount of resonant activity was discovered between 3 and 10 hertz for a variety of rheological conditions. Examining the solution space, it was clear that not all of these resonances were between the capillary and dilational modes. The dispersion relation has, in fact, five roots. One of these roots had been previously identified with the capillary mode and the other with the dilational mode. The other three had been considered spurious. While the resonances might not be between capillary and dilational modes, the effect of resonance of one of these 'spurious' roots on the capillary mode is the minima in the group velocity of gravity-capillary waves near 4 hertz.

The discovery of the effect of the 'spurious' roots on physical ones led to the identification of all of the roots as variously gravitational, capillary or dilational in nature. And, the acknowledgment that these various roots may or may not be physical and stable dependent on the rheology and wave conditions led to a numerical study of stability of the various roots and the quantification of this stability based on the rheological parameters.

Armed with the knowledge of how to look at the dispersion relation solution space (complex analytical model), where to look at the dispersion relation solution space (conditions for resonance), when to look at the dispersion relation solution space (conditions for stable roots), and what to look for in the the dispersion relation solution space (which roots corresponded to which wave modes - gravity, capillary or dilational), I then had enough information to try to find resonance experimentally and the ability to interpret the results.

I ran manyy experiments with water and with soluble surfactants before develop-

ing both a good quality experimental set-up and technique for measuring resonance effects. There is not much published wave number and damping coefficient data. I do not doubt that this is because good precision data is difficult to obtain. Eventually I obtained excellent data sets and, with the knowledge acquired from the analytical and numerical studies, I was able to both apply the inverse method and to capture resonance effects at precisely the expected frequency values. I was also able to show modulation between the capillary and dilational wave modes and the appearance of an energy bifurcation around 4 hertz as the primary mode of energy transport passed from the gravity to the capillary and dilational modes.

Thesis contributions

The contributions of this thesis dissertation fall into three categories: explanations of physical phenomena based on previous authors' work; new analysis techniques and new results. For clarity of reading the thesis dissertation, these have been itemized below with directions to the locations of their presentation within the thesis dissertation body.

- Explanations of physical phenomena based on previous authors' work
  - Clarification of the meanings of the rheological parameters used in the derivation of the dispersion relation for gravity, capillary and dilational waves at a visco-elastic two-fluid interface §2.3
  - Mathematical description of interfacial wave mode resonance using complex analysis §4.2.2
  - Mathematical explanation of resonance phenomena noted in previous experimental and numerical studies §4.2.2
- New analysis techniques
  - Inverse method to find surface rheological parameters from surface wave data §6

- New results
  - Identification of separate gravity, capillary and dilational wave modes §3.4
  - Numerically determined parametric bounds of modal stability §3.5
  - Numerically determined identification of and conditions for various modal resonances §4.3
  - Demonstration of effect of resonance on the group velocity, Cg, damping coefficients and energy spectrum §4.4
  - Experimental interfacial wave measurements §5.5
    * fatty acid monlayers on acqueos solutions
    * viscous lubricant
  - Analysis of wave modulation §5.4
  - Application of the inverse method to experimental data - determination of surfactant rheological parameters §6.5
  - Experimental evidence of modal bifurcation §6.5
  - Experimental evidence of resonances §7

Chapter 2

Development of boundary conditions and governing equations

2.1 Introduction

Gravity, capillary and dilational waves are separate wave modes arising from a single linear dispersion relation describing motion at a visco-elastic interface of a two-layer fluid system which may or may not be separated by a monomolecular layer of surfactant. The gravity and capillary modes which result in oscillatory motion normal to the plane of the interface arise due to the restoring forces of gravity and of gravity and surface tension combined, respectively. The dilational, or Marangoni, mode arises due to elasticity at the interface and results in oscillatory motion in the plane of the interface.

Elasticity at the interface may exist due to the presence of a surfactant film, but may also exist due to the diffuse nature of an interface and the relative attractions of the fluid particles in this region. This depends on the nature of bonding between elements of the two fluids. An air-water interface is fairly inelastic while an air-oil interface is quite elastic. All natural fluid interfaces (air-water) have some sort of contamination, whether it be dust, biota, or even an oil spill. Unless the surface is highly turbulent, this contamination forms a visco-elastic film which, in turn, results in dilational wave motion. Thus, all two layer fluid systems are most properly de-

scribed by a full visco-elastic dispersion relation with simplified dispersion relations for gravity waves or for gravity-capillary waves as limiting cases.

This chapter presents the development of the dispersion relation at a visco-elastic interface.

2.2 Literature review

The effect of surface films on water has been known since antiquity. The oldest written observation of the dissipative effect of an oil film on ocean waves was made by Pliny the Elder in AD 77. Pliny accounted both a practice amongst seamen of pouring oil into the sea to calm the waves in storm and that of divers spreading oil at the sea surface to calm the waves and allow more light to penetrate to a greater depth. The earliest known experiments with oil on water were conducted by Benjamin Franklin in 1774. From these experiments, Dr. Franklin conjectured that a mutual repulsion between oil and water would cause a small drop of oil to spread out to a great extent on the surface of a body of water and that this layer of oil would prevent friction between the air and water so that the wind would be unable to produce small waves at the surface.

Capillarity was discovered and described by Leonardo DaVinci in 1490. In 1881, LaPlace provided the accepted mathematical theory of capillary action and called the resultant attraction of particles on the surface of the liquid, surface tension. Lord Kelvin (Thompson, 1871) showed that the small waves studied by Dr. Franklin are mainly governed by surface tension and thus these waves became known as capillary waves. He derived a dispersion relation governing both capillary and gravity waves.

Lamb (1932) extended Kelvin's relation to include the effects of bulk fluid viscosity. Following the works of Reynolds (1880) and Aitken (1883), who noted that the damping of capillary waves by oil on the surface of the water appeared to be due to extensions and contractions of the surface as a result of variation of surface tension, Lamb also considered the effects of variation of surface tension (elasticity) on the surface waves for an inextensible surface and found the effect of elasticity on

the damping rate of capillary waves small in comparison to constant surface tension effects.

Levich (1941) made a much more detailed analysis than Lamb with the same conclusions. Though he noted that the works of Shuleikin (1933) and Mayers and Harkins (1938) suggested that the damping rate of capillary waves should be due to the high viscosity of monolayers, he rejected this claim in favor of the hypothesis that the damping effect of a film must be due to inextensibility. Dorrestein (1951), Hansen and Mann (1964), and van den Tempel and van de Riet (1965) showed that Levich was wrong, that the maximum damping rate of capillary waves would occur for surfaces with extensibility, calculating it to be exactly twice that for an inextensible surface. Based on these findings, Lucassen (1968) developed a general dispersion relation for fluids with a visco-elastic interface and demonstrated that the cyclical elastic motion of the interface results in one of its roots of the dispersion relation corresponding to a dilational wave mode.

The rheological description of the behavior of the surface in terms of elasticity, relaxation and viscosities has also developed over time. The earliest formulation of the dynamics of a Newtonian fluid dependent on interfacial surfactant rheology was given by Boussinesq (1913), and later formalized by Scriven (1960). Lucassen's (1968) dispersion relation initially considered surface tension, elasticity, and dilational viscosity. Goodrich (1981) and Baus (1982) relaxed the restriction of isotropy in the normal direction, resulting in the appearance of two additional surface viscosity coefficients, one normal and one tangential to the plane of the surface.

There has been a great deal of confusion in the literature over the correct meanings of the rheological parameters with several different parameters being referred to by the same name. Great pains were taken with section 2.3.2 to clarify these definitions.

2.3 Dispersion relation governing interfacial wave modes

2.3.1 Development of dispersion relation

We consider an idealized two fluid system whose interface is comprised of a monolayer of surfactant. When the interface of system of this type is disturbed, both primarily transverse (gravity and capillary) and a primarily longitudinal (dilational) wave modes are produced. To investigate these modes, we examined the single dispersion relation which governs all three.

Our development of the dispersion relation is very similar to that of Lucassen-Reynders & Lucassen (1969) incorporating, however, the more general boundary conditions of Goodrich (1981), the parameter conventions of Edwards *et al.* (1991), and the notation of Earnshaw & McLaughlin (1991).

We consider a stable two fluid system with an interface which at rest coincides with the plane $z = 0$ with the $+z$ direction extending into the upper fluid. At this interface are propagated two-dimensional plane waves in the $-x$ direction. When the amplitude of these waves is small, the quadratic terms in the Navier-Stokes equation can be ignored, and the resulting x and z component equations become for the lower fluid, respectively:

$$\rho\frac{\partial v_x}{\partial t} = -\frac{\partial p}{\partial x} + \mu\left(\frac{\partial^2 v_x}{\partial x^2} + \frac{\partial^2 v_x}{\partial z^2}\right), \tag{2.1}$$

$$\rho\frac{\partial v_z}{\partial t} = -\frac{\partial p}{\partial z} + \mu\left(\frac{\partial^2 v_z}{\partial x^2} + \frac{\partial^2 v_z}{\partial z^2}\right) - \rho g \tag{2.2}$$

where $\mathbf{v} = (v_x, v_z)$ is the velocity, p the pressure, μ the viscosity of the fluid, ρ the fluid density and g gravitational acceleration. The subscripts x and z indicate components in these directions. The continuity equation is

$$\nabla \cdot \mathbf{v} = \frac{\partial v_x}{\partial x} + \frac{\partial v_z}{\partial z} = 0. \tag{2.3}$$

Equations (2.1), (2.2) and (2.3) can be solved by considering the velocity field to be the sum of an irrotational field and a divergence free field

$$\mathbf{v} = -\nabla\phi + \nabla \times \psi, \tag{2.4}$$

with, for nearly sinusoidal waves, the potential and stream functions having solutions of the forms

$$\phi = Ae^{kz+i(kx+\omega t)}, \quad \psi = Be^{mz+i(kx+\omega t)}, \tag{2.5}$$

respectively, with

$$m^2 = k^2 + \frac{i\omega\rho}{\mu}. \tag{2.6}$$

The quantities k, m and ω are allowed to be complex with $Re(k)$ and $Re(\omega)$ denoting the wavenumber and frequency of the wavemodes and $Im(k)$ and $Im(\omega)$ denoting spatial and temporal wavemode damping. We require that $Re(k) > 0$ and $Re(m) > 0$ so that all motion will vanish as $z \to -\infty$. From (2.4), we find the velocity and pressure components

$$\begin{aligned} v_x &= \left[-ikAe^{kz} - mBe^{mz}\right] e^{i(kx+\omega t)}, \\ v_z &= \left[-kAe^{kz} + ikBe^{mz}\right] e^{i(kx+\omega t)}, \\ p &= p_o - \rho g z + i\omega\rho Ae^{kz}e^{i(kx+\omega t)}. \end{aligned} \tag{2.7}$$

At the surface, the velocity components can be written in terms of vertical (normal) and horizontal (tangential) displacements, ζ and ξ, of a surface element from equilibrium. To the leading order of a small amplitude approximation:

$$v_z = \frac{\partial\zeta}{\partial t}, \quad v_x = \frac{\partial\xi}{\partial t} \tag{2.8}$$

which can be integrated to give

$$\zeta = \frac{-kA + ikB}{i\omega} \cdot^{i(kx+\omega t)}, \quad \xi = \frac{-ikA - mB}{i\omega} \cdot^{i(kx+\omega t)} . \tag{2.9}$$

By similar development, in the upper fluid (denoted by primed variables) we find

$$\phi' = Ae^{kz+i(kx+\omega t)}, \quad \psi' = Be^{m'z+i(kx+\omega t)},$$
$$m'^2 = k^2 + \frac{i\omega\rho}{\mu}, \tag{2.10}$$

and

$$v'_x = \left[ikA'e^{-kz} + m'e^{-m'z}\right] e^{i(kx+\omega t)},$$
$$v'_z = \left[+kA'e^{kz} + ikB'e^{-m'z}\right] e^{i(kx+\omega t)}, \tag{2.11}$$
$$p' = p'_o - \rho' gz + i\omega\rho' A'e^{-kz}e^{i(kx+\omega t)} \tag{2.12}$$

where $Re(m') > 0$ so that all motion will vanish as $z \to 0$.

At the interface between two fluids, we require that momentum be balanced and that there be no discontinuity in the velocity field. Here our formulation departs from that of Lucassen & Lucassen-Reynders (1969) insomuch as we utilize the more general momentum balance expressions of Goodrich (1981):

$$\frac{\partial \sigma_D}{\partial x} + (\mu - \mu')\frac{\partial^2 \zeta}{\partial t \partial x} + \mu' \frac{\partial v'_x}{\partial z} - \mu \frac{\partial v_x}{\partial z} + (\kappa + \eta)\frac{\partial^2 v_x}{\partial z^2} = 0, \tag{2.13}$$
$$\left(\sigma_D + \eta_N \frac{\partial}{\partial t}\right)\frac{\partial^2 \zeta}{\partial x^2} + p + p' - 2(\mu' - \mu)\frac{\partial v_x}{\partial x} = 0, \tag{2.14}$$

The parameters η_N and η are surface shear viscosities normal and tangential, respectively, to the interface, κ a surface dilational viscosity tangential to the interface and σ_D the surface tension of a deformed interface:

$$v_x = v'_x, v_z = v'_z \tag{2.15}$$

applied on $z = 0$ to the leading order.

The gradient of surface tension is commonly expressed in terms of a viscoelastic response function

$$\frac{\mathrm{d}\sigma_D}{\mathrm{d}x} = \frac{\mathrm{d}\sigma_D}{\mathrm{d}\ln A}\frac{\mathrm{d}\ln A}{\mathrm{d}x} = \frac{\mathrm{d}\sigma_D}{\mathrm{d}\ln A}\frac{\mathrm{d}^2\xi}{\mathrm{d}x^2} = \varepsilon\frac{\mathrm{d}^2\xi}{\mathrm{d}x^2} \tag{2.16}$$

where A is the area of a fluid element at the surface, and ε is the dilational modulus.

This is somewhat more obvious if we consider that the surface tension is dependent on the amount of stretching of the interface and can be expanded as follows (Hansen & Ahmad 1971):

$$\sigma_D = \sigma_o + \varepsilon\frac{\partial s}{\partial x} + \varepsilon_2\left(\frac{\partial s}{\partial x}\right)^2 + \cdots \tag{2.17}$$

where σ_o is the surface tension of the unstretched surface (static surface tension) and

$$s = \int_0^{x+\xi}\left(1+\frac{\partial\zeta}{\partial x}\right)^{1/2} dx, \tag{2.18}$$

is the arc length of an element of surface that has been displaced from $(x,0)$ to $9x+\xi,\zeta)$. for small amplitude waves, $\partial s/\partial x = \partial\xi/\partial x$ to the leading order and thus $\partial\sigma_D/\partial x = \varepsilon\partial^2\xi/\partial x^2$.

When the surface experiences a sinusoidally oscillating dilation, the dilational modulus can be represented as a complex parameter (Edwards *et al.* 1991),

$$\varepsilon = |\varepsilon|e^{i\theta} = \varepsilon_o + i\varepsilon'' = \varepsilon_o + i\omega\varepsilon', \tag{2.19}$$

whose phase, θ, represents the phase lag between the stretching of the area of a surface element, δA, and a corresponding change in the surface tension, σ_D. The real part of the dilational modulus, ε_o, is referred to as the dilational elasticity and the imaginary part, ε'', as the relaxational elasticity.

We incorporate (2.3), (2.15), (2.16), (2.17), (2.19) into the momentum balance

equations such that

$$[\varepsilon_o + i\omega(\varepsilon' + \kappa + \eta)]\frac{\partial^2 \xi}{\partial x^2} + (\mu' - \mu)\left(\frac{\partial v_x}{\partial z} + \frac{\partial v_z}{\partial x}\right) = 0, \tag{2.20}$$

$$(\sigma_o + i\omega\eta_N)\frac{\partial^2 \zeta}{\partial x^2} + p - p' + 2(\mu' - \mu)\frac{\partial v_x}{\partial z} = 0. \tag{2.21}$$

Not that σ_o has replaced σ_D and $i\omega\eta_N$ replaced $\eta_N \partial\zeta/\partial t$ in (2.21). By making a change of notation,

$$\epsilon = \epsilon_o + i\omega\epsilon' = \varepsilon_o + i\omega(\varepsilon' + \kappa + \eta), \tag{2.22}$$

$$\sigma = \sigma_o + i\omega\sigma' = \sigma_o + i\omega\eta_N, \tag{2.23}$$

we arrive at the same form of the boundary conditions as Lucassen & Lucassen-Reynders (1969) with, however, important distinctions in the meanings of the parameters. Both σ and ϵ are now complex and incorporate viscous as well as viscoelastic effects. The real part of ϵ, ϵ_o, is the dilational elasticity, while the imaginary part is the product of frequency and ϵ', an apparent surface viscosity combining relaxational, dilational and shearing effects (Edwards *et al.* 1991). The real part of σ, σ_o, is the static surface tension and the imaginary part is the product of frequency and surface normal shear viscosity. The simple complex forms of $\sigma = \sigma_o + i\omega\sigma'$ and $\epsilon = \epsilon_o + i\omega\epsilon'$ make use of the notation of Earnshaw *et al.* (1988) and Earnshaw & McLaughlin (1991), who first used a fully complex form of σ as well as ϵ in their calculations. The authors identified σ' with surfaced shear viscosity transverse to the surface, but ϵ' only as a quantity affecting surface dilation and did not include the relaxational and shearing effects in the more explicit expression given above.

Substituting (2.22) and (2.23), together with the velocity components for the upper and lower fluids adn the expressions given for the displacements ζ and ξ, into (2.15), (2.20) and (2.21), we obtain

$$\left[-i\omega\rho - 2\mu k^2 + \frac{i\sigma k^3}{\omega} + \frac{i\rho g k}{\omega}\right] A + \left[i\omega\rho' + 2\mu' k^2 + \frac{i\rho' g k}{\omega}\right] A'$$

$$+\left[2i\mu km+\frac{\sigma k^3}{\omega}+\frac{\rho gk}{\omega}\right]B+\left[2i\mu' km'-\frac{\rho' gk}{\omega}\right]B'=0, \tag{2.24}$$

$$\left[-2i\mu k^2-\frac{\epsilon k^3}{\omega}\right]A+\left[-2i\mu' k^2\right]A'$$

$$+\left[-mu(k^2+m^2)+\frac{i\epsilon k^2 m}{\omega}\right]B+\left[\mu'(k^2+m'^2)\right]B'=0, \tag{2.25}$$

$$ikA-ikA'+mB+m'B'=0, \tag{2.26}$$

$$A+A'-iB+iB'=0. \tag{2.27}$$

A nontrivial solution to these equations can only be found if the determinant of the coefficients is zero. This results in the well known dispersion relation (Lucassen-Reynders & Lucassen, 1969):

$$\Delta=\left[\mu(k-m)-\mu'(k-m')\right]^2+E\cdot S=0, \tag{2.28}$$

$$E=\frac{\epsilon k^2}{\omega}+i\left[\mu(k+m)+\mu'(k+m')\right],$$

$$S=\frac{\sigma k^2}{\omega}+i\left[\mu(k+m)+\mu'(k+m')\right]+\frac{g(\rho-\rho')}{\omega}-\frac{\omega(\rho+\rho')}{k}$$

2.3.2 Boundary conditions at a visco-elastic interface

Surface tension effects

Let the surface of separation between two fluids undergo an infinitesimal displacement, $\delta\zeta$.

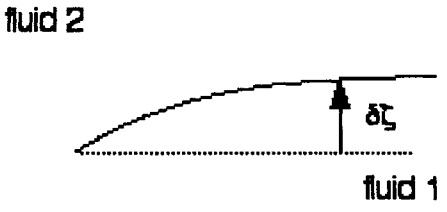

Figure 2-1: Slightly deformed two-fluid interface

The total work, δR done in displacing the surface (neglecting inertial effects) is the sum of pressure, p, work done to change the volumes of the two separated media plus the work connected with the change in surface area, δf.

$$\delta R = -\int (p_1 - p_2)\,\delta\zeta\; df + \sigma\delta f \tag{2.29}$$

The coefficient σ is termed the surface tension coefficient. In thermodynamic equilibrium, δR is zero.

Let $z = \zeta(x)$ be the equation of the surface. An element of surface area can then be represented in terms of an arc length extended a unit distance in the y-direction:

$$f = \int \left[1 + \left(\frac{\partial\zeta}{\partial x}\right)^2\right]^{1/2} dxdy \tag{2.30}$$

If ζ is everywhere small, then

$$f \approx \int \left[1 + \frac{1}{2}\left(\frac{\partial\zeta}{\partial x}\right)^2\right] dxdy \tag{2.31}$$

and the variation, δf, is

$$\delta f = \int \left[\frac{\partial\zeta}{\partial x}\frac{\partial\delta\zeta}{\partial x}\right]\; dxdy. \tag{2.32}$$

Integrating by parts we find

$$\delta f = -\int \frac{\partial^2\zeta}{\partial x^2}\;\delta\zeta\; dxdy. \tag{2.33}$$

Substituting (2.33) into (2.29), we obtain

$$0 = \int \left\{-(p_1 - p_2) - \sigma\frac{\partial^2\zeta}{\partial x^2}\right\}\delta\zeta\; dxdy, \tag{2.34}$$

or,

$$(p_1 - p_2) = -\sigma \frac{\partial^2 \zeta}{\partial x^2}. \tag{2.35}$$

Viscous stress balance for an undeformed fluid interface

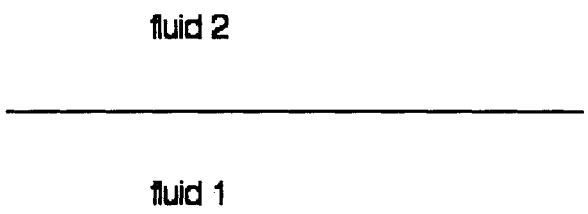

Figure 2-2: Undeformed interface between two viscous fluids. The symbols τ and p indicate interfacial and bulk stresses respectively.

At an undeformed interface between two fluids, the normal and tangential stresses, p_{ik}, must be balanced:

$$\begin{aligned} p_{2_{zz}} - p_{1_{zz}} &= 0 \\ p_{2_{zx}} - p_{1_{zx}} &= 0. \end{aligned} \tag{2.36}$$

These stresses have the form

$$p_{ik} = -\delta_{ik} p + p'_{ik} \tag{2.37}$$

where p'_{ik} is the viscous stress tensor. Furthermore, we require the velocity field to be continuous at the interface:

$$v_{1_x} = v_{2_x} \quad v_{1_z} = v_{2_z}. \tag{2.38}$$

Deformed viscous interface

If we deform the interface between two viscous fluids then, as in section 2.3.2, surface tension effects enter into the stress balance and equations (2.40) become

$$\begin{aligned} p_{2_{zz}} - p_{1_{zz}} + \sigma \frac{\partial^2 \zeta}{\partial x^2} &= 0, \\ p_{2_{zx}} - p_{1_{zx}} &= 0. \end{aligned} \tag{2.39}$$

Deformed viscous surface with surface tension gradient

If the surface tension varies over the surface, $\sigma(x)$, then an additional term is added to the tangential stress condition:

$$\begin{aligned} p_{2_{zz}} - p_{1_{zz}} + \sigma \frac{\partial^2 \zeta}{\partial x^2} &= 0, \\ p_{2_{zx}} - p_{1_{zx}} + \frac{\partial \sigma}{\partial x} &= 0. \end{aligned} \tag{2.40}$$

Boundary conditions at a viscous interface of finite width separating two viscous fluids

Let us consider two viscous bulk fluids separated by a transition region of finite width which we call the interfacial region. We consider a fluid element situated in the interfacial region with upper and lower boundaries at the edge of the two bulk fluids. Viscous stresses will act on this element as pictured in figure 2-3.

The stresses on the upper and lower faces of the fluid element, denoted by p's are exerted by the upper and lower bulk fluids while the stresses on the sides of the element, denoted by τ's, are interfacial stresses which we assume to have the form

$$\tau_{ik} = \tau'_{ik} \tag{2.41}$$

which assumes that the only contribution of these stresses is viscous.

For a small ζ,

$$\tau_{tt} \approx \tau_{xx}, \ \tau_{tn} \approx \tau_{xz}, \ p_{nn} \approx p_{zz}, p_{nt} \approx p_{zx} \tag{2.42}$$

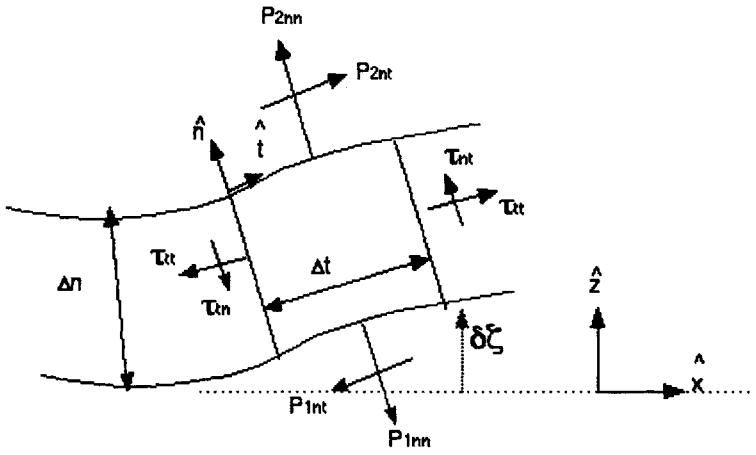

Figure 2-3: Deformed interface of finite width between two viscous fluids

$$\Delta t \approx \Delta x \quad \Delta n \approx \Delta z \tag{2.43}$$

The net forces due to the interfacial stresses are:

$$\begin{aligned}
\left(\tau_{xx}|_{x+\Delta x} - \tau_{xx}|_x\right) \Delta z \Delta y &= \frac{\partial \tau_{xx}}{\partial x} \Delta x \Delta z \Delta y = \frac{\partial \tau_{xx}}{\partial x} l \Delta x \Delta y, \\
\left(\tau_{xz}|_{x+\Delta x} - \tau_{xz}|_x\right) \Delta z \Delta y &= \frac{\partial \tau_{xz}}{\partial x} \Delta x \Delta z \Delta y = \frac{\partial \tau_{xz}}{\partial x} l \Delta x \Delta y,
\end{aligned} \tag{2.44}$$

where $l = \Delta z$ is the width of the interface.

Incorporating the interfacial stresses into the stress balance in equations (2.40), we have:

$$\begin{aligned}
p_{2_{zz}} - p_{1_{zz}} + \frac{\partial \tau_{xz}}{\partial x} + \sigma \frac{\partial^2 \zeta}{\partial x^2} &= 0 \\
p_{2_{zx}} - p_{1_{zx}} + \frac{\partial \tau_{xx}}{\partial x} + \frac{\partial \sigma}{\partial x} &= 0.
\end{aligned} \tag{2.45}$$

A condition must also be placed on the velocity field at the interface. As the width of the interface is small compared to the vertical extents of the two bulk fluids, we will require that the velocity field be continuous between the two bulk fluids with no apparent jump across the interface so that

$$v_{1_x} = v_{2_x} \quad v_{1_z} = v_{2_z}. \tag{2.46}$$

Thus, the interior of the interfacial region will support no vertical velocity gradients, and

$$\frac{\partial v_x}{\partial z} = 0 \quad \frac{\partial v_z}{\partial z} = 0 \tag{2.47}$$

within this region.

Forms of the viscous stress tensors

The bulk viscous stress tensor The are three conditions which must be met by the viscous stress tensor:

- Viscous stresses, p'_{ik}, arise due to internal friction resulting from velocity variation between different parts of the bulk fluid. Thus the viscous stresses must be independent of the velocity itself and rely only on its spatial derivatives, $\partial^n v_i / \partial {x_k}^n$.

- Viscosity is important for slowly moving fluids. In such cases momentum transfer is considered linear, relying only on the first order derivatives of the velocity. As momentum transfer is linear, then so too is viscous stress considered.

- In uniform rotation, there can be no friction between adjacent fluid elements and thus viscous stresses, p'_{ik}, must disappear.

Meeting the three above conditions, we find that p'_{ik} must contain only combinations of the form:

$$\frac{\partial v_i}{\partial x_k} + \frac{\partial v_k}{\partial x_i}. \tag{2.48}$$

After a little bit of manipulation, we obtain the standard form of the viscous stress tensor in an isotropic fluid:

$$p'_{ik} = \mu \left(\frac{\partial v_i}{\partial x_k} + \frac{\partial v_k}{\partial x_i} - \frac{2}{3} \delta_{ik} \frac{\partial v_l}{\partial x_l} \right) - \mu^* \delta_{ik} \frac{\partial v_l}{\partial x_l} \tag{2.49}$$

where μ, μ^* are called the first and second coefficients of viscosity, respectively. In an isotropic fluid, as was assumed, μ and μ^* must be scalars.

For an incompressible fluid the second coefficient of viscosity is disregarded. In cartesian coordinates, we have:

$$\begin{aligned} p'_{1_{zz}} &= 2\mu_1 \left(\frac{\partial v_z}{\partial z}\right) \quad p'_{2_{zz}} = 2\mu_2 \left(\frac{\partial v_z}{\partial z}\right) \\ p'_{1_{zx}} &= \mu_1 \left(\frac{\partial v_z}{\partial x} + \frac{\partial v_x}{\partial z}\right) \quad p'_{2_{zx}} = \mu_2 \left(\frac{\partial v_z}{\partial x} + \frac{\partial v_x}{\partial z}\right) \end{aligned} \tag{2.50}$$

where subscripts refer to the two bulk fluids.

The interfacial viscous stress tensor In the interfacial region, similar conditions to those outlined for the bulk fluids apply to the viscous stress tensor:

- The viscous stresses are independent of the velocity and rely only on its spatial derivatives, $\partial^n v_k / \partial x_k^n$.
- Momentum transfer, and thus viscous stress is considered linear, relying only of the first order derivatives of the velocity.

Meeting the above conditions, we assume that τ'_{ik} has the form:

$$\alpha^i_{ik} \frac{\partial v_i}{\partial x_k} + \alpha^i_{ki} \frac{\partial v_k}{\partial x_i}. \tag{2.51}$$

Now we come to the third condition:

- The interfacial region may be isotropic in the "plane" of the surface, but it cannot be considered so in the direction normal to the surface. This anisotropy may arise from a transition in density between the two fluids or the presence of a surfactant material. Surfactant materials are surface acting precisely because of a preferred orientation at the surface with one end of the molecule 'fluid 1' - phyllic and the other 'fluid 2' - phobic. This preferred orientation creates a normal anisotropy. Given this anisotropy, we can at most say that in a uniform

rotation of the fluid around the surface normal, the interfacial viscous stress tensor must vanish.

This results in viscous shear stresses of the form:

$$\tau'_{ik} = \alpha^i_{ik}\frac{\partial v_i}{\partial x_k} + \alpha^i_{ki}\frac{\partial v_k}{\partial x_i} \quad i,k = t,y \tag{2.52}$$

$$\tau'_{in} = \alpha^i_{ni}\frac{\partial v_n}{\partial x_i} \tag{2.53}$$

$$\tau'_{ni} = \alpha^n_{ni}\frac{\partial v_n}{\partial x_i} \tag{2.54}$$

$$\tau'_{nn} = 2\alpha^n_{nn}\frac{\partial v_n}{\partial x_n} \tag{2.55}$$

As the interfacial region can support no vertical (normal) stress gradients,

$$\frac{\partial v_n}{\partial x_n} = 0 \quad \frac{\partial v_i}{\partial x_n} = 0 \tag{2.56}$$

we have:

$$\tau'_{ik} = \alpha^i_{ik}\frac{\partial v_i}{\partial x_k} + \alpha^i_{ki}\frac{\partial v_k}{\partial x_i} \quad i,k = t,y \tag{2.57}$$

$$\tau'_{in} = \alpha^i_{ni}\frac{\partial v_n}{\partial x_i} \tag{2.58}$$

$$\tau'_{ni} = \alpha^n_{ni}\frac{\partial v_n}{\partial x_i} \tag{2.59}$$

$$\tau'_{nn} = 0. \tag{2.60}$$

For our stress balance with small ζ, in cartesian coordinates we have:

$$\tau'_{xx} = 2\alpha^x_{xx}\left(\frac{\partial v_x}{\partial x}\right)$$

$$\tau'_{xz} = \alpha^x_{xx}\left(\frac{\partial v_z}{\partial x}\right) \tag{2.61}$$

Stress balance across the interfacial region

Incorporating the explicit forms of the viscous stress tensors from (2.50) and (2.61) into the stress balance of (2.45) we arrive at

$$\begin{aligned} -p_2 + 2\mu_2\left(\frac{\partial v_z}{\partial z}\right) + p_1 - 2\mu_1\left(\frac{\partial v_z}{\partial z}\right) + l\alpha^x_{xz}\left(\frac{\partial v_z}{\partial x}\right) + \sigma\frac{\partial^2\zeta}{\partial x^2} = 0, \\ \mu_2\left(\frac{\partial v_z}{\partial x} + \frac{\partial v_x}{\partial z}\right) - \mu_1\left(\frac{\partial v_z}{\partial x} + \frac{\partial v_x}{\partial z}\right) + 2l\alpha^x_{xx}\left(\frac{\partial v_x}{\partial x}\right) + \frac{\partial\sigma}{\partial x} = 0. \end{aligned} \tag{2.62}$$

At an air-water interface, the viscous stresses exerted by the upper fluid become negligible compared to those exerted by the lower fluid and the boundary conditions become

$$p - 2\mu\frac{\partial v_z}{\partial z} + l\alpha^x_{xz}\left(\frac{\partial v_x}{\partial x}\right) + \sigma\frac{\partial^2\zeta}{\partial x^2} = 0, \tag{2.63}$$

$$-\mu\left(\frac{\partial v_z}{\partial x} + \frac{\partial v_x}{\partial z}\right) - \mu_1\left(\frac{\partial v_z}{\partial x} + \frac{\partial v_x}{\partial z}\right) + 2l\alpha^x_{xx}\left(\frac{\partial v_x}{\partial x}\right) + \frac{\partial\sigma}{\partial x} = 0. \tag{2.64}$$

where the subscripts on the variables pertaining to the lower fluid have been dropped.

The gradient of surface tension is commonly expressed interms of a viscoelastic response function

$$\frac{\mathrm{d}\sigma}{\mathrm{d}x} = \frac{\mathrm{d}\sigma}{\mathrm{d}\ln A}\frac{\mathrm{d}\ln A}{\mathrm{d}x} = \frac{\mathrm{d}\sigma}{\mathrm{d}\ln A}\frac{\partial^2\xi}{\partial x^2} = \varepsilon\frac{\partial^2\xi}{\partial x^2} \tag{2.65}$$

where A is the area of a fluid element at the surface, ε is the dilational modulus, and ξ is the displacement of a surface element in the x-direction from equilibrium.

If we also replace the interfacial viscous shear stress coefficients

$$l\alpha^x_{xx} = \eta_N \tag{2.66}$$

$$2l\alpha^x_{xx} = \kappa + \eta \tag{2.67}$$

then we arrive at the form of the boundary conditions (Goodrich 1981) used in the

derivation of the dispersion relation, equation 2.28, for our work:

$$p - 2\mu\frac{\partial v_z}{\partial z} + \eta_N\left(\frac{\partial v_z}{\partial x}\right) + \sigma\frac{\partial^2\zeta}{\partial x^2} = 0 \tag{2.68}$$

$$-\mu\left(\frac{\partial v_x}{\partial z} + \frac{\partial v_z}{\partial x}\right) + (\kappa+\eta)\left(\frac{\partial v_x}{\partial x}\right) + \varepsilon\frac{\partial^2\xi}{\partial x^2} = 0. \tag{2.69}$$

Chapter 3

Roots of the dispersion relation - gravity, capillary and dilational wave modes

3.1 Introduction

Dispersion relations relate frequency and wave number with respect to the various physical parameters describing the system in complex polynomials. The roots of these polynomials represent the various wave modes. Three dispersion relations describing wave motion at a fluid-air interface are studied in this chapter: Lucassen's relation for a visco-elastic interface, Lamb's relation for non-visco-elastic interface with a viscous bulk fluid and Kelvin's relation for a non-visco-elastic interface with an inviscid bulk fluid. Both Lamb's and Kelvin's dispersion relations are simplifications of Lucassen's relation and are helpful in elucidating the behavior and interaction of the various wave modes.

This chapter discusses the roots of the three polynomial dispersion relations, the identification of these roots with various wave modes and the conditions for their physicality and stability.

3.2 Expansions of the dispersion relations.

3.2.1 Lucassen's relation

Lucassen's dispersion relation,

$$\Delta = [\mu(k-m)]^2 + E \cdot S = 0, \tag{3.1}$$

$$E = \frac{\epsilon k^2}{\omega} + i\mu(k+m),$$

$$S = \frac{\sigma k^2}{\omega} + i\mu(k+m) + \frac{g\rho}{\omega} - \frac{\omega\rho}{k} \tag{3.2}$$

with

$$\sigma = \sigma_0 + i\omega\sigma'$$

$$\epsilon = \epsilon_0 + i\omega\epsilon' \tag{3.3}$$

is a complex polynomial with eight variables $(\omega, k, \epsilon_0, \epsilon', \sigma_0, \sigma', \mu, \rho, g)$. Both k and ω are complex. The factor m

$$m^2 = k^2 + \frac{i\omega\rho}{\mu}. \tag{3.4}$$

necessitates an expansion of Δ so that polynomials with integer powers for k and ω can be obtained. The resulting $\Delta_{expansion}$ is 10th order in k and 8th order in ω.

The expansion in m

$$(Am^2 + Bm + C)(Am^2 - Bm + C) = 0 \tag{3.5}$$

produces ten roots for a polynomial in k and eight for a polynomial in ω ,respectively. Five of the k-roots and four of the ω-roots satisfy the original dispersion relation

$$\Delta = Am^2 + Bm + C = 0 \tag{3.6}$$

with $Re(m) > 0$. The additional five k-roots and four ω-roots occur for $Re(m) < 0$,

satisfy

$$A|m|^2 - B|m| + C = 0, \tag{3.7}$$

are spurious, and may be discarded.

3.2.2 Lamb's relation

A simplification of Lucassen's relation results from the assumption that elasticity is negligible. The dispersion relation, without terms proportional to $\epsilon = \epsilon_o + i\omega\epsilon'$, reduces to

$$\omega^2 + 4\left(\frac{\mu}{\rho}\right)^2 k^2 m\,(m-k) = gk + \frac{\sigma k^3}{\rho} \tag{3.8}$$

When expanded in m this relation is 8th order in k and 4th order in ω. Four k-roots and two ω-roots of $\Delta_{Lamb_{expansion}}$ satisfy Δ_{Lamb} for $Re(m) > 0$.

3.2.3 Kelvin's relation

A further simplification, that viscous effects are negligible results in Kelvin's relation:

$$\omega^2 = gk + \frac{\sigma k^3}{\rho} \tag{3.9}$$

This relation is 3rd order in k and 2nd order in ω and requires no expansion in m.

3.3 Admissible solutions

Of the five roots in k of (3.2) which satisfy $Re(m) > 0$, admissibility is determined by

$$Real(k) > 0, \tag{3.10}$$

and stability by

$$Imag(k) < 0, \tag{3.11}$$

(for waves travelling in the $-x$ direction). This follows from the assumption in deriving the dispersion relation that the potential function has the form

$$\psi = e^{kz} e^{i(kx+\omega t)}. \tag{3.12}$$

Depending on the values of the rheological and bulk parameters, $(\epsilon_o, \epsilon', \sigma_o, \sigma', \rho, g, \mu)$, each of the five roots can be admissible.

3.4 Identification of the roots of the dispersion relation

The roots of Kelvin's, Lamb's and Lucassen's dispersion relations can be variously identified with three physical modes: gravity (gravity-capillary), capillary and dilational waves. We will later see in section 4.4 that gravity and capillary (or gravity-capillary and capillary) waves are two separate modes which resonate near 4 Hertz.

Gravity-capillary modes can be easily identified as gravity modes below 4 Hertz by their adherence to the dispersion relation for deep water gravity waves,

$$\omega^2 = kg. \tag{3.13}$$

Above this frequency, this mode bifurcates into two typically non-admissible roots ($Re(k) > 0$) which adhere to Kelvin's relation for capillary waves. These modes are marked in red in figure 3-1. They follow the $\omega^2 = kg$ curve below 4 hertz (pictured in magenta circles) and drop down and follow the lower $\omega^2 = \sigma k^3/\rho$ curves above 4 hertz (pictured in yellow diamonds). The nature of the bifurcation of this mode from a physical gravity to two non-physical "capillary" modes will be made clear in section 4.3. For ease of discussion, this mode will simply be referred to as a gravity mode as

it only has physical character when it behaves like a gravity wave.

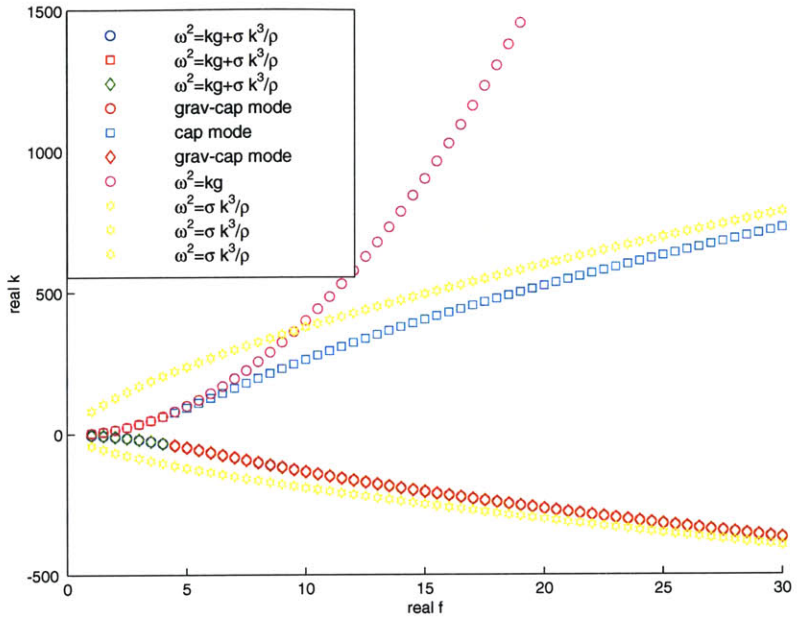

Figure 3-1: A comparison between modes of Kelvin's dispersion relation, $\omega^2 = kg + \sigma k^3/\rho$, the modes of the deep water gravity-wave dispersion relation, $\omega^2 = kg$, and the modes of the deep water capillary dispersion relation, $\omega^2 = k^3/\rho$.

The capillary mode can be identified above 4 Hertz by its asymptotic approach to the physical root ($Re(k) > 0$) of Kelvin's relation for increasing frequency in the absence of the the gravity term,

$$\omega^2 = \frac{\sigma k^3}{\rho}. \tag{3.14}$$

Below four Hertz, this mode bifurcates into two typically non-admissible $Re(k) < 0$ modes. The capillary modes are marked my blue, green and cyan in figure 3-1. The dispersion relation roots for expression 3.14 are marked by yellow pentagons.

The dilational modes are dependent on elasticity, ϵ, and can be identified by varying this parameter as in figure 3-2. One of these modes tends to be both admissible $Re(k) > 0$ and stable $Im(k) < 0$ above approximately 4-6 Hertz.

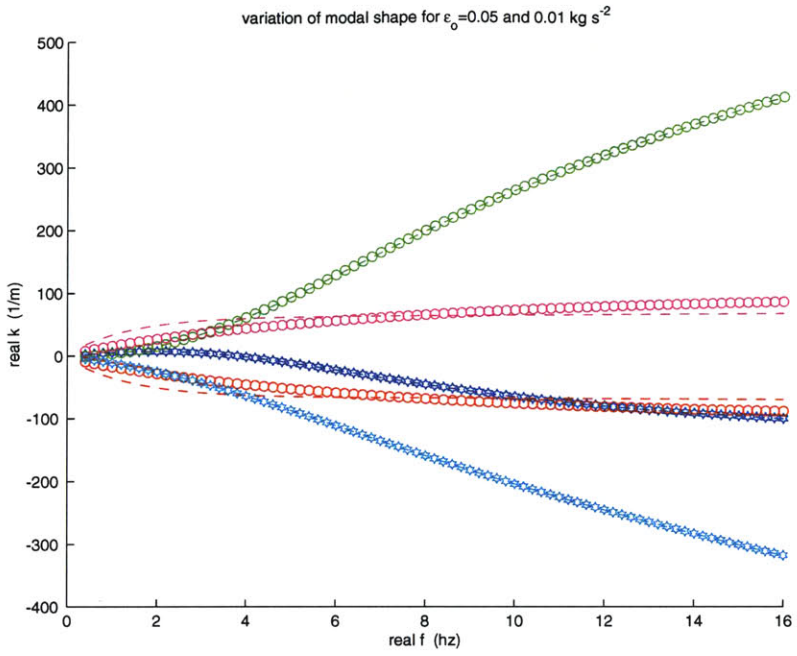

Figure 3-2: A comparison between modes from Lucassen's dispersion relation for $\epsilon_o = 0.05$ and 0.01 kg s^{-2}. The magenta and red modes, which are dependent on ϵ, can be identified as the dilational modes.

3.5 How many admissible modes can coexist?

Lucassen's dispersion relation has five roots corresponding variously to gravity, capillary and dilational modes. The admissibility and stability (existence) of these modes depends on the surface rheology. Lucassen (1969) analytically showed that in the limits of zero (clean surface) and infinite elasticities, only the capillary mode can exist. He predicted that the dilational mode would exist whenever the dilational modulus, ϵ had a finite value.

To get a comprehensive picture of the rheological conditions for which any number of wave modes coexist, we can numerically search for a marginal curve of stability in parameter space.

3.5.1 Marginal curve of spatial stability

Let us consider the conditions for which the gravity, capillary and dilational wave modes exist.

There are five possible roots of the dispersion relation

$$\Delta(k, \omega, \mu, \rho, g, \sigma, \epsilon) = 0 \tag{3.15}$$

corresponding to gravity, capillary and dilational wave modes.

To be physically realistic, these roots must satisfy

$$Real(m) > 0 \quad Real(k) > 0 \quad Real(\omega) > 0 \tag{3.16}$$

and to be stable in space and time, respectively, they must satisfy

$$Imag(k) < 0 \quad Imag(\omega) > 0. \tag{3.17}$$

The range of rheological conditions under which a stable physical wave mode exists is marked by a boundary in parameter space for each mode. The bound of the spatial stability, or marginal curve of spatial stability, in rheological parameter space must satisfy

$$Imag(\omega) = 0 \quad Imag(k) = 0 \tag{3.18}$$

for some neighboring values of the parameters. Inside this bound, all rheologies result in roots of the dispersion relation satisfying

$$Imag(k) < 0. \tag{3.19}$$

There can be multiple bounds defined: one for which there is one stable root, another in which there are two stable roots, and so forth. Thus different regions of parameters space will have n numbers of physical and stable roots associated with

them.

3.5.2 Non-dimensional parametric bounds of spatial stability

Rather than delinating the bounds of stability in rheological parameter space, we non-dimensionalize the dispersion relation and define the bounds in the resulting non-dimensional rheological and physical parameter space. Which non-dimensional (ND) parameters control the bounds will be determined by examining the dependence of the number of stable roots of the dispersion relation on the parameters.

Before proceeding, it is necessary to decide how to non-dimensionalize the dispersion relation. This relation has are eleven dimensional variables,

$$k_R, k_I, \omega_R, \omega_I, \mu, \rho, g, \epsilon_o, \epsilon', \sigma_o, \sigma'.$$

To find the spatially stable roots of the equation, we solve for $k(\omega)$. On the marginal curve of stability, $\omega_I = 0$. To non-dimensionalize the dispersion relation, three scaling variables must be chosen from the remaining eight:

$$\omega_R, \mu, \rho, g, \epsilon_o, \epsilon', \sigma_o, \sigma'.$$

There are eighty-one possible sets of three variables which can be made.

To gain some insight into which of these might be important to stability, we can take advantage of the dimensional similarity of σ_o and ϵ_o and of σ' and ϵ' and numerical investigate the dependence of the number of stable roots on

$$\frac{\sigma'}{\epsilon'} \quad \frac{\sigma_o}{\epsilon_o} \quad \frac{\sigma'\omega}{\sigma_o}$$

$$\frac{\epsilon'\omega}{\epsilon_o} \quad \frac{\sigma'\omega}{\epsilon_o} \quad \frac{\epsilon'\omega}{\sigma_o}.$$

Note that $\omega = \omega_R$ as $\omega_I = 0$.

To obtain $\frac{\sigma_o}{\epsilon_o}$, $\frac{\epsilon'\omega}{\epsilon_o}$ and $\frac{\sigma'\omega}{\epsilon_o}$, the dispersion relation must be non-dimensionalized by ϵ_o, g, ω:

$$[P_1(k^* - m^*)]^2 + E^* \cdot S^* = 0 \tag{3.20}$$

$$E^* = k^{*2}(1 + iP_2) + iP_1(k^* + m^*)$$

$$S^* = k^{*2}(P_3 + iP_4) + iP_1(k^* + m^*) + P_5\left(1 - \frac{1}{k^*}\right)$$

$$m^{*2} = k^{*2} + i\frac{P_5}{P_1}$$

where

$$P_1 = \frac{\mu g}{\epsilon_o \omega} \quad P_2 = \frac{\omega \epsilon'}{\epsilon_o}$$

$$P_3 = \frac{\sigma_o}{\epsilon_o} \quad P_4 = \frac{\omega \sigma'}{\epsilon_o} \quad P_5 = \frac{\rho}{\epsilon_o \omega}\left(\frac{g}{\omega}\right)^3$$

To obtain the other parameters, other non-dimensionalizations can be made. For ease of dicussion, these parameters will be referred to in terms of P_1, P_2, P_3, P_4, and P_5, so that

$$\frac{\sigma'}{\epsilon'} = \frac{P_4}{P_2}, \qquad \frac{\sigma'\omega}{\sigma_o} = \frac{P_4}{P_3}, \qquad \frac{\epsilon'\omega}{\sigma_o} = \frac{P_2}{P_3} \tag{3.21}$$

A numerical investigation was made of the above parameters and also variations of μ and ρ with respect to ϵ_o, ϵ', σ_o and σ':

$$\frac{\mu g}{\epsilon_o \omega} = P_1 \qquad \frac{\rho}{\epsilon_o \omega}\left(\frac{g}{\omega}\right)^3 = P_5 \qquad \frac{\mu g}{\epsilon' \omega^2} = \frac{P_1}{P_2} \qquad \frac{\rho}{\epsilon' \omega^2}\left(\frac{g}{\omega}\right)^3 = \frac{P_5}{P_2}$$

$$\frac{\mu g}{\sigma_o \omega} = \frac{P_1}{P_3} \qquad \frac{\rho}{\sigma_o \omega}\left(\frac{g}{\omega}\right)^3 = \frac{P_5}{P_3} \qquad \frac{\mu g}{\sigma' \omega^2} = \frac{P_1}{P_4} \qquad \frac{\rho}{\sigma' \omega^2}\left(\frac{g}{\omega}\right)^3 = \frac{P_5}{P_4}.$$

and variation of ρ with respect to μ,

$$\frac{\rho}{\omega \mu}\left(\frac{g}{\omega}\right)^2 = \frac{P_5}{P_1}.$$

This last parameter occurs in the expression for m^* and affects the relative vertical

decay rates of the two wave modes. When its value is much greater than k^*, and ϵ approaches zero, the flow is mainly potential ($|A| >> |B|$) (Lucassen-Reynders and Lucassen, 1969).

It is possible to have many other non-dimensional parameters, however, the parameters considered above take into account variation of each of the dimensional parameters with respect to the others and give us a full picture of the parametric dependency of stability.

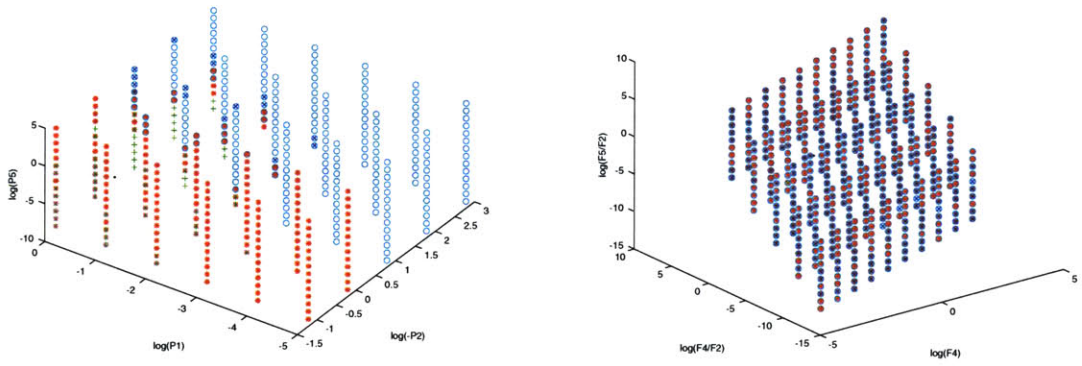

Figure 3-3: Figure 3-3a shows clear dependence on the three axes parameters, $\log(P5), \log(P1), \log(-P2)$. Figure 3-3b shows a lack of dependence on the three axes parameters, $\log(P5/P2), \log(P4/P2), \log(P4)$. The blue $\times$'s, cyan $\circ$'s, red $*$'s and green $+$'s correspond to 0, 1, 2 and 3 physical and stable roots, respectively.

The numerical investigation was made by calculating the number of stable roots of a non-dimensional form of the dispersion relation dependent on the above parameters. One of the numerical codes for these calculations is described in Appendix A. Colored symbols corresponding to the number of stable roots were then plotted in ND parameter space. Dependence of root stability on these parameters was clearly shown by regions of ND parameter space for which only the symbols for 0, 1 or 2 roots appeared. Non-dependence was shown by a mix of symbols for all parameter values as in figure 3-3.

The parameters were varied over many orders of magnitude in order increments. Together, $\epsilon'\omega/\epsilon_o$, $\mu g/\epsilon_o\omega$ and $\rho/\epsilon_o\omega(g/\omega)^3$ were correlated to the number of stable roots shown in figure 3-5, as well as $\rho/\epsilon'\omega^2(g/\omega)^3$, $\rho/\sigma'\omega^2(g/\omega)^3$ and $\rho/\omega\mu\,(g/\omega)^2$ together as shown in figure 3-4.

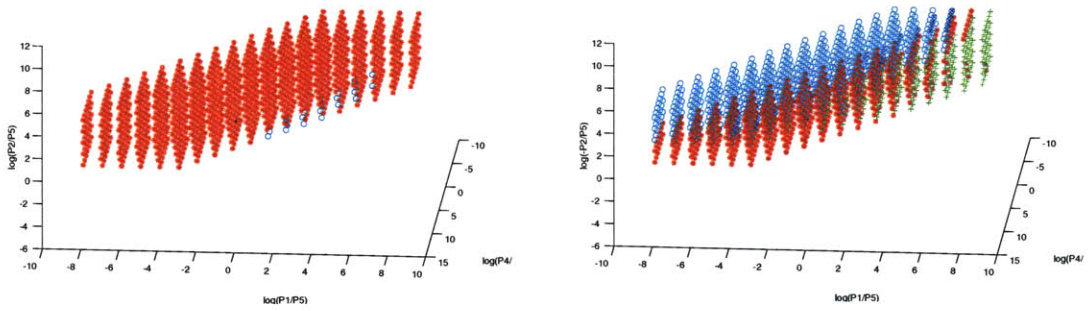

Figure 3-4: Root dependence on $\frac{P_2}{P_5} = \frac{\epsilon'\omega^2}{\rho}\left(\frac{\omega}{g}\right)^3$, $\frac{P_4}{P_5} = \frac{\sigma'\omega^2}{\rho}\left(\frac{\omega}{g}\right)^3$ and $\frac{P_1}{P_5} = \frac{\omega\mu}{\rho}\left(\frac{\omega}{g}\right)^2$.The blue $\times$'s, cyan $\circ$'s, red $*$'s and green $+$'s correspond to 0, 1, 2 and 3 physical and stable roots, respectively. In figure 3-4a, ϵ' is positive and in figure 3-4b, ϵ' is negative.

In figure 3-4, we see three regions of stability: one stable root, two stable roots and three stable roots. These regions are defined in $\left(\frac{\rho}{\omega\mu}\left(\frac{g}{\omega}\right)^2, \frac{\rho}{\sigma'\omega^2}\left(\frac{g}{\omega}\right)^3, \frac{\rho}{\epsilon'\omega^2}\left(\frac{g}{\omega}\right)^3\right)$ parameter space. While this group of parameters shows a correlation to the number of stable roots, we will find $\epsilon'\omega/\epsilon_o$, $\mu g/\epsilon_o\omega$ and $\rho/\epsilon_o\omega(g/\omega)^3$, (P_2, P_1, P_5), most useful in classifying the conditions under which the various modes exist. These parameters show that the the existence of more than one mode depends on the ratios of relaxation and dilational viscous retarding effects to elastic propagation of energy

$$DVE = \frac{\omega\epsilon'}{\epsilon_o}$$

bulk viscous retarding effects to elastic propagation of energy

$$BVE = \frac{\mu g}{\epsilon_o\omega}$$

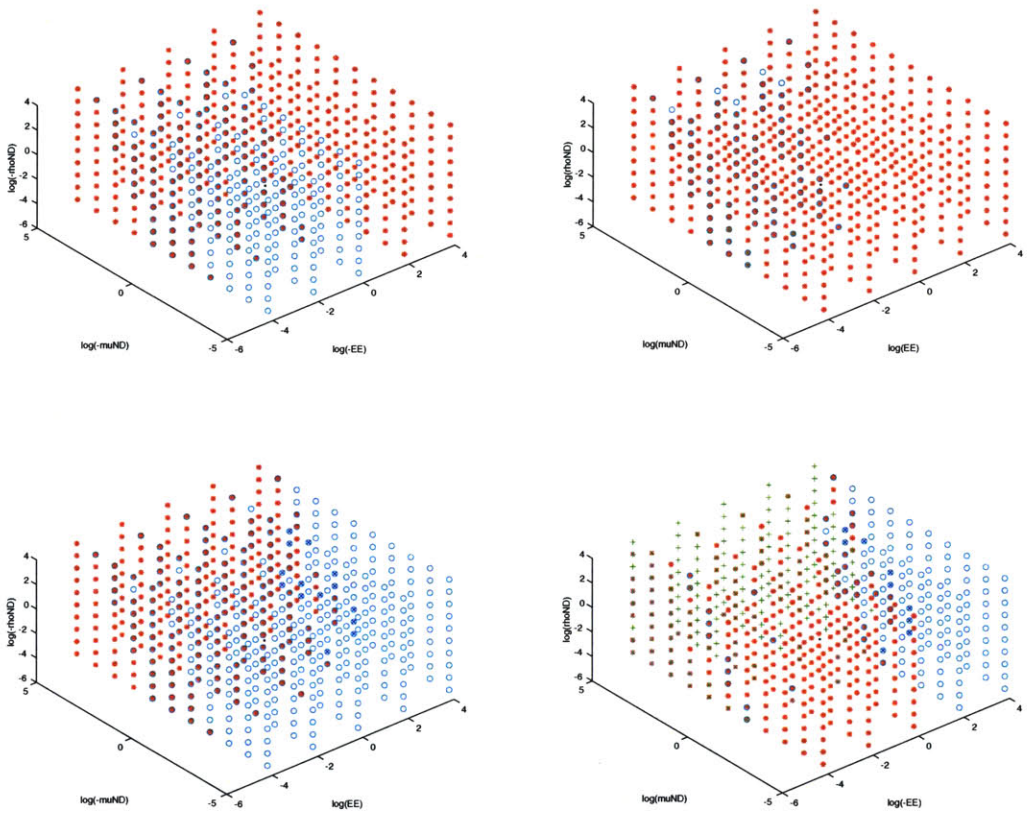

Figure 3-5: The regions of stability defined in $\left(P_2 = DVE = \frac{\epsilon'\omega}{\epsilon_o}, P_1 = BVE = \frac{\mu g}{\epsilon_o \omega}, P_5 = BIE = \frac{\rho}{\epsilon_o \omega}\left(\frac{g}{\omega}\right)^3\right)$ parameter space. The four figures correspond to the four quadrants of $\epsilon = \epsilon_o + i\omega\epsilon'$. The blue $\times$'s, cyan $\circ$'s, red $*$'s and green $+$'s correspond to 0, 1, 2 and 3 physical and stable roots, respectively.

and bulk inertial retarding effects to elastic propagation of energy

$$BIE = \frac{\rho}{\epsilon_o \omega}\left(\frac{g}{\omega}\right)^3$$

that controls stability of the wave modes. Stable gravity and capillary waves never coexist and the two dilational modes, which do not appear as as physical and and stable until the gravity mode does, are generally symmetric around the imaginary k axis with one physical, $Real(k) > 0$ and one unphysical $Real(k) < 0$, thus when two modes coexist, they are the capillary and dilational modes. The parameters above are

all ratios retarding effects to elastic propagation of energy, they govern the dilational modes. Thus, the conditions for the existence of the dilational mode are marked by the boundaries of the region of two physical stable roots.

A third stable root of the dispersion relation is here predicted, but its physical correlation is unlikely. For the reasons discussed above, it would have to be a second dilational mode. It occurs in the forth quadrant of ϵ for which, as discussed below, $\epsilon' < 0$ and $\epsilon_o > 0$. It appears when P_1 is small and thus bulk viscous effects are small in comparison to the elasticity of the film. It also occurs at larger P_1 values when P_2 is small and smaller P_1 values when P_2 is large. Thus, when the response of the film to elastic forcing is large in comparison to the elastic forcing, the existence of the third root requires the bulk viscous effects to be very small in comparison to film elasticity, but when the response of the film is very small when compared to elasticity, the third root can arise when bulk viscous effects are nearly balanced by film elasticity. Thus, the third root could to be an artifact of fluids and films for which some longitudinal viscosity is very low, however, the most likely explanation for a third stable root is that it is an artifact of the numerical code. For extremely large or small values of any parameter, as is the case here, errors inherent in the root solving algorithm an cause anomalous results. As the conditions for which it occurs are quite extreme, it is unlikely in any case that this third mode would ever be seen.

3.5.3 The four quadrants of ϵ

The four figures correspond to the four quadrants of ϵ:

$$\epsilon = |\epsilon| e^{i\theta} = \epsilon_o + i\epsilon'' = \epsilon_o + i\omega\epsilon'.$$

The reader will recall from chapter 1 that ϵ itself is composed of ε, κ and η_N:

$$\epsilon = \epsilon_o + i\omega\epsilon' = \varepsilon_o + i\omega(\varepsilon' + \kappa + \eta_N) \tag{3.22}$$

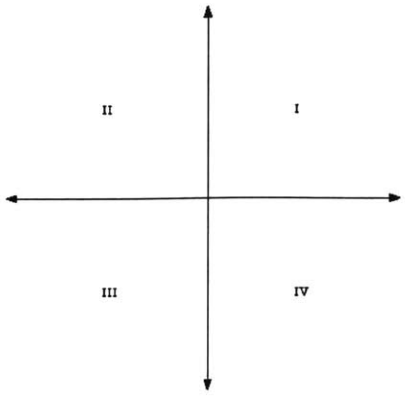

Figure 3-6: The four quadrants of ϵ.

where κ and η_N are dilational viscosities and

$$\varepsilon = |\varepsilon| e^{i\theta} = \varepsilon_o + i\varepsilon'' = \varepsilon_o + i\omega\varepsilon' = \frac{\partial \sigma}{\partial x} \tag{3.23}$$

is the dilational modulus. The angle θ represents the phase difference between variation in surface tension and the elastic response of the film. The four quadrants in complex ε space are shown in figure 3-7. Within these quadrants are defined regions

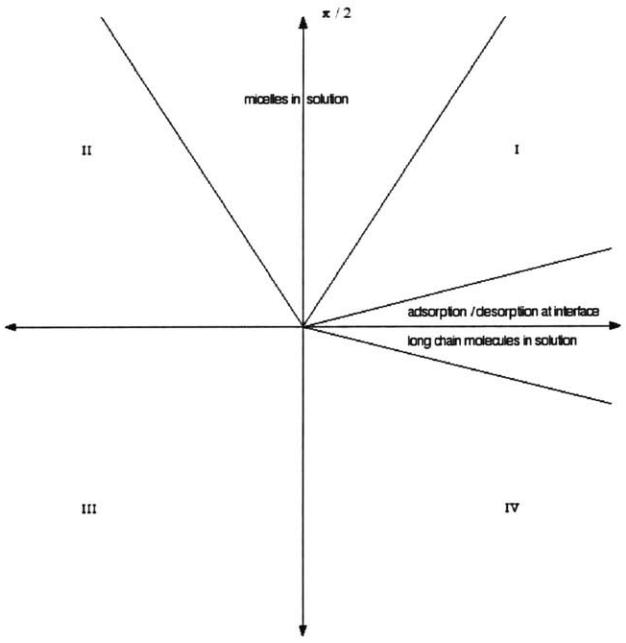

Figure 3-7: The four quadrants of ε.

corresponding to certain phenomena in the physics of various films.

As ε_o and ε'' or $\omega\varepsilon'$ vary in the four quadrants, then so must ϵ:

$$\epsilon = \epsilon_o + i\omega\epsilon' = \varepsilon_o + i\omega(\varepsilon' + \kappa + \eta_N).$$

Thus the response, or relaxation, times of the surfactant films and the existence of the dilational wave mode are linked.

It is not obvious how to separate the effects of $\kappa + \eta_N$ from ε' without a clearer picture of the range of $\kappa + \eta_N$ for the types of surfactants that lie in each quadrant in ε. We can though infer some effects of the nature from considering the four quadrants of ϵ.

The first quadrant of ϵ can correspond to either the first or the fourth quadrant of ε.

1st quadrant: $\epsilon_o > 0 \quad \epsilon' > 0$

$$\begin{aligned} &\varepsilon_o > 0 \\ &\epsilon' = \varepsilon' + \kappa + \eta \\ &\text{2 possibilities} \begin{cases} \varepsilon' > 0 \\ \varepsilon' < 0 \text{ but } \kappa + \eta > -\varepsilon' \end{cases} \end{aligned} \tag{3.24}$$

The second quadrant of ϵ can correspond to either the second or the third quadrant of ε.

2nd quadrant: $\epsilon_o < 0 \quad \epsilon' > 0$

$$\begin{aligned} &\varepsilon_o < 0 \\ &\text{2 possibilities} \begin{cases} \varepsilon' > 0 \\ \varepsilon' < 0 \text{ but } \kappa + \eta > -\varepsilon' \end{cases} \end{aligned} \tag{3.25}$$

The third quadrant of ϵ corresponds to the third quadrant of ε.

3rd quadrant: $\epsilon_o < 0 \quad \epsilon' < 0$

$$\begin{array}{l} \varepsilon_o < 0 \\ \text{1 possibility} \left\{ \begin{array}{l} \\ \varepsilon' < 0 \end{array} \right. \end{array} \tag{3.26}$$

The forth quadrant of ϵ corresponds to the forth quadrant of ε.

4th quadrant: $\epsilon_o > 0 \quad \epsilon' < 0$

$$\begin{array}{l} \varepsilon_o > 0 \\ \text{1 possibility} \left\{ \begin{array}{l} \\ \varepsilon' < 0 \end{array} \right. \end{array} \tag{3.27}$$

3.5.4 Special cases

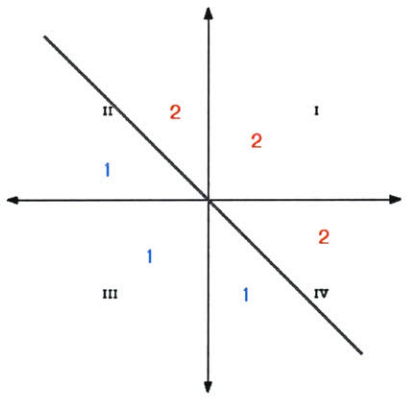

Figure 3-8: The number of stable roots in figure 3-9 mapped into the four quadrants of ϵ.

Under certain conditions, which interestingly are quite common, the existence of stable roots of the dispersion relation is entirely dependent on $\omega\epsilon'/\epsilon_o$. This occurs when P_1, the ratio of bulk viscous effects to film elasticity, is very small ($\leq 10^{-3}$), or when P_1 is somewhat small ($\leq 10^{-1}$) and P_5, the ratio of bulk inertial effects to film elasticity, is not too small ($\geq 10^{-2}$). Then, the regions of numbers of stable roots can be presented as in figure 3-9.

The regions of one and two stable roots can be simply viewed in complex ϵ space (figure 3-8). In this figure, the line $\tan\epsilon = -1$ demarcates the boundary between the ϵ values for which the dispersion relation has two stable roots and those values

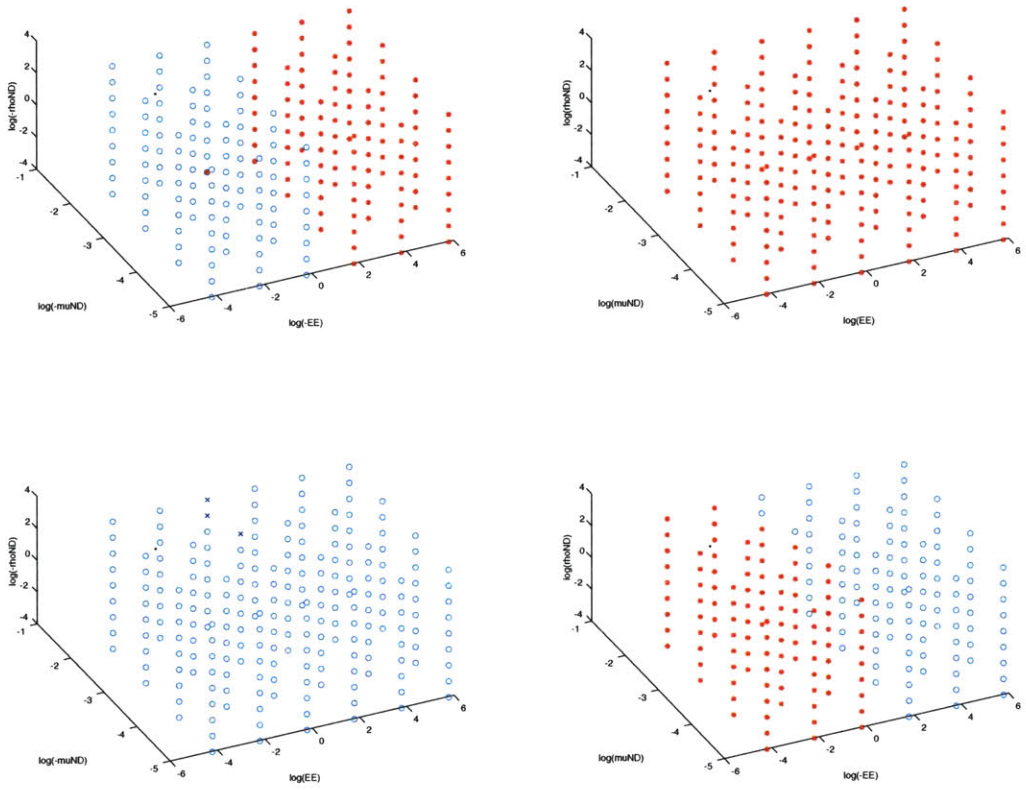

Figure 3-9: The regions of stability defined in $\left(P_2 = DVE = \frac{\epsilon'\omega}{\epsilon_o}, P_1 = BVE = \frac{\mu q}{\epsilon_o \omega}, P_5 = BIE = \frac{\rho}{\epsilon_o \omega}\left(\frac{g}{\omega}\right)^3\right)$ parameter space. The four figures correspond to the four quadrants of $\epsilon = \epsilon_o + i\omega\epsilon'$. The blue $\times$'s, cyan $\circ$'s and red $*$'s and green $+$'s correspond to 0, 1 and 2 physical and stable roots, respectively. In these parameter ranges, only $P_2 = \frac{\epsilon'\omega}{\epsilon_o}$ controls the number of stable roots.

of ϵ for which it has one stable root. As ϵ is a function of ε, the dependency of the number of stable roots on the phase of ϵ indicates that the number of stable roots is dependent on the film relaxation.

Chapter 4

Analytical and numerical descriptions of wave mode resonance

4.1 Literature review

Evidence of resonant interaction between the capillary and the dilational wave modes has been noted in numerical, experimental and field studies. This evidence includes a peak in the damping rate of the capillary wave mode together with a concurrent trough in the damping rate of the dilational wave mode and mixed-moode behaviour, which suggests that neither wave mode has a predominantly capillary or dilational character near resonance conditions.

Before the root of the dispersion relation corresponding to the dilational wave mode was discovered by Lucassen (1968), peaks in the capillary wave mode damping rate were found in numerical studies (cf. Dorrestein, 1951, Hansen & Mann, 1964, van den Tempel & van de Riet, 1965). These were later noted experimentally by Bock (1987) as well as in a field study by Wei & Wu (1992). After the discovery of the second root, it was found numerically that a trough in the dilational wave mode damping rate occurs concurrently with the peak in the capillary wave mode damping

rate (Hühnerfuss *et al.* 1985, Dysthe & Rabin, 1986, Cini *et al.* 1987, Ghia & Trivero, 1988, etc.). As this peak and trough both occurred when the frequencies of the two wave modes coalesced, this behaviour was attributed to resonance between the two modes.

A second piece of evidence occuring near frequency coalescence of the two wave modes, termed 'mixed mode behaviour', has been found in a numerical studies (Earnshaw & McLaughlin 1991, Rednikov et al. 1998). Earnshaw & McLaughlin found that, while for certain combinations of values of the surfactant film rheological parameters (on which the roots of the dispersion relation depend) the two wave modes appear to be either wholly capillary or dilational in behaviour, altering these parameter values led to the two modes adopting the opposite wave mode behaviour. The critical values of the parameters for which the change occurs coincide with the values of the parameters for which the two wave mode frequency roots of the dispersion relation are closest to resonance. In this immediate region, neither wave mode can be classified as wholly capillary or wholly dilational in nature. Such behaviour was described by the authors as 'mixed mode'.

4.2 An analytical description of modal resonance

4.2.1 Evidence of resonance in previous numerical and experimental studies

Two behaviors attributed to resonance between the capillary and dilational wave modes have been noted in numerous numerical and experimental studies. These behaviors are peaks in the damping rate of the capillary mode and mixed mode behaviour between the capillary and dilational modes.

Figure 4-1 shows both behaviors. These curves were produced from Lucassen's dispersion relation with $\mu = 11.3 \times 10^{-4}$ kg m/s, $k = 5 \times 10^4$ 1/m^2, $\sigma_o = 65.0 \times 10^{-3}$ kg/s^2, $\sigma' = 2.5 \times 10^{-7}$ kg/s^2, $\rho = 998$ kg m/s, and $g = 9.81$ m/s. The upper set of curves were made for $Im(\epsilon) = \omega\epsilon' = 0.0015$ kg s^{-2} and the lower for $Im(\epsilon) = 0.0006$

kg s^{-2}.

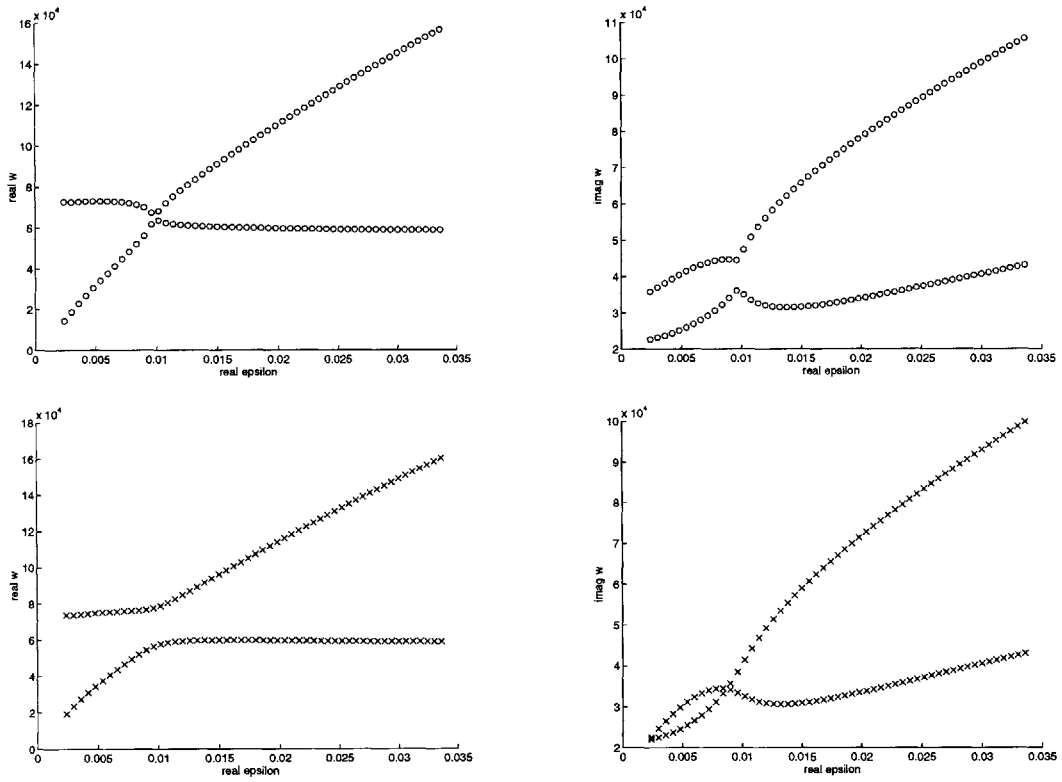

Figure 4-1: This figure shows plots of frequency, ω_R, and spatial damping rate, ω_I, versus elasticity, ϵ_o for both capillary and dilational wave modes. The upper set of plots was made for $Imag(\epsilon) = 0.0015$ kg s^{-2} and the lower for $Imag(\epsilon) = 0.0006$ kg s^{-2}. Labeling the four plots clockwise beginning in the upper left hand corner, we see in plot (b) a peak in the capillary wave mode damping rate concurrently with a trough in the dilational wave mode damping rate. Plot (c) shows mixed-mode behavior. Neither wave mode appears to behave stictly as a capillary nor a dilational wave.

In figure 4-1(b), we see $Im(\omega)$ plotted against $Re(\epsilon) = \epsilon_o$. Near $Re(\epsilon) = 0.0102$ kg/s^2 the two modes approach each other. This is the resonant peak (trough) mentioned in the literature. Away from this value of $Re(\epsilon)$, the lower wave mode appears to be nearly independent of $Re(\epsilon)$. This is the capillary mode. The other mode, which is highly dependent on $Re(\epsilon)$, is the dilational mode. A similar two-dimensional numerical result for $Im(\epsilon) = 0.0$ kg/s^2 was obtained by Earnshaw & McLaughlin (1991).

In figure 4-1(c), we see $Re(\omega)$ plotted versus $Re(\epsilon)$. The behaviour of the wave modes is wholly different than in figure 4-1(a). In figure 4-1(c), the two modes appear to switch character near $Re(\epsilon) = 0.0102$ kg/s^2. In the neighborhood of this value of ϵ,

the wave modes cannot be identified as either wholly capillary or dilational in nature. This is the phenomena labeled as mode mixing by Earnshaw & McLaughlin (1991). It is more generally referred to as an avoided crossing.

Figure 4-2 shows the resonance effect of a peak in the capillary mode spatial damping coefficient appearing in experimental data. This data is a reproduction of a data set (Bock 1989) showing variation of spatial damping, $(Im(k))$, with frequency, $(f = \omega/2\pi)$, for capillary waves propagating across the surface of Hercolube C at 45°C. The data set is marked in o's with the peak in the damping rate occuring near 6 Hertz. The solid line corresponds to Bock's fit of the dispersion relation to his data assuming that both f and σ are real and $\epsilon = 0.0$.

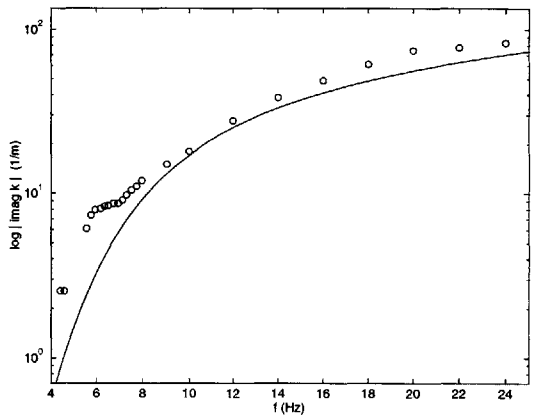

Figure 4-2: Reproduction of a data set (Bock 1989) showing variation of spatial damping, $(Im(k))$, with frequency, $(f = \omega/2\pi)$, for capillary waves propagating across the surface of Hercolube C at 45°C. The data set is marked in o's. The solid line corresponds to Bock's fit of the dispersion relation to his data assuming that both f and σ are real and $\epsilon = 0.0$.

4.2.2 Description of mode to mode resonance

Although phenomena related to resonance between the capillary and dilational wave modes have been noted in the literature, there was no mathematical description of this type of resonance. In Brown *et al.* 2002, we presented a mathematical description of first order wave mode resonance and demonstrated how all of the above mentioned

phenomena could be accounted for with this description. A discussion of the work in this paper follows.

General dispersion relation

A dispersion relation can be characterized by the expression

$$\Delta(\omega, \pi_i) = 0, \tag{4.1}$$

which provides the natural frequencies of the system, ω, for some values of the physical parameters of the system, $\pi_i, i = 1, 2, \ldots p$. The set of all possible combinations of parameters and frequencies that satisfy this equation is its solution space. If the parameters and frequencies are complex, then the dispersion relation solution space will also be complex.

Resonance occurs when there are two or more repeated roots of the dispersion relation. In the complex solution space, this phenomenon is represented by root coalescence points (ω_o, π_o) of (4.1) which satisfy the conditions (Triantafyllou & Triantafyllou, 1991):

$$\Delta(\omega_o, \pi_o) = 0 \qquad \frac{\partial^n \Delta}{\partial \omega^n}(\omega_o, \pi_o) = 0, \quad n = 1, \ldots, m-1, \tag{4.2}$$

where m is the order of complex root (in this case, frequency) coalescence. The solution of (4.2) represents a multiply (m) repeated complex root, ω_o, for a corresponding value of the complex parameter, $\pi_i = \pi_{o_i}$. An expansion around this point yields, for a single parameter π:

$$\Delta(\omega, \pi) = 0 = \alpha(\omega - \omega_o)^m + \beta(\pi - \pi_o) + H.O.T., \tag{4.3}$$

where $H.O.T$ refers to higher order terms and α and β are nonzero constants.

Figure 4-3 shows how the solution space, $\omega(\pi)$, will look around a second order ($m = 2$) root coalescence point. Lines of constant real and lines of constant imaginary π from the complex π plane are mapped into the complex ω plane and lines of constant

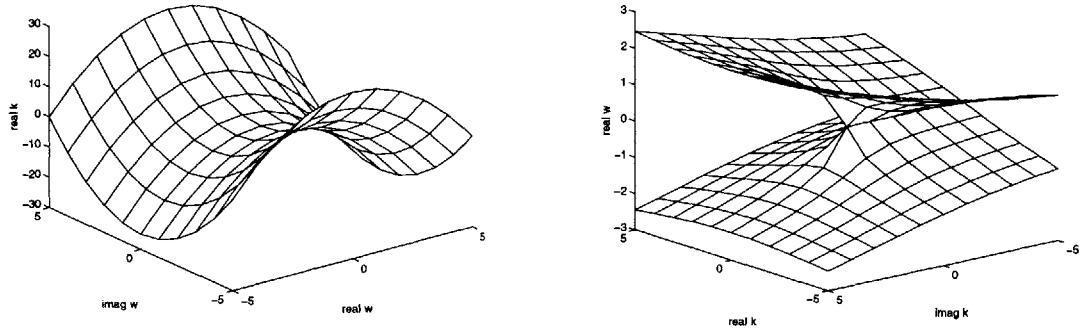

Figure 4-3: In figure 4-3a, lines of constant real and imaginary π in the complex π plane are mapped via relation (4.3) with $\alpha = \beta = 1$ and $\omega_o = \pi_o = 0$ into the complex ω plane and displayed in $(Re(\omega), Im(\omega), Re(\pi))$ three space. In figure 4-3b, lines of constant real and imaginary ω in the complex ω plane are mapped via relation (4.3) with $\alpha = \beta = 1$ and $\omega_o = \pi_o = 0$ into the complex π plane and displayed in $(Re(\pi), Im(\pi), Re(\omega))$ three space.

real and imaginary ω from the complex ω plane are mapped into the complex π plane. The frequency coalescence point appears as a saddle point in the complex ω plane and as a branch point in the complex π plane.

The distortion of the solution space near the frequency coalescence point is due to the sensitivity of the shape of the solution space to the parameter π. This can be demonstrated mathmatically by looking at the mapping for $\omega(\pi)$:

$$\omega - \omega_o = \gamma\sqrt{\pi - \pi_o}, \tag{4.4}$$

where $\gamma = \sqrt{\beta/\alpha}$. From (4.4) we see that a small variation in π of order δ will produce a variation in ω of the order $\sqrt{\delta}$. The sensitivity of ω to variations in π is calculated as

$$S(\omega, \pi) = \frac{\partial \omega}{\partial \pi} = \frac{1}{2}\,\gamma\,\frac{1}{(\pi - \pi_o)^{1/2}}. \tag{4.5}$$

Thus, as we approach the wavenumber coalescence point, ω becomes infinitely sensitive to variation in π and the space is drastically stretched.

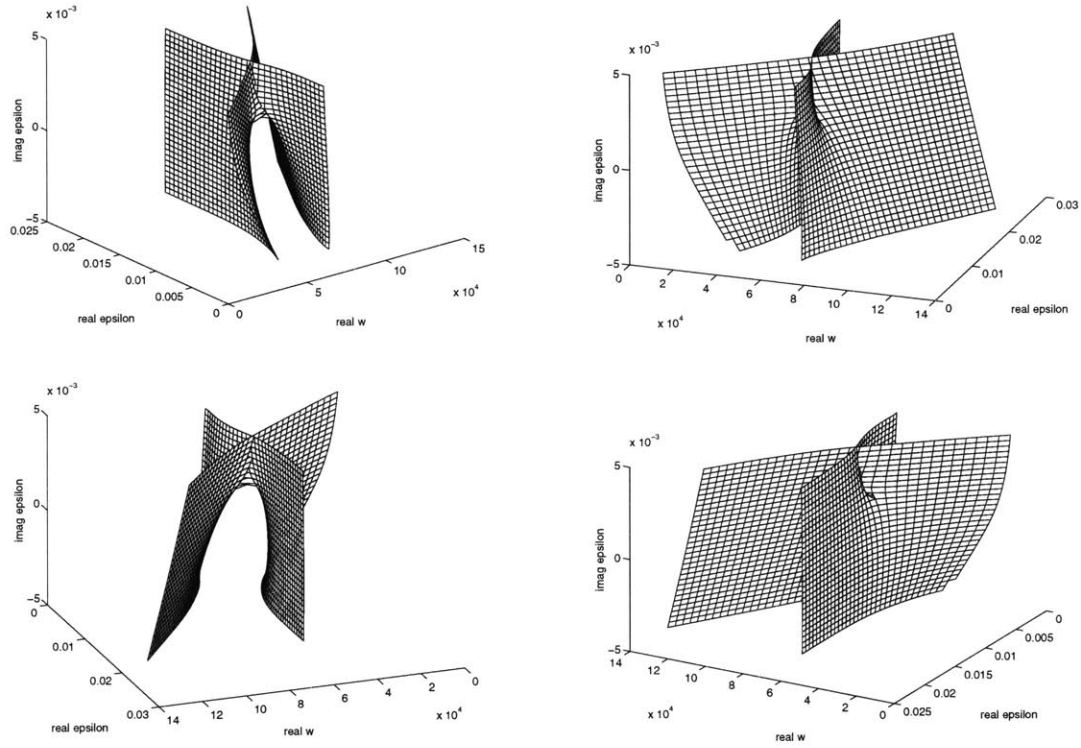

Figure 4-4: Projection of the solution space for $\Delta(\omega, k, \epsilon, \sigma) = 0$ onto ($Re(\omega)$, $Re(\epsilon)$, $Im(\epsilon)$) three space. The viewer's perspective moves counterclockwise around the projection in figures (a) — (d). The labels CWM and DWM indicate the portion of the solution space corresponding to the capillary and dilational wave modes, respectively.

Capillary-dilational dispersion relation

The dispersion relation for capillary and dilational waves at an air-fluid interface can be characterized by

$$\Delta(k, \omega, \epsilon, \sigma, \rho, \mu, g) = 0, \tag{4.6}$$

or, for a bulk fluid with known properties, ρ and μ, simply as:

$$\Delta(k, \omega, \epsilon, \sigma) = 0 \tag{4.7}$$

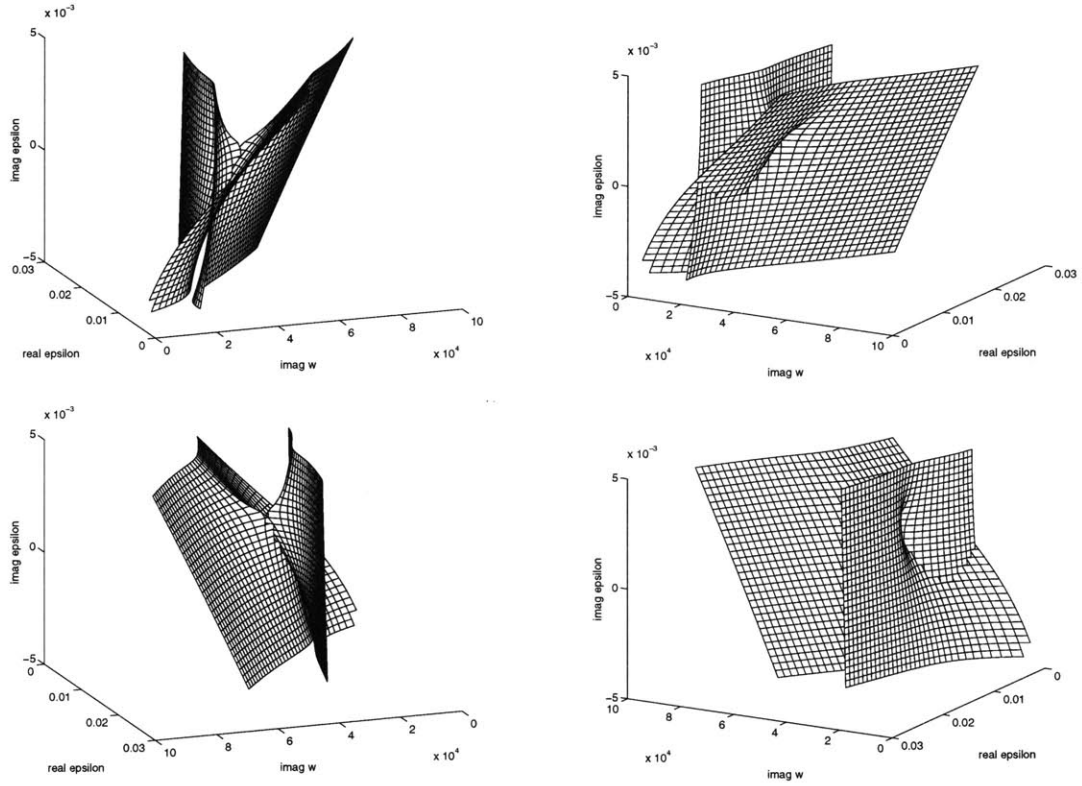

Figure 4-5: Projection of the solution space for $\Delta(\omega, k, \epsilon, \sigma) = 0$ onto ($Im(\omega)$, $Re(\epsilon)$, $Im(\epsilon)$) three space. The viewer's perspective moves counterclockwise around the projection in figures (a) — (d). The labels CWM and DWM indicate the portion of the solution space corresponding to the capillary and dilational wave modes, respectively.

where

$$k = k_R + ik_I \qquad \omega = \omega_R + i\omega_I$$
$$\epsilon = \epsilon_0 + i\omega\epsilon' \qquad \sigma = \sigma_0 + i\omega\sigma'. \tag{4.8}$$

The letters R and I denote the real and imaginary parts, respectively, of the quantities they subcript.

The solution space for $\Delta(k, \omega, \epsilon, \sigma)$ is eight dimensional – all four parameters are complex. If we fix two variables, for example, k and σ, we can reduce the solution space for $\epsilon(\omega)$ to four variable dimensions. It is in the neighborhood of a root coalescence point for ϵ that the plots of the solution space in figure 4-4 are produced.

The roots were obtained using Matlab's standard root solver. This root solver is predicated on the solution of an equivalent eigenvalue problem written in terms of a companion matrix for the original polynomial. The solution is accurate to within 0.1 percent.

Figure 4-4 shows a projection of the four-dimensional solution space onto ($Re(\omega)$, $Re(\epsilon)$, $Im(\epsilon)$) three space. Figure 4-5 shows a projection of the solution space onto ($Im(\omega)$, $Re(\epsilon)$, $Im(\epsilon)$) three space. The physical parameters in the dispersion relation have been assigned the the same values as those in figure 4-1 which was a reproduction of a figure in a numerical study by Earnshaw & McLaughlin (1991): $\mu = 11.3 \times 10^{-4}$ kg m/s, $k = 5 \times 10^4$ 1/m^2, $\sigma_o = 65.0 \times 10^{-3}$ kg/s^2, $\sigma' = 2.5 \times 10^{-7}$ kg/s^2, $\rho = 998$ kg m/s, and $g = 9.81$ m/s.

Our point of view travels counterclockwise around the projections to give four views of the projected solution space. Each sheet of the projection represents the portion of the solution space corresponding to a separate wave mode. The sheet which does not significantly vary with ϵ is the capillary wave mode. The other sheet, which is highly dependent on ϵ, is the dilational wave mode.

We can infer from figures 4-4 and 4-5 the shape of the four dimensional projected solution space. The root coalescence point occurs at the intersection of the loci of modal frequencies with identical imaginary parts and the loci of modal frequencies with identical real parts and can be seen in both sets of plots as the point at which the two sheets separate. It is in the neigborhood of this point that resonant interaction between the two modes occurs. It is important to note that a pair of modal roots with identical imaginary parts but not real parts, or equivalently, with identical real parts but not imaginary parts does not imply resonance.

Numerical data

In figure 4-6, the solution space is projected into two single views of each of the three dimensional parameter spaces. The lines marked by the symbols $\circ$ and $\times$ are transects of the solution space corresponding to a constant value of $Im(\epsilon) = \omega\epsilon'$. The transect above the frequency coalescence point for which $Im(\epsilon) = .0015$ kg/s^2

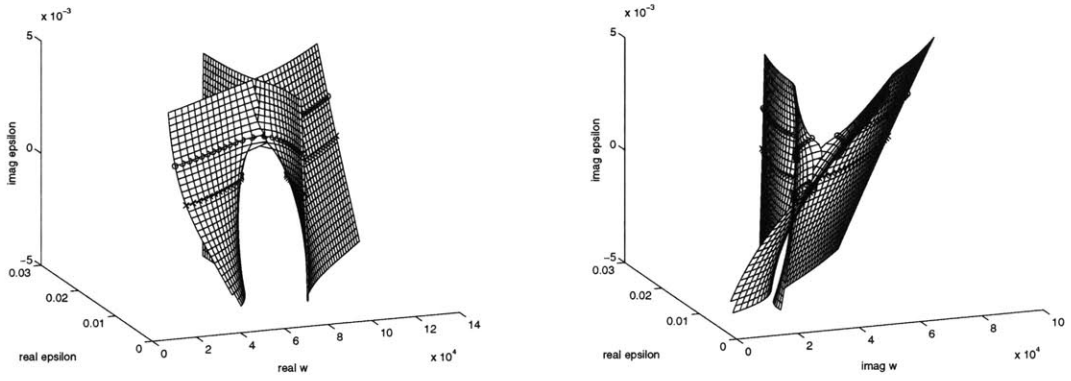

Figure 4-6: Projections of the solution space of $\Delta(\omega, k, \epsilon, \sigma) = 0$ onto ($Re(\omega)$, $Re(\epsilon)$, $Im(\epsilon)$) and (($Im(\omega)$, $Re(\epsilon)$, $Im(\epsilon)$) three spaces. The top transect, marked by $\circ$'s, corresponds to $Im(\epsilon) = .0015$ kg/s^2. The bottom transect, marked by $\times$'s, corresponds to $Im(\epsilon) = .0006$ kg/s^2.

exhibits the behaviours of peaks (troughs) for the damping rate, while the transect below the frequency coalescence point at $Im(\epsilon) = .0006$ kg/s^2 exhibits mixed mode behaviour. This becomes clear when the transects are viewed from above as in figure 4-7, a reprinting of figure 4-1.

The transect above the frequency coalescence point is plotted in figures 4-7(a) and 4-7(b). In figure 4-7(b), we see $Im(\omega)$ plotted against $Re(\epsilon) = \epsilon_o$. Near $Re(\epsilon) = 0.0102$ kg/s^2 the two modes approach each other. This is the resonant peak (trough) mentioned in the literature. Away from this value of $Re(\epsilon)$, the lower wave mode appears to be nearly independent of $Re(\epsilon)$. This is the capillary mode. The other mode, which is highly dependent on $Re(\epsilon)$, is the dilational mode. A similar two-dimensional numerical result for $Im(\epsilon) = 0.0$ kg/s^2 was obtained by Earnshaw & McLaughlin (1991).

The transect below the frequency coalescence point is plotted in figures 4-7(c) and 4-7(d). In figure 4-7(c), we see $Re(\omega)$ plotted versus $Re(\epsilon)$. The behaviour of the wave modes is wholly different than in figure 4-7(a). In figure 4-7(c), the two modes appear to switch character near $Re(\epsilon) = 0.0102$ kg/s^2. In the neighborhood of this value of ϵ, the wave modes cannot be identified as either wholly capillary or dilational in nature. This phenomena was labeled as mode mixing by Earnshaw & McLaughlin (1991). It is more generally referred to as an avoided crossing.

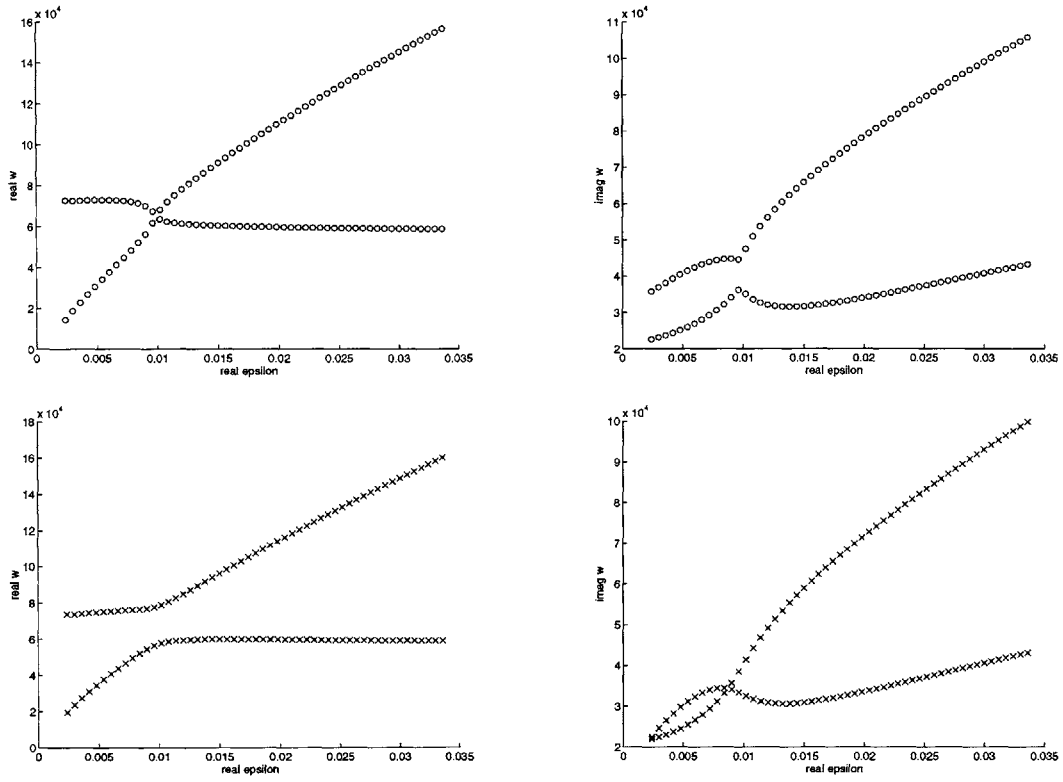

Figure 4-7: Transects above and below the frequency coalescence point in figure (4-6).

In figure 4-1(d), the imaginary parts of the two wave modes are identical twice. It is only in the occurence near $Re(\epsilon) = 0.0102$ kg/s^2 that the effects of resonance are felt (as seen by the mode mixing in the first plot), because it is near this value of ϵ in the solution space that the loci of frequencies with identical real parts and the loci of frequencies with identical imaginary parts intersect. The occurence of identical imaginary parts of the frequency near $Re(\epsilon) = 0.0024$ kg/s^2 has no meaning with regard to resonance.

As was mentioned in the introduction to section 4.2 Earnshaw & McLaughlin (1991) identified both peaks (troughs) in the damping rate and mixed mode behaviour in very similar two dimensional plots of ω versus ϵ. These authors attributed these effects to resonance, but were not able to demonstrate exactly how modal resonant interaction created the effects. Case in point, the variation of modal behaviours from peaks in the damping rate to an avoided crossing, or, as they called it, mixed

mode behavior, were not found by taking different transects of the solution space and showing how the relative position of the frequency coalescence point, but rather by varying the surface normal shear viscosity. They saw that variation in a parameter affected the modal behavior, but did not account for why the various resonance related phenomena occurred. The analytical description of resonance in Brown *et al.* (2002), by contrast, clearly demonstrates that resonance is linked to the occurence of a frequency coalescence point and with this description, we are able to show that the various resonance phenomena are linked to the position of a two dimensional transect with respect to the location of the root coalescence point in parameter space. Thus it becomes clear that the variation of the surface normal shear viscosity by Earnshaw & McLaughlin (1991) had the effect of moving the frequency coalescence point in the solution space from below the transect to above it, thus resulting in the alteration of the modal behaviour.

Experimental data

The experimental data set presented in figure 4-2 is represented in figure 6-5. In this figure, a peak in the capillary wave mode spatial damping coefficient value is apparent.

The data set is reproduced from a plot of this data in Bock (1989). Bock used a bulk fluid, Hercolube C, a pentaerythritol ester at 45.0 °C whose interface with air behaves elastically. This fluid had the following properties: surface tension = 27.7 $\times 10^{-3}$ kg/s^2, density = 940 kg/m^3 and kinematic viscosity = 14.1 $\times 10^{-6}$ m^2/s. In the experiment, capillary waves were produced at the air-fluid interface by a vibrating metal bar at a known frequency, $Re(\omega)$. The spatial damping coefficent k_I was measured using a laser slope gauge in a manner similar to Sohl *et al.* (1978).

The line in figure 6-5 corresponds to Lucassen's dispersion relation with the assumption that there was no temporal wave damping, $\omega_I = 0.0$, no transverse surface viscosity, $\sigma' = 0$, and no elasticity, $\epsilon = 0.0$. As we can see in the figure, this curve is unable to account for the small bump appearing in his data near 6.0 Hz which he attributes to resonance between the capillary and dilational wave modes.

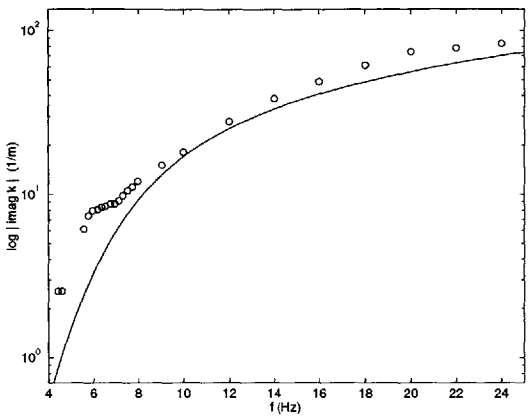

Figure 4-8: Reproduction of a data set (Bock 1989) showing variation of spatial damping, ($Im(k)$), with frequency, ($f = \omega/2\pi$), for capillary waves propagating across the surface of Hercolube C at 45°C. The data set is marked in o's. The solid line corresponds to Bock's fit of the dispersion relation to his data assuming that both f and σ are real and $\epsilon = 0.0$.

With different values of the parameters, we were able to show in Brown *et al.* (2002) that the dispersion relation is able to account for the peak in the spatial damping rate and that this effect is, indeed, due to resonance. As will be explained in fuller detail in section chapter 6, we used an inverse method to find the optimal match of the dispersion relation solution space to the data. This optimal match has a unique set of parameters $(k, \omega, \sigma, \epsilon, \mu, \rho, g)$ which describe the physical system.

The optimal match to this data was found for $\epsilon_0 = 59.1 \times 10^{-3}$ kg/s^2, $\epsilon' = -70.4 \times 10^{-5}$ kg/s, $\sigma' = 0.542 \times 10^{-5}$ kg/s and $Im(f) = 0.176$ Hz. These parameters describe both the rheology of the surface as well as the likelihood that the waves produced in the experiment were not steady, but slowly decaying in time.

The match to the data set in two dimensional $(k_I, f_R = \omega/2\pi)$ space is presented in figure 6-7 and accounts well for the small bump near 6.0 Hz. The relative position of this transect with respect to a root coalescence point marking resonance between the capillary and dilational roots is shown in figure 6-9. The peak in the capillary wave mode spatial damping rate is now well described by resonant interaction between the capillary and dilational wave modes.

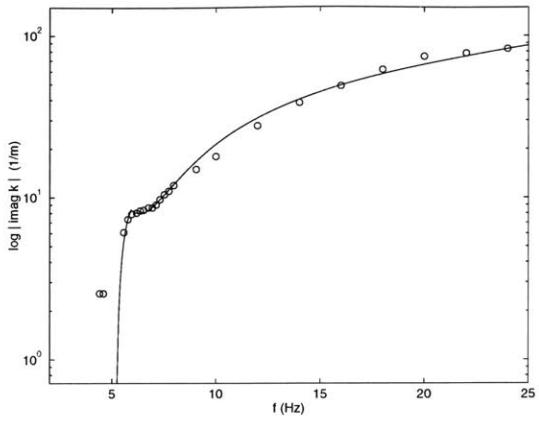

Figure 4-9: Comparison on a semilog scale of capillary wave temporal damping vs. wave frequency between the measured data, o (Bock, 1989), and the optimal match of the dispersion relation solution space to the entire data set, $-$, obtained by the optimization program.

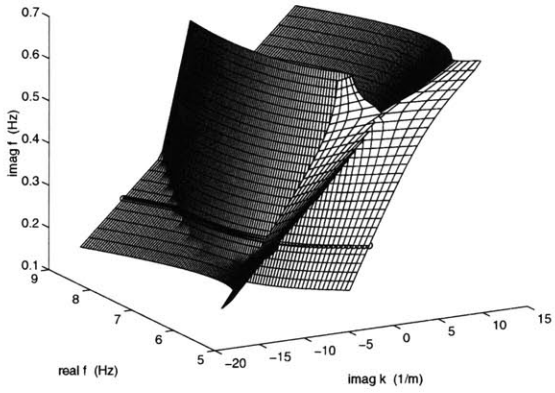

Figure 4-10: Projection of the 'best match' solution space of $\Delta(\omega, k, \epsilon, \sigma) = 0$ onto $(Re(f), Im(f), Im(k))$ three space. A frequency coalescence point is visible at the top of the figure. The transect at $Im(f) = 30.0$, marked by o's, corresponds to the best match to the measured data (Bock, 1989).

4.3 Where do we get gravity-capillary and capillary-dilational resonances?

We are in interested in two types of wavemode resonance, gravity-capillary, between the gravity and capillary modes, and capillary-dilational, between the capillary and

dilational modes. Both the existence of these modes and the conditions under which they resonate depend upon the boundary conditions at the surface. The existence of gravity and capillary modes is independent of the presence of a surface film and we will see that the conditions for these modes to resonate are completely described by an analysis of Kelvin's dispersion relation. Dilational wave modes appear in the presence of a surface film or a diffuse interface which has elastic properties similar to a film. Resonance between the capillary and dilational wavemodes is dependent on elastic properties, surface viscosities, and surface tension. The conditions for these modes to resonate are described by an analysis of Lucassen's dispersion relation.

4.3.1 Capillary–gravity resonance and Kelvin's relation

Our first taste of capillary-gravity resonance comes from a complexified version of Kelvin's dispersion relation

$$\omega^2 = kg + \frac{\sigma}{\rho}k^3 \tag{4.9}$$

with complex wavenumber, $k = k_R + ik_I$, and frequency, $\omega = \omega_R + i\omega_I$, and the complex combination of surface tension and surface normal viscosity, $\sigma = \sigma_o + i\omega\sigma'$. The letters R and I indicate the real and imaginary parts of the quantities they subscript. Surface normal viscosity, σ', is unlikely to exist without surface elasticity, ϵ. For a filmless bulk fluid with an inelastic interface, σ' will be zero. However, as we will see later, the above formulation of Kelvin's dispersion relation is adequate to describe gravity-capillary wavemode resonance even in the presence of elastic surface conditions.

The resonance conditions

$$\Delta = 0 \qquad \frac{\partial \Delta}{\partial k} = 0 \tag{4.10}$$

described in section 4.2 can be satisfied in closed form solution for this simple case. Figure 4-11 shows a projection of the dispersion relation solution space for clean

water in $k - (f = \omega/2\pi)$ space with the different Reimann sheets corresponding to the gravity and capillary wave modes. Resonance is apparent near $4(1 \pm i)$ Hertz.

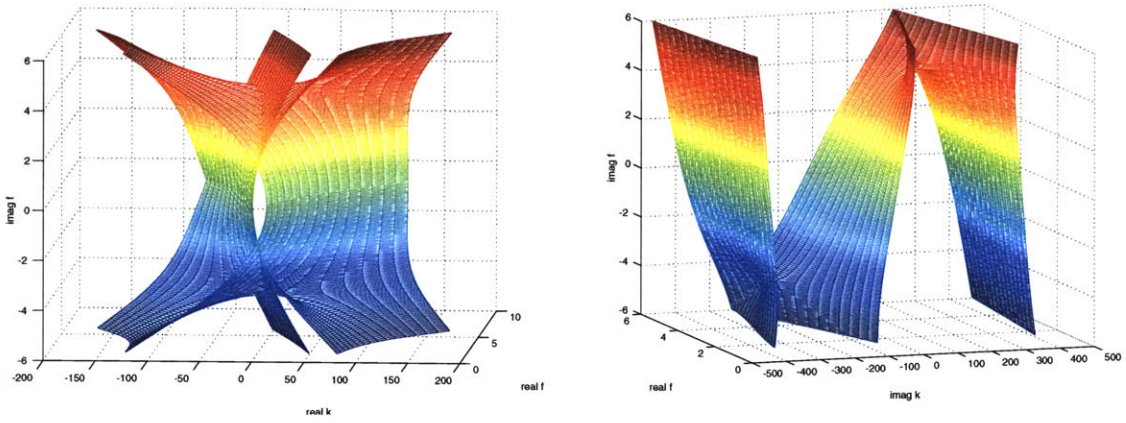

Figure 4-11: Gravity–capillary root coalescence (resonance) for water in $f - k$ space where $f = \omega/2\pi$.

To distinguish which Reimann sheet corresponds to which modal behavior, we consider the behavior of the the various sheets above and below the resonance points.

If we look at the right hand plot in figure 4-11 we can see that the center sheet is twisted so that for frequencies greater than 4 Hertz the portion above the top root coalescence point is aligned with the top of the right hand sheet and the portion below the bottom root coalescence point is aligned with the bottom of the left hand sheet. For these conditions, the right hand and left hand sheets each flow into the center sheet.

For frequencies below 4 Hertz, we can see that the center sheet of figure 4-11 also twists into two directions, above the top root coalescence point it aligns with the bottom of the right hand sheet and below the bottom root coalescence point it aligns with the top of the left hand sheet. For these conditions, the center sheet flows into the right hand and left hand sheets.

Therefore, waves which have a modal behavior defined by the left and right hand sheets below 4 Hertz have a modal behavior defined by the center sheet above 4 Hertz. Waves which have a modal behavior defined by the center sheet below 4 Hertz have

a modal behavior defined by the left and right hand sheets above 4 Hertz.

We can now identify the modal behaviors of the sheets. Figure 4-12 shows as transect of the solution space at the real f axis. We recognize the curve corresponding

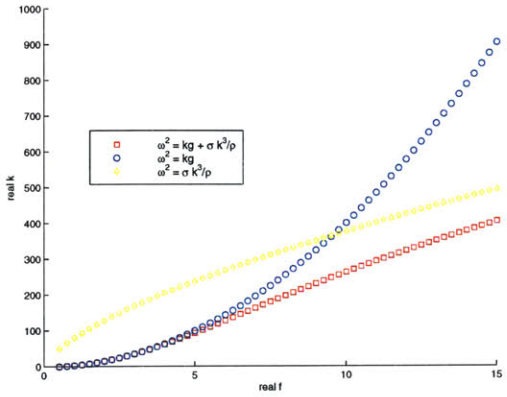

Figure 4-12: A comparison of the roots of Kelvin's dispersion relation relation to those of the dispersion relations for deep water gravity and capillary waves. The roots are plotted in $Real(k)$ - $Real(f = \omega/2\pi)$ space.

to the center sheet as representing the physical root of $f = \omega/2\pi$ versus k for Kelvin's relation. Below 4 Hertz, the curve behaves asymptotically as a deep water gravity wave governed by

$$\omega^2 = kg. \tag{4.11}$$

Above 4 Hertz, the curve behaves asymptotically as a capillary wave governed by

$$\omega^2 = \frac{\sigma k^3}{\rho}. \tag{4.12}$$

Thus below 4 Hertz the center sheet corresponds to the gravity mode and therefore the left and right hand sheets correspond to the gravity mode above 4 Hertz. Above 4 Hertz the center sheet corresponds to the capillary mode and thus below 4 Hertz the left and right hand sheets correspond to the capillary mode.

To examine resonance between the capillary and gravity modes, we proceed by

the following non–dimensionalizations

$$k^* = kL_d \qquad \omega^* = \omega T_d \tag{4.13}$$
$$L_d = \sqrt{\frac{\sigma_o}{\rho g}}; \qquad T_d = \sqrt{\frac{L_d}{g}}$$

Then,

$$\Delta^* = 0 = k^* + (1 + i\omega^*\tau)k^{*3} - \omega^{*2} \qquad \frac{\partial \Delta^*}{\partial k^*} = 0 = 1 + 3(1 + i\omega^*\tau)k^{*2} \tag{4.14}$$

where $\tau = \frac{\sigma'}{\sigma_o T_d}$.

When the surface normal shear viscosity, σ' has negligible effect (recalling that a complexified version Kelvin's relation will suffice to describe capillary-gravity resonance even for much more complicated visco-elastic fluid interfaces), then the term with τ is dropped in equations 4.14 and the resulting simple relations for resonance points (ω^*, k^*) for Kelvin's relation

$$0 = k^* + k^{*3} - \omega^{*2} \qquad 0 = 1 + 3k^{*2} \tag{4.15}$$

are satisfied for $k^* = \pm\sqrt{-\frac{1}{3}}$ with corresponding $k = \pm 212.08i$ 1/m and $\omega/2\pi = \pm 4.1914(1 \pm i)$ 1/s for clean water. The solution space comprising all of the roots of the dimensional dispersion relation appears as it does in figure (4-11). Resonance occurs locations of the branch points of the Reimann sheets.

The purely imaginary values for the roots of k represent trapped energy - at the exact conditions of capillary and gravity mode resonance the energy does not travel away from its spatial location. However, in the neighborhood of this event (in $k - \omega$ space), when $k_R > 0$, energy does travel with the waves, albeit with the capillary wave mode significantly damped. This concept will be further elucidated in section 4.4.

It is important to note that the non–dimensional value of $k^* = \pm\sqrt{-\frac{1}{3}}$ (and the corresponding value of $\omega*$) at resonance is invariant with respect to the physical parameters, (g, σ_o, ρ) in the system (figure 4-13). The values of ω and k for resonance

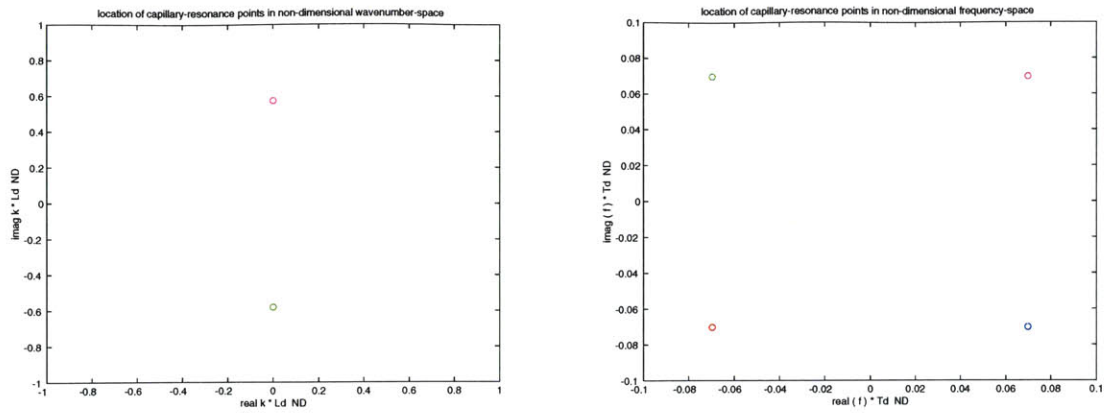

Figure 4-13: Locations of gravity–capillary resonance events in non-dimensional $k^* - f^*$ space. The values of $k^* = \pm\sqrt{\frac{1}{3}}$ and $f^* = \omega^*/2\pi = \pm 0.07(1 \pm i)$ are invariant with respect to the physical parameters of the system.

in any physical system governed by the simple form of Kelvin's dispersion relation are completely determined by the dimensional parameters, L_d and $T_d(L_d)$ as displayed in figures (4-14 – 4-15).

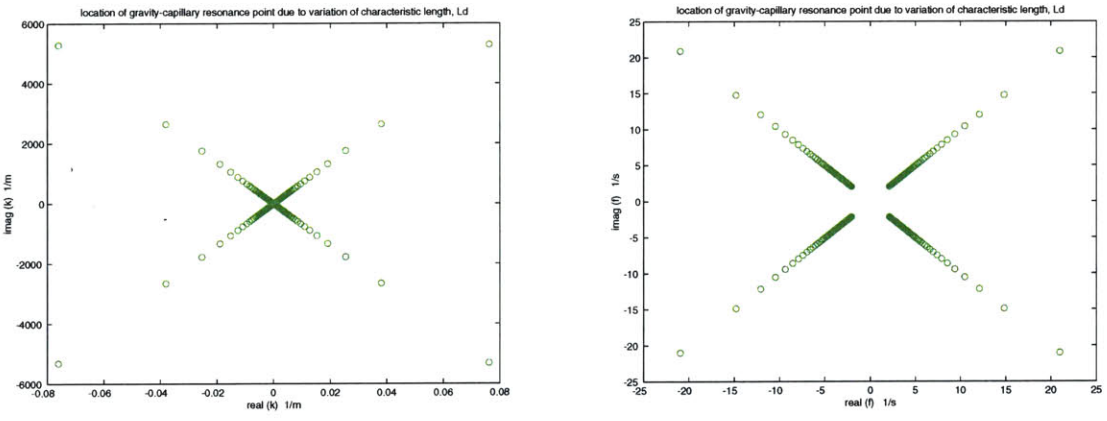

Figure 4-14: Locations of gravity–capillary resonance points in $f - k$ space due to variation of the length scale, $L_d = \sqrt{\frac{\sigma_o}{\rho g}}$.

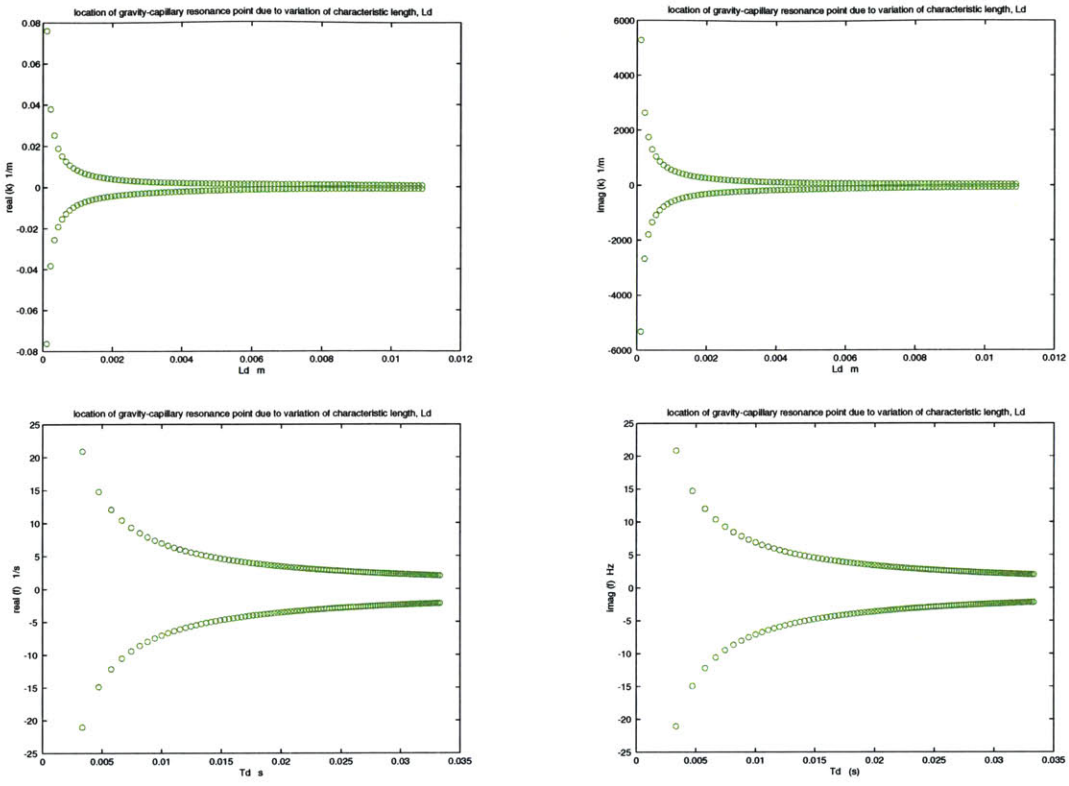

Figure 4-15: Locations of gravity–capillary resonance points in $f - k$ space versus variation of the length and time scales, L_d and T_d.

In these figures we see that increasing the dimensional parameter

$$L_d = \sqrt{\frac{\sigma_o}{\rho g}}$$

results in the gravity-capillary resonance points approaching the origin. An increase in surface tension or decrease in density thus result in resonance at lower frequencies and smaller spatial and temporal damping rates.

When surface normal viscosities are important in equations (4.14), then variation of σ', and thus τ, alters the location of resonance points in $f - k$ space, where $f = \omega/2\pi$. By varying σ' over 13 orders of magnitude from 10^{-7} to 10^5 we obtain the plots of resonance values of f and k for clean water shown in figures (4-16) and (4-18). In figures (4-16) we see four roots of equations 4.14. In actuality, there are

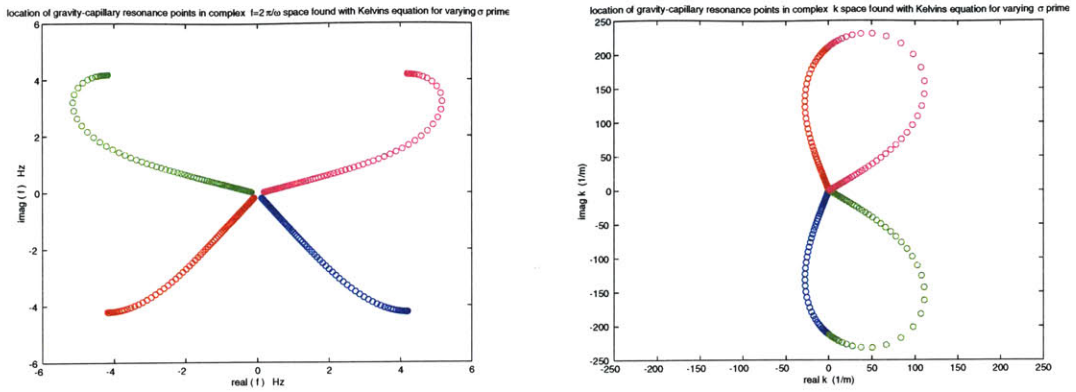

Figure 4-16: Location in $f-k$ space of gravity–capillary root coalescence (resonance) for water for variation of σ' in Kelvin's dispersion relation.

five, the fifth giving always $(real(\omega = 0))$, as these equations can be combined to give

$$i\tau\omega^{*5} + \omega^{*4} + \frac{4}{27} = 0 \qquad k^{*2} = -\frac{1}{3[1 + i\omega^*\tau]} \tag{4.16}$$

or

$$6\tau^2 k^{*5} + 9k^{*4} + 6k^{*2} + 1 = 0 \qquad \omega^* = \frac{i}{\tau}\left[1 + \frac{1}{3k^{*2}}\right] \tag{4.17}$$

The tips of the tentacles in figure (4-16a) are the locations are the values $f = \omega/2\pi = \pm 4.1914(1 \pm i)$ 1/s found for the negligible surface normal viscosity, σ'. As this value increases, all roots of the equations 4.16 or 4.17 converge to $(f = 0, k = 0)$.

The values of (f, k) satisfying equations 4.16 and 4.17 do not represent physical or stable modes themselves - all have either $Real(k) < 0$. $Imag(k) > 0$ or $Imag(f) > 0$. These resonance events do, however, effect physical modes. We see this, for example, when we examine the group speed of non-decaying waves governed by Kelvin's relation. The dip near 4 Hertz, we see in figure 4-17 is actually an avoided crossing. This is a real physical phenomenon and has been measured experimentally. Thus, physical and stable waves in the neighborhood of resonance point (ω, k), which itself may be representative of a non-physical or unstable wave, still feel its effect.

In figure (4-18) we see how the increase of the value of σ' affects the complex values

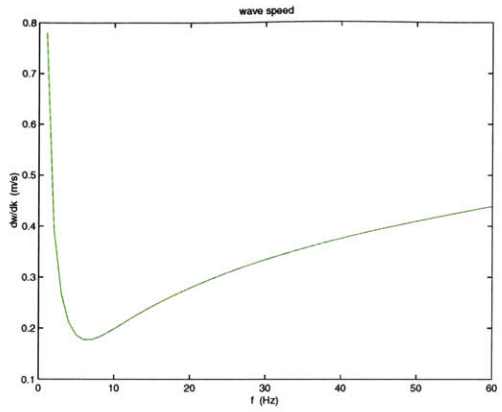

Figure 4-17: Group velocity, $\frac{\mathrm{d}\omega}{\mathrm{d}k}$ versus frequency, f, calculated by Kelvin's dispersion relation for "capillary-gravity" waves travelling at an air-water interface.

of k and $\omega/2\pi$. The greatest effect of σ' on these parameters occurs in the range $10^{-4} < \sigma' < 10^{0}$. In this range, the introduction of σ' results in modal resonance for increasingly small waves with a minimum length of $\lambda = 5.7$ cm for water corresponding to $Real(k) \approx 110$ 1/m. Concommitantly the frequency increases to nearly 5.5 hertz.

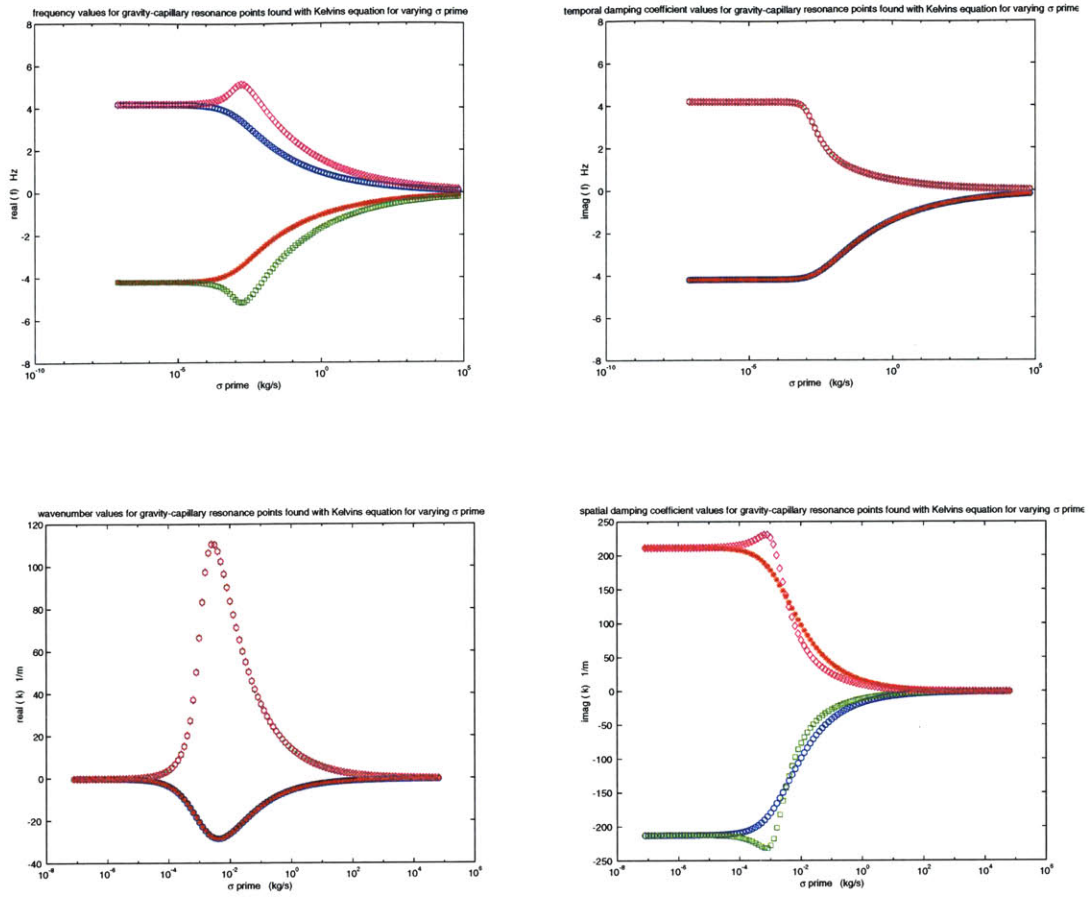

Figure 4-18: Location in $f-\sigma'$ and $k-\sigma'$ spaces of gravity–capillary root coalescence (resonance) for water for variation of σ' in Kelvin's dispersion relation.

4.3.2 Lamb's relation: effect of viscosity on capillary–gravity resonance

Lamb's dispersion relation adds the effect of viscosity to Kelvin's relation and thus provides a mechanism for the decay of the surface waves.

$$\omega^2 + 4\left(\frac{\mu}{\rho}\right)^2 k^2 m\,(m-k) = gk + \frac{\sigma k^3}{\rho} \qquad m^2 = k^2 + \frac{i\omega\rho}{\mu} \tag{4.18}$$

The solution to

$$\Delta = 0 \qquad \frac{\partial \Delta}{\partial k} = 0 \tag{4.19}$$

for Lamb's relation is not closed form. These equations were solved numerically as described in Appendix A.

The interesting result is that viscosity, μ has absolutely no effect on the location of the resonance points in (ω, k) space. Note figures (4-19) and (4-20). There is no variation of resonance point position for variation of μ and exactly the same variation of resonance point position for variation of σ' as with Kelvin's relation. (The scatter at each location is a result of the error bounds set in the numerical programs.) As we will confirm with our examination of Lucassen's relation, Kelvin's relation completely describes capillary-gravity resonance.

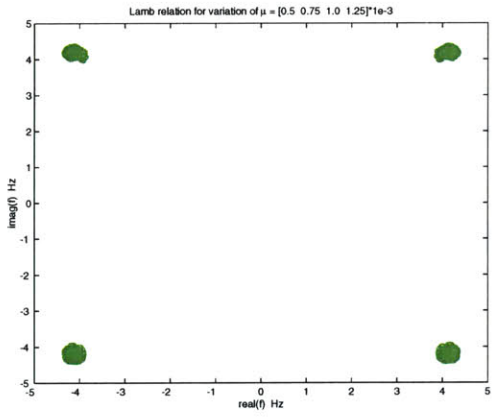

Figure 4-19: Location in f space of gravity–capillary root coalescence (resonance) for water for variation of μ by Lamb's relation.

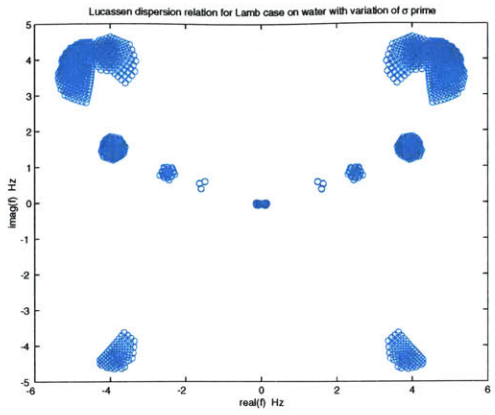

Figure 4-20: Location in $f-k$ space of gravity–capillary root coalescence (resonance) for water for variation of σ' for values of positive k by Lamb's relation.

4.3.3 Lucassen's dispersion relation: effects of an elastic film at the surface

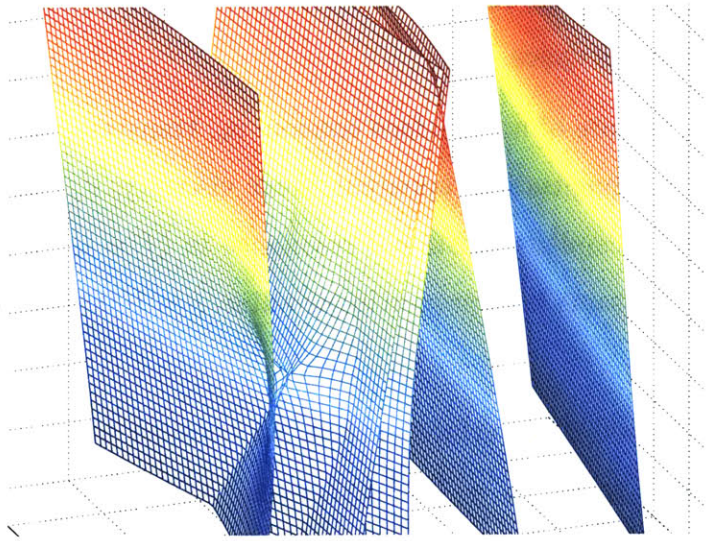

Figure 4-21: A closeup view of two capillary-dilational resonances and one capillary-gravity resonance in the projection of the the solution space of Lucassen's dispersion relation in $\omega - k$ space.

We now come to Lucassen's dispersion relation which adds the effects of elasticity and normal and transverse shear viscosities at the surface:

$$\Delta = [\mu(k-m) - \mu'(k-m')]^2 + E \cdot S = 0, \tag{4.20}$$

$$E = \frac{\epsilon k^2}{\omega} + i\left[\mu(k+m) + \mu'(k+m')\right],$$

$$S = \frac{\sigma k^2}{\omega} + i\left[\mu(k+m) + \mu'(k+m')\right] + \frac{g(\rho-\rho')}{\omega} - \frac{\omega(\rho+\rho')}{k}$$

$$m^2 = k^2 + \frac{i\omega\rho}{\mu}.$$

With the addition of elasticity in the dispersion relation, dilational wave modes appear. Two types of resonances are now possible: gravity-capillary resonance and capillary-dilational resonance. Gravity-dilational resonance does not appear to occur.

In figure (4-21) we can see both types of resonances occuring. The gravity-capillary resonance stretches the solution space far more than the capillary-dilational resonances. Thus the effects of gravity-capillary have a much wider neighborhood of influence. This implies that for capillary-dilational effects to be important in experimental and field measurements, these resonances will need to occur very close to the real ω and k axes in $\omega - k$ space.

To get a physical picture of how surface tension, σ_o, transverse shear viscosity, σ', dilational elasticity, ϵ_o, longitudinal apparent shear viscosity, ϵ', and bulk viscosity, μ effect the location of capillary-dilational resonance in $(f = \omega/2\pi) - k$ space, we examine a fluid with the same bulk properties as water, $\rho = 1000$ kg/m^3 and $\mu = 1e^{-3}$ kg/ms.

Beginning with the effect of surface tension, we consider a film covered fluid interface with $\rho = 1000$ kg/m^3, $\mu = 1e^{-3}$ kg/ms, $\epsilon_o = 10e^{-3}$ kg/s^2 and $\epsilon' = 1e{-}7$ kg/s. Surface tension, σ_o was varied over the range $[10 \;\; 50 \;\; 100]\, e^{-3}$ kg/s. Examining figure 4-22, we see that the gravity-capillary resonance points are visible near 4 hertz. Three capillary-dilational points appear between 4 and 9 hertz. The locations of these points are sensitive to surface tension, and a reduction in σ_o causes them to approach the real $f = \omega/2\pi$ and k axes .

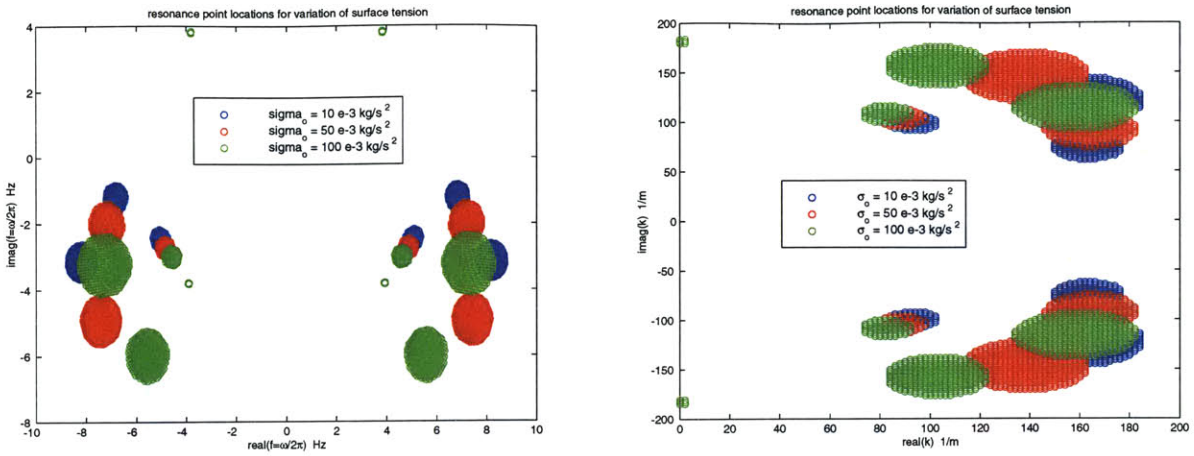

Figure 4-22: Location in f and k spaces of gravity–capillary and capillary–dilational root coalescences (resonance) for a visco-elastic fluid for variation of surface tension, σ_o.

Variation of dilational elasticity has the opposite effect as surface tension, increasing

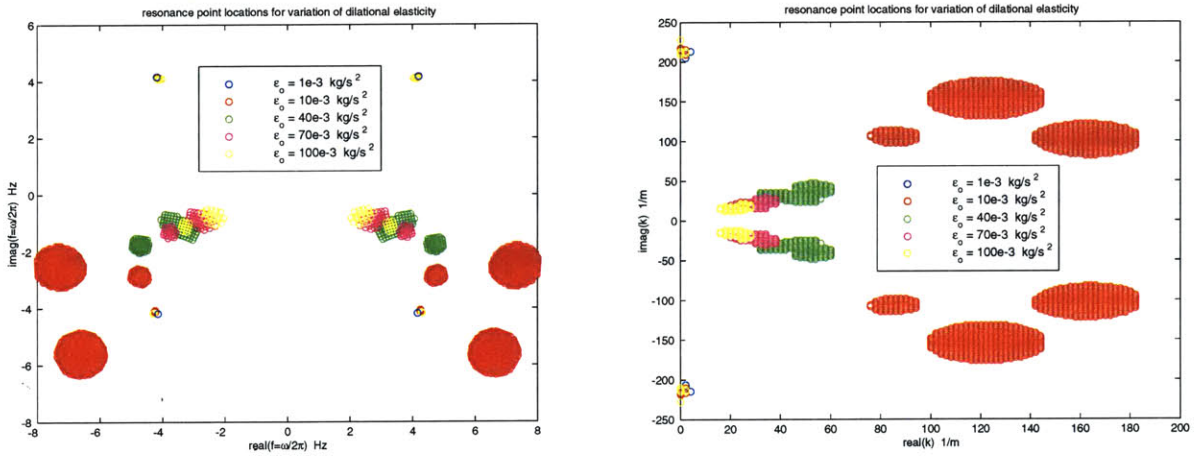

Figure 4-23: Location in f and k spaces of gravity–capillary and capillary–dilational root coalescences (resonance) for a visco-elastic fluid for variation of dilational elasticity, ϵ_o.

ϵ_o causes the cap-dil resonance points to approach the real $f = \omega/2\pi$ and k axes and converge toward the origin

Similarly to dilational elasticity, an increase of apparent dilational surface viscosity, ϵ', causes the cap-dil resonance points to approach the real $f = \omega/2\pi$ and k axes

and converge toward the origin.

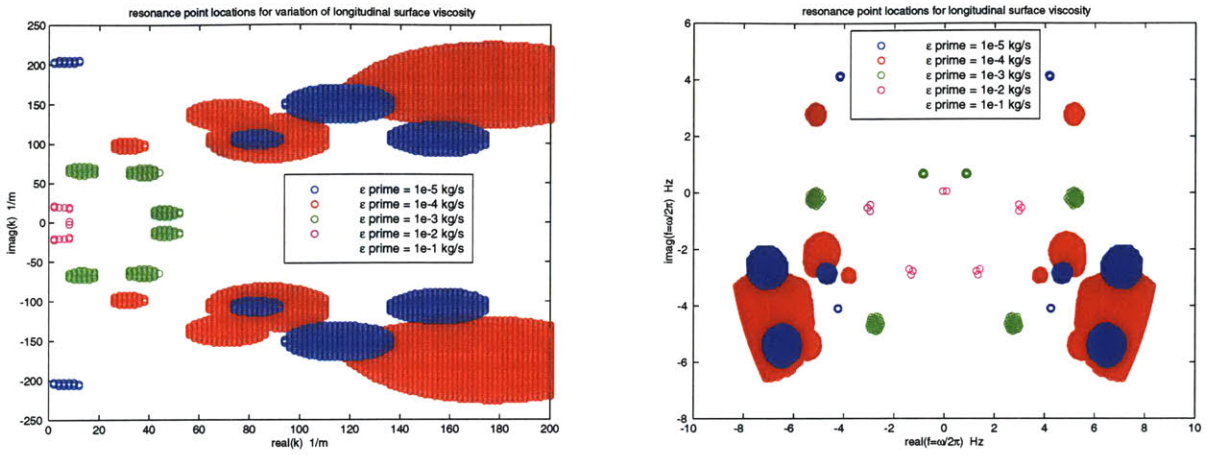

Figure 4-24: Location in f and k spaces of gravity–capillary and capillary–dilational root coalescences (resonance) for a visco-elastic fluid for variation of apparent dilational surface viscosity, ϵ'.

Note that in all of the figures in the section, the location of resonance points corresponding to gravity-capillary resonance (near 4 Hertz) is invariant with respect to parameter variation. There is no effect of surface elasticity or viscosity on gravity-capillary resonance and thus we can study this phenomenon simply by Kelvin's relation.

4.4 Effects of resonance

In section 4.2, resonance was described by coalescence between two roots of the dispersion relation. As will be presented below resonance affects modal group velocities, the transverse wave energy spectrum and can result in bifurcations of the wave modes.

4.4.1 Group velocity

There are three quantities for wave modes, the group velocity, Cg, and the spatial, k_I, and temporal, ω_I, damping coefficients which determine how the wave amplitude

diminishes in space and time, respectively. We have already seen that there are peaks and troughs of the damping rates near resonance, now we look at the effect of resonance on the group velocity.

The group velocity for fluid waves is defined as

$$Cg = \frac{\partial \omega}{\partial k} \tag{4.21}$$

For gravity-capillary waves, it can be calculated from Kelvin's relation

$$\Delta = 0 = -\omega^2 + kg + \frac{\sigma k^3}{\rho}. \tag{4.22}$$

Taking the partial derivative by k of each term in this equation we have

$$0 = -2\omega \frac{\partial \omega}{\partial k} + g + 3\frac{\sigma k^2}{\rho}. \tag{4.23}$$

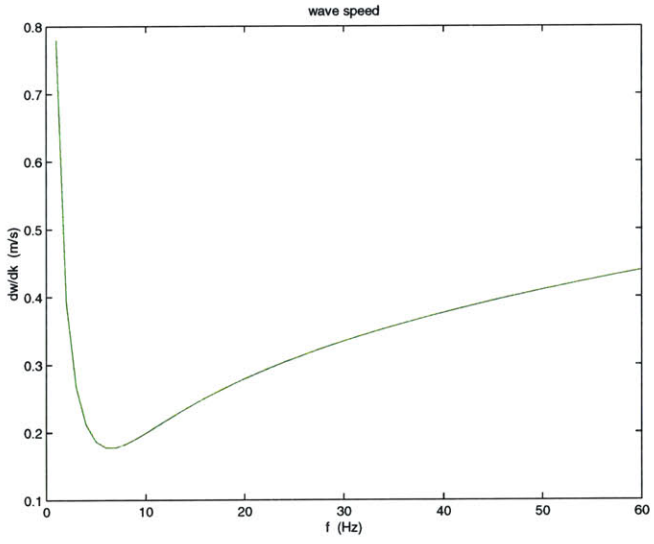

Figure 4-25: Group velocity, $\frac{d\omega}{dk}$, versus frequency, f, of capillary-gravity waves by Kelvin's relation.

which can be rearranged to give

$$\frac{\partial \omega}{\partial k} = \frac{1}{2}\left[\frac{g + 3\frac{\sigma k^2}{\rho}}{\omega}\right] \tag{4.24}$$

or, in terms of the dispersion relation,

$$\frac{\partial \omega}{\partial k} = \frac{1}{2}\frac{\partial \Delta}{\partial k}\frac{1}{\omega}. \tag{4.25}$$

As the conditions for root coalescence are defined by

$$\Delta = 0 \qquad \frac{\partial \Delta}{\partial k} = 0 \tag{4.26}$$

then at resonance, the group speed of the waves

$$Cg = \frac{\partial \omega}{\partial k} = 0. \tag{4.27}$$

is zero.

We see this effect in the plot of group speed versus frequency for undamped capillary-gravity waves traveling at an air-water interface. The dip near 4 Hertz is due to resonance between the capillary and gravity modes at $k = \pm 212.08i$ 1/m and $\omega/2\pi = \pm 4.1914(1 \pm i)$ 1/s. The group velocity is approaching zero. These waves are produced for physical conditions in the neighborhood of resonance conditions and thus experience a reduced group velocity.

When there is capillary-dilational resonance as well as gravity-capillary resonance, we can expect to see two dips in the plot of group speed versus frequency as shown in figure 4-26. This figure also displays curves for an air-water and and air-viscous bulk fluid interface which have only a single dip corresponding to gravity-capillary resonance. The viscoelastic interface has the same values for the rheological parameters as given in section 4.2.2, $\sigma_o = 27.7 \times 10^{-3}$ kg/s^2, $\sigma' = 0.542 \times 10^{-5}$ kg/s, $\epsilon_0 = 59.1 \times 10^{-3}$ kg/s^2,$\epsilon' = -70.4 \times 10^{-5}$ kg/s, $\rho = 940$ kg/m^3 and $\nu = 14.1 \times 10^{-6}$ m^2/s. The air-viscous bulk fluid interface shares these values as well, but with no

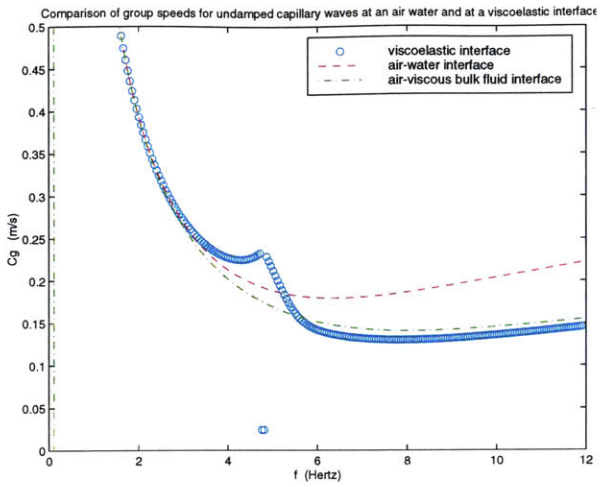

Figure 4-26: Comparison of group speed, $\frac{d\omega}{dk}$, versus frequency, f, of "capillary-gravity" waves at air-viscoelastic (Lucassen's relation), air-viscous bulk fluid (Lamb's relation) and air-water (Kelvin's relation) interfaces.

surface elasticity or viscosity. The air-water interfacet is only dependent on surface tension, $\sigma_o = 72.7 \times 10^{-3}$ kg/s^2, and density, $\rho = 1000$ kg/m^3.

In comparing the curves in figure 4-26 of group velocity versus frequency for the visco-elastic and air-viscous bulk fluid interfaces to that of water, we see that there is a diminuation of the group speed for frequencies greater than 5.5 Hertz. Because the surface tension of this fluid is relatively smaller to that of water, the location of the gravity-capillary root coalescence point is closer to the real frequency axis and thus its effect on neighboring frequencies is larger.

Furthermore, the curve for the visco-elastic interface has two dips. The first dip occurring near 4 Hertz corresponds to resonance between the capillary and gravity modes. The second dip occurring near 5.5 Hertz corresponds to resonance between the capillary and dilational modes. The single point near zero is a numerical artifact. Thus both modal resonances causes a dips in the group velocity.

4.4.2 Energy spectrum

The effects of resonance can also be seen on the transverse wave energy spectrum. A good demostration of this is a measured wind-wave energy spectrum. These spectra show the amount of transverse wave energy at each frequency transported downstream of some forcing location. Figure 4.4.2 shows four plots taken from a study by Huhnerfuss *et al.* (1985) in which wave spectra for clean water and for water with various surface films were developed by wind forcing on a flume.

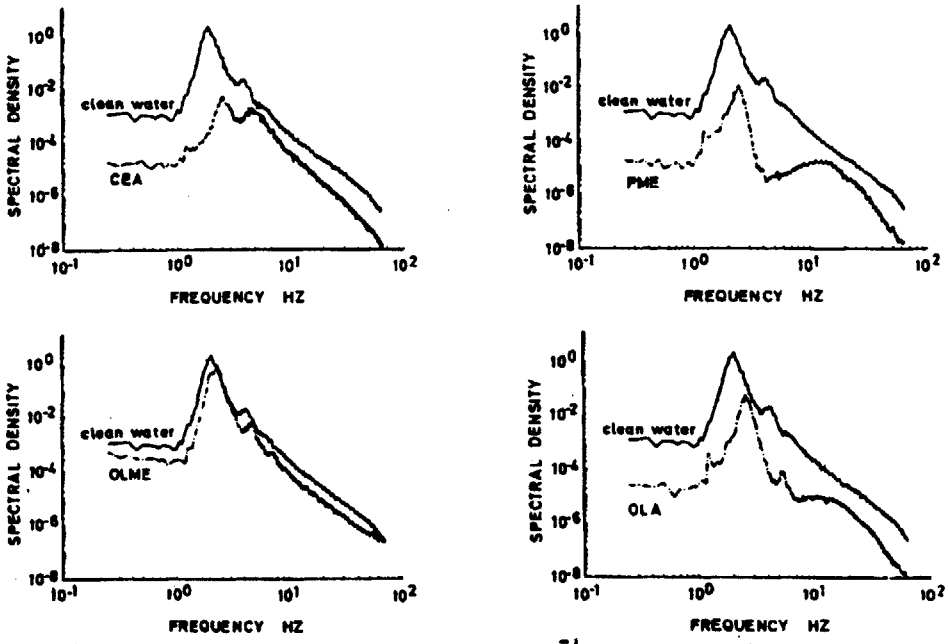

Fig. 1. Wind wave spectra (wind speed U = 8 ms^{-1}, fetch about 16 m, degrees of freedom 66) of a clean water surface (solid lines), and in the presence of a hexadecanol (CEA), hexadecanoic acid methyl ester (PME), 9-octadecenoic acid methyl ester, Z-isomer (OLME), and 9-octadecen-1-ol, Z-isomer (OLA) surface film.

Figure 4-27: Wind-wave spectra for clean water and four surfactants on water from a study by Huhnerfuss *et al.* , 1985.

In every plot, both for the clean water and surface film spectra, there is a dip near 4 Hertz corresponding to capillary-gravity resonance. This dip shows that there is less energy transported down flume at this frequency than at its neighboring frequencies. The spectrum for OLA has a clear double dip, one near 4 Hertz and another near 6 Hertz. The second dip corresponds to capillary-dilational resonance. The spectrum

for PME has a very large dip extending from 4 Hertz to 6 Hertz. This can have two meanings. The location of the gravity-capillary root coalescence point is dependent on surface tension, a significant decrease in surface tension can increase the effect of gravity-capillary resonance on the group speed for nearby frequencies. A second possibility is that this surfactant has properties whereby several capillary-dilational resonances happen in the 4-6 Hertz range. This is also possible. The other two surfactants studied by Huhnerfuss *et al.* do not appear to introduce conditions conducive to capillary-dilational resonance.

4.4.3 Mode bifurcation

Gravity-capillary resonance is accompanied by a bifurcation of the gravity mode below 4 hertz into two inadmissible modes above 4 hertz and a unification of two inadmissible modes below 4 hertz into a capillary mode above 4 hertz.

Figure (4-28) is a simple illustration to demonstrate approximately when each of the five wave modes is admissible $Re(k) > 0$. Below approximately four hertz for common rheological conditions, there is generally one dilational and one gravity wave, and above four hertz, there is generally one capillary and one dilational wave.

Admissibility, $Re(k) > 0$, does not also imply stability, $Im(k) < 0$. The dilational wave is not always stable below four hertz for fluid interfaces of common rheology and thus it is generally only the gravity mode which is apparent. In this case, all of the wave energy travels in a gravity mode below 4 hertz and in both a capillary and a dilational mode above 4 hertz. This means that below 4 hertz, all of the energy travels as a transverse wave and above four hertz only some of the energy travels as a transverse wave. As it is only the transverse wave component which is measured with a wave gauge, necessarily, there will be a dip in the wave spectrum when modal bifurcation occurs. Thus the dip at 4 hertz is a function of modal bifurcation.

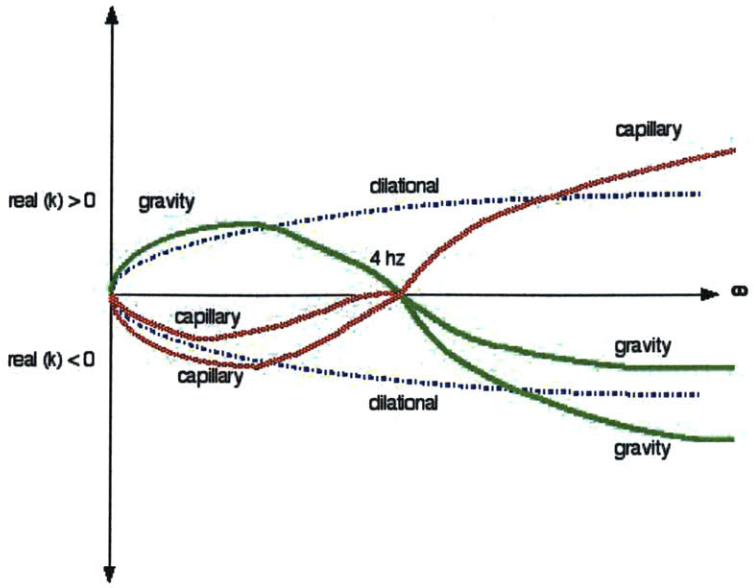

Figure 4-28: A rough sketch of dependence of the admissibility of the five wave modes on frequency.

4.5 Comparison of wave mode resonance to vibration absorption

There is a very strong parallel between the redistribution of energy between coupled interfacial fluid wave modes due to mode coalescence and the redistribution of energy between coupled oscillators in mechanical systems due to vibration absorption at natural frequencies. Both systems experience a decrease in the amplitude of the motion of one mode (or mass-spring system) with an increase in the amplitude of the motion of the coupled secondary mode (or mass-spring system).

In a mechanical system, a secondary mass-spring system is often used to absorb energy at the natural (resonant) frequency of the primary system. Figure 4.5 shows a vibration absorber coupled to a primary system.

Following the development in Rao (2004), the primary system has an equation of motion,

$$m_1\ddot{x_1} + k_1 x_1 = F_o \sin \omega t. \tag{4.28}$$

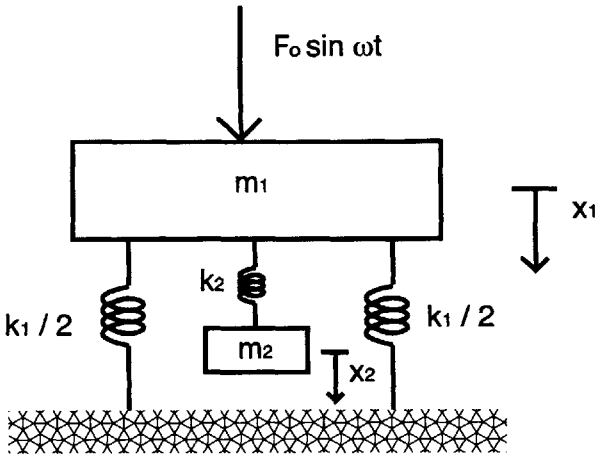

Figure 4-29: Undamped dynamic vibration absorber, $m_2 - k_2$, coupled to a primary oscillator, $m_1 - k_1$. The secondary system reduces the vibratory response of the primary system at its natural frequency.

When the vibration absorber is added, the equations of motion become,

$$\begin{aligned} m_1\ddot{x}_1 + k_1x_1 + k_2(x_1 - x_2) &= F_o \sin\omega t \\ m_2\ddot{x}_2 + k_2(x_2 - x_1) &= 0. \end{aligned} \tag{4.29}$$

Assuming harmonic solutions,

$$x_j(t) = X_j \sin\omega t \qquad j = 1, 2 \tag{4.30}$$

the responses of the two oscillators are found to be

$$\begin{aligned} \frac{X_1}{\delta_{st}} &= \frac{1 - \left(\frac{\omega}{\omega_2}\right)^2}{\left[1 + \frac{k_2}{k_1} - \left(\frac{\omega}{\omega_1}\right)^2\right]\left[1 - \left(\frac{\omega}{\omega_2}\right)^2\right] - \frac{k_2}{k_1}} \\ \frac{X_2}{\delta_{st}} &= \frac{1}{\left[1 + \frac{k_2}{k_1} - \left(\frac{\omega}{\omega_1}\right)^2\right]\left[1 - \left(\frac{\omega}{\omega_2}\right)^2\right] - \frac{k_2}{k_1}} \end{aligned} \tag{4.31}$$

where

$$\delta_{st} = \frac{F_o}{k_1} \qquad \omega_1 = \left(\frac{k_1}{m_1}\right)^{1/2} \qquad \omega_2 = \left(\frac{k_2}{m_2}\right)^{1/2} \tag{4.32}$$

If the the absorber is designed so that

$$\omega_2 = \omega_1, \tag{4.33}$$

then the amplitude of the vibration of the machine operating at its natural frequency will be zero.

Figure 4-30 shows the difference in the response of the primary system with and without the absorber. The green line shows the response to periodic forcing of the primary system without the absorber. The blue line shows the response of the primary system with the coupled absorber and the red line shows the response of the absorber to the periodic forcing. The effect of the dynamic absorber at the system is to redistribute energy from the primary system to the secondary system at the natural frequency of the primary system, ω_o. At frequencies much smaller or greater than this frequency, the effect of the of the dynamic absorber on the primary system is negligible. At the natural frequency of the primary system, the effect is to reduce the response from infinite to zero. Near the natural frequency, there are now two new resonant peaks of response, one at a slightly higher and the other at a slightly lower frequency.

Like coupled fluid wave modes, a measurements of the response of only the primary oscillator in the mechanical system will show a dip at the resonant frequency of vibration absorption by the secondary oscillator.

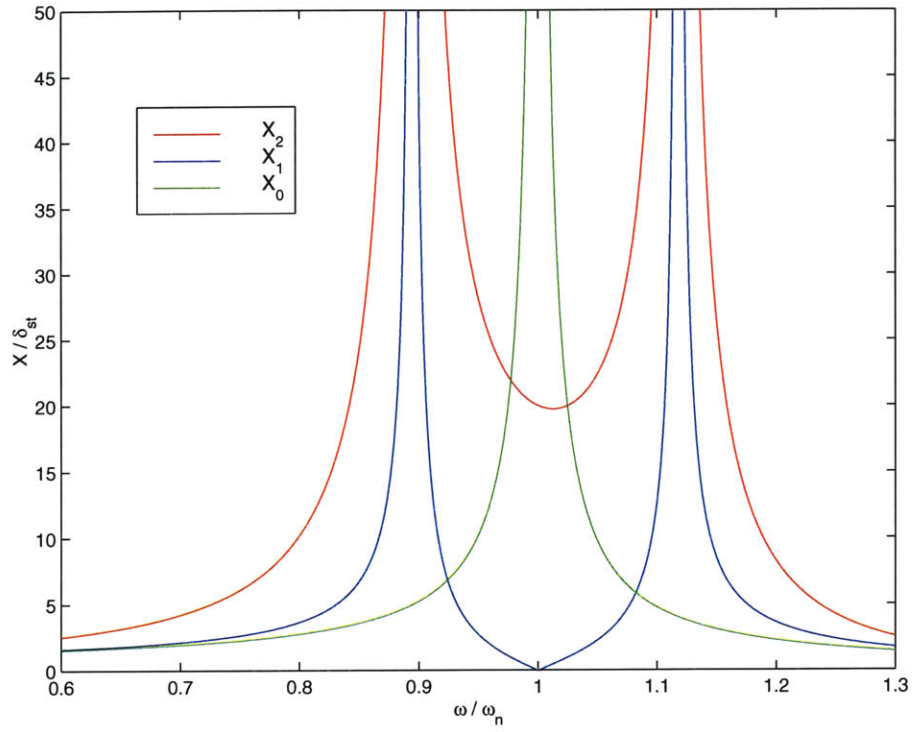

Figure 4-30: The ratios of the dynamics to static responses of the primary system, X_o/δ_{st}, primary system with vibration absorber, X_1/δ_{st} and secondary system (vibration absorber), X_1/δ_{st} versus the ratio of frequency to the natural frequency of the primary system, ω/ω_o.

Chapter 5

Experimental measurements of viscoelastic capillary waves

In the preceding chapters, wave mode resonance was described analytically and its dependence on surface rheology characterized numerically. In the following chapters, it is shown how resonance phenomena manifest themselves physically.

Experimental demonstration of resonance requires measurements of waves at a visco-elastic interface and either good fortune or a foreknowledge of which two-fluid systems possess the interfacial rheology for conditions amenable to measuring resonance phenomena.

While there is a great body of literature wherein are published rheological parameters for two-fluid systems, finding a complete set of these parameters in the 3-11 hertz range (where resonant behavior is expected) proved extremely difficult. This limited any foreknowledge of conditions amenable to resonance to the very few fluid systemss for which published wave data showed evidence of resonance phenomena. We found only two such data sets. We used the same fluid as one of the published data sets, and made our own measurements successfully showing the effects of both gravity-capillary and capillary-dilational resonances.

In an attempt to find additional fluid systems which might provide amenable conditions for measuring resonance phenomena, we developed an inverse method whereby the rheological parameters describing the visco-elastic interface are found from wave

data. In addition to its usefulness in studying resonance, the inverse method provided a powerful tool for determining all surface rheological parameters simultaneously at the low end of the frequency spectrum where information about surfactants at the ocean surface would be most needed. With a complete set of rheological parameters, we could use our analysis in chapter 4 to determine if resonance phenomena would be discernable for accessable experimental conditions. We applied the inverse method to experimental measurements several fatty acids monolayers on distilled water with mixed results for showing resonance.

Chapter 5 dicusses the methodology of obtaining wave measurements and presents the results for three different two-fluid systems. Chapter 6 presents the inverse method and its application to the experimental measurements. Chapter 7 presents experimental evidence of wave mode resonance phenomena.

5.1 Literature review

The earliest measurements of ripples (capillary waves) appears to be by Lord Rayleigh, (Thompson, 1871) for the determination of surface tension. This method used a stroboscope to measure the lengths of the waves and then employing these measurements in Kelvin's dispersion relation, determined the surface tension. Measurements of capillary waves for this purpose and using similar methods continued with Dorsey (1897), Watson (1901), Brown(1936), etc. Brown's measurements are particularly interesting because they give the damping coefficient of capillary waves on distilled water. Data of wave damping coefficients and wave numbers are rare.

A few other authors who made measurements of wave number, spatial damping coefficient or wave velocity are Goodrich (1961), Mann & Hansen (1963), Garrett (1963), Lucassen & Hansen (1967) and Bock (1987). These authors largely used laser slope meter or electrical potentiometers to measure the wave characteristics.

Experimental measurements of frequency and temporal damping coefficient were made by Høard and Neuman (1986) and Earnshaw *et al.* (1988) using light scattering techniques.

Bock (1987) and Hühnerfuss (1985) had experimental wave data which showed the effects of resonance.

Measurements of rheological parameters are wide spread and use a variety of techniques. It is worth noting that only light scattering techniques return a complete set of parameters simultaneously (without having to resort to more than one measurement technique to get them). Light scattering has, however, two drawbacks: one, it uses an approximation of the dispersion relation to determine the parameters; and, two, it only gives information rheological behavior at high frequencies. As rheology is frequency dependent, this means that this information is not useful for understanding rheological behavior at the low frequencies we are interested in studying.

There are several methods by which which the parameters we measure may be obtained. The Gibb's or static elasticity is generally measured by use of a Langmuir-Blodgett trough (Langmuir, 1917, Adam, 1922, Adam & Jessop, 1926, Adam & Harding, 1932). When the barrier is oscillated dynamically, this method estimates the dynamic elasticity.

Complex elasticity combining elastic, relaxational and viscous effects has been estimated using surface wave methods. Generally when capillary wave methods (both mechanical and electrocapillary) are used, the relaxational and viscous effects are ignored (Bock, 1987, Jayalakshmi *et al.* 1995, Giermanska-Kahn *et al.* , 1999). Longitudinal wave methods use an approximation to the dispersion relation for this wave mode and relate longitudinal wave characteristics to the complex elasticity (Mass & Milgram, 1998, Liu & Duncan, 2003). Light scattering methods observe both longitudinal and transverse waves (dilational and capillary) and related the scattered intensity and frequency to a computed power spectrum of the waves. This power spectrum is related to the dispersion relation of the waves and from this the various rheological parameters are estimated. Authors employing this method include Langevin & Griesmar (1980), Langevin (1981), Høard and Neuman (1986), Earnshaw & McGivern (1987) and Earnshaw *et al.* (1988). Other authors used the oscillating bubble method (Wantke *et al.* 1998).

The inverse method we developed is capable of determining the surface dilational

elasticity, surface normal shear viscosity and an apparent viscosity combining the surface relaxational elasticity, surface tangential shear viscosity and surface tangential dilational viscosity simultaneously at the low frequencies found for ocean waves.

5.2 Description of experimental set-up

5.2.1 Laboratory equipment

Measurements were taken of planar capillary waves travelling at water-air interfaces with monolayers of myristic and palmitic acids and at an air-pentaerithritol ester interface with the aid of laser slope meters, a method pioneered by Sohl *et al.* (1978). Wavelength and damping ratio were measured in the 3-10 Hertz frequency range.

The experimental set-up included a polyeurithane tank and lid with optical glass inserts with optical coatings to account for the index of refraction between glass and air. This tank was supported by four legs on an optical mounting plate. The mounting plate was suspended on a Bosch frame that rested on a vibration isolation table. The table was not floated using its pneumatic system as this would produce seiching of the liquids in the tank. The benefit of the vibration isolation table was weight - at 500 pounds, most high frequency vibrations in the floor were damped out.

On the optical mounting plate were optical equipment rails by which two helium-neon can lasers on kimball mounts with positioning micrometers could be positioned along the length of the tank. The kimball mounts together with the positioning micrometers and the optical rail allow for two-dimensional lateral positioning and three-dimensional angular positioning.

Above the tank was mounted an upside down rail on which was attached two position sensing diodes (PSD's) on kimball mounts with positioning micrometers.

Waves were produced at one end of the tank by a polyeurithane blade nearly the width of the tank with a 45 degree triangular cross section. The blade was forced by an audio speaker to which was attached a cigar tube stabilized by a ring of balsa wood. The audio speaker was mounted independently of the Bosch framing and the

isolation table to insure that no mechanical vibrations affected the measured signal.

Figure 5-1 shows the tank, wavemaker and optics measurement system.

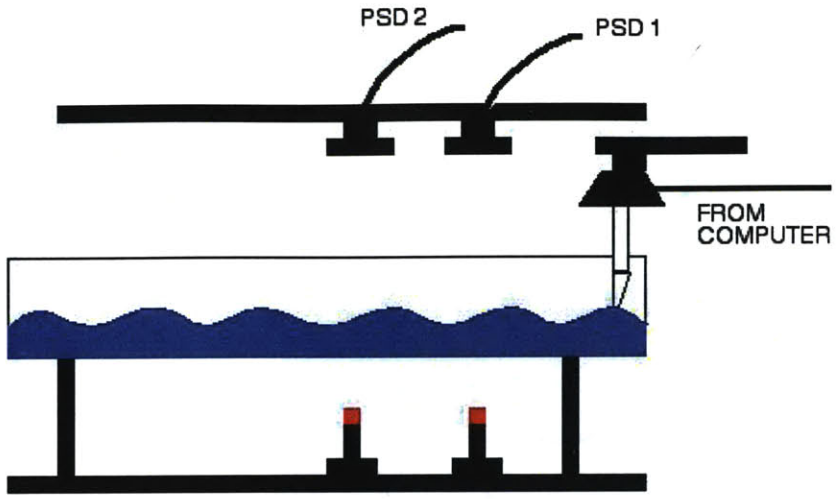

Figure 5-1: The tank, optics and wavemaker set-up.

The audio speaker was driven by a signal from a lock-in amplifier routed through an audio amplifier by which its amplitude was controlled.

The two PSD's captured the laser signals and transmitted via two currents to a combiner box which combined the two current signals and sent them to a PSD amplifier which converted the current signal to two voltage signals. This signal was then routed through an oscilloscope to the lock-in amplifier for analysis. The results of this analysis were then downloaded to a computer.

Figure 5-2 shows the route of the data signals from the PSD's to the combiner box, PSD amplifier, oscilloscope, lock-in amplifier and computer. It also show the signal from the lock-in amplifier to the audio speaker.

The wave signal is captured as follows. First the lasers are aligned so that their beams pass through a small pinhole at the emission point of the laser, the optical glass in the bottom of the tank, the fluid in the tank and the optical glass at the top of the tank, finally impinging on the PSD surface where they are reflected and pass back through all of the above media until the return beam comes back identically to the pinhole. The lasers are focused on the PSD surfaces.

When a wave travels down the tank, the laser beam is refracted. This refraction

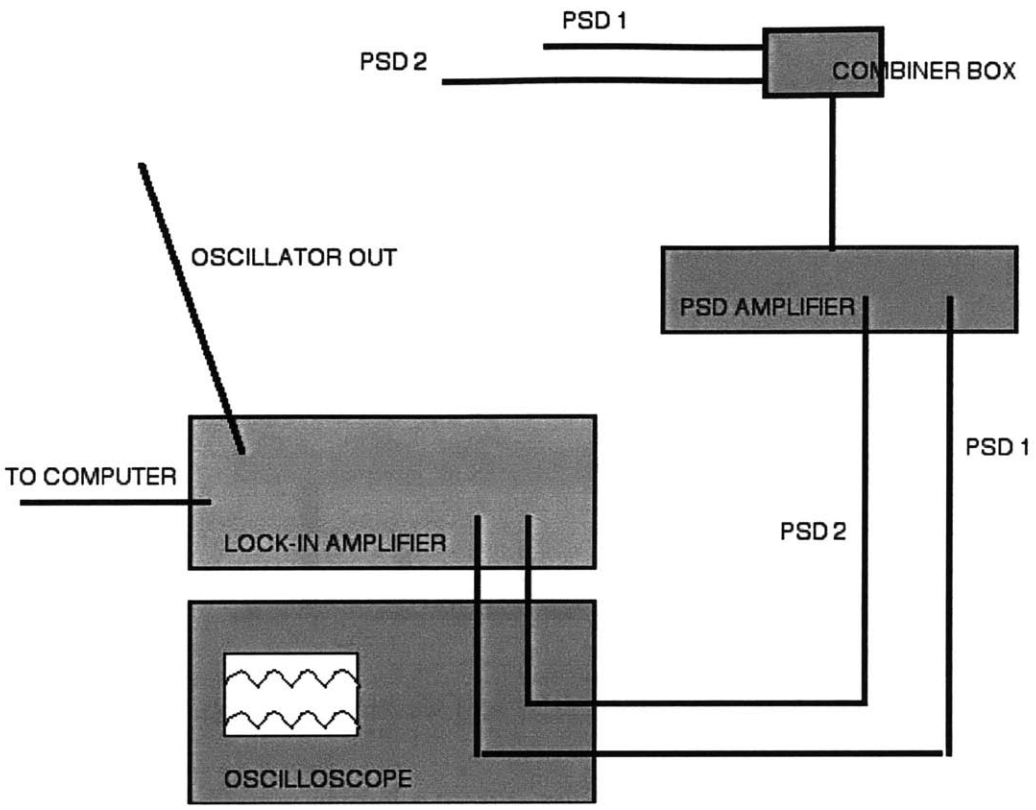

Figure 5-2: The signal routing from the PSD's to the combiner box, PSD amplifier, oscilloscope, lock-in amplifier and computer.

causes the beam to describe a sinusoidal excursion on the face of the position sensing diode as depicted in figure 5-3.

The PSD consists of a photo-sensitive silicon diode wafer which acts as a variable resistor. The laser impinging on the surface acts as a voltage, the lengths of the PSD from the point of impingement to the two ends provide variable resistance resulting in two currents, $C1$ and $C2$ as shown in figure 5-4.

The PSD circuitry then combines these currents so that

$$I = \frac{1}{2}\frac{C1 - C2}{C1 + C2}. \tag{5.1}$$

The signals from each PSD are eventually routed to the lock-in amplifier where they are analyzed. The phase lock-in amplifier has multiple functions in this experimental set-up. It both provides an oscillatory signal (oscillatore out) which drives

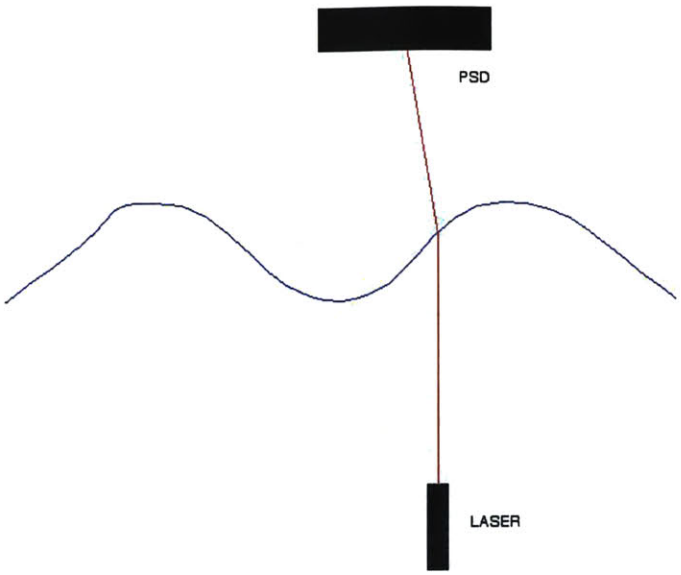

Figure 5-3: Refraction of the laser beam by the passing wave.

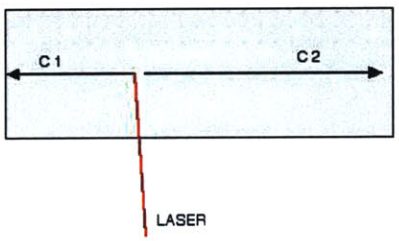

Figure 5-4: PSD operation. The impinging laser beam causes two currents on the variable resistance photo diode detector. The variable resistance is due to the difference in distance from the laser beam to each of the two ends of the detector.

the wavemaker speaker and extracts signal phase and magnitude information at the same frequency as the oscillator out signal.

The lock-in amplifier uses a combination of digital and analog technology for extremely low-noise analysis. A block diagram of this instrument is shown in figure 5-5.

In addition to the wave measurements, surface tension measurements were taken. The measurements were made with a Wilhelmy plate suspended from a high precision balance. The Wilhelmy plate is a small platinum blade which can be attached at one end to a wire. Surface tension is calculated from the maximum force required to

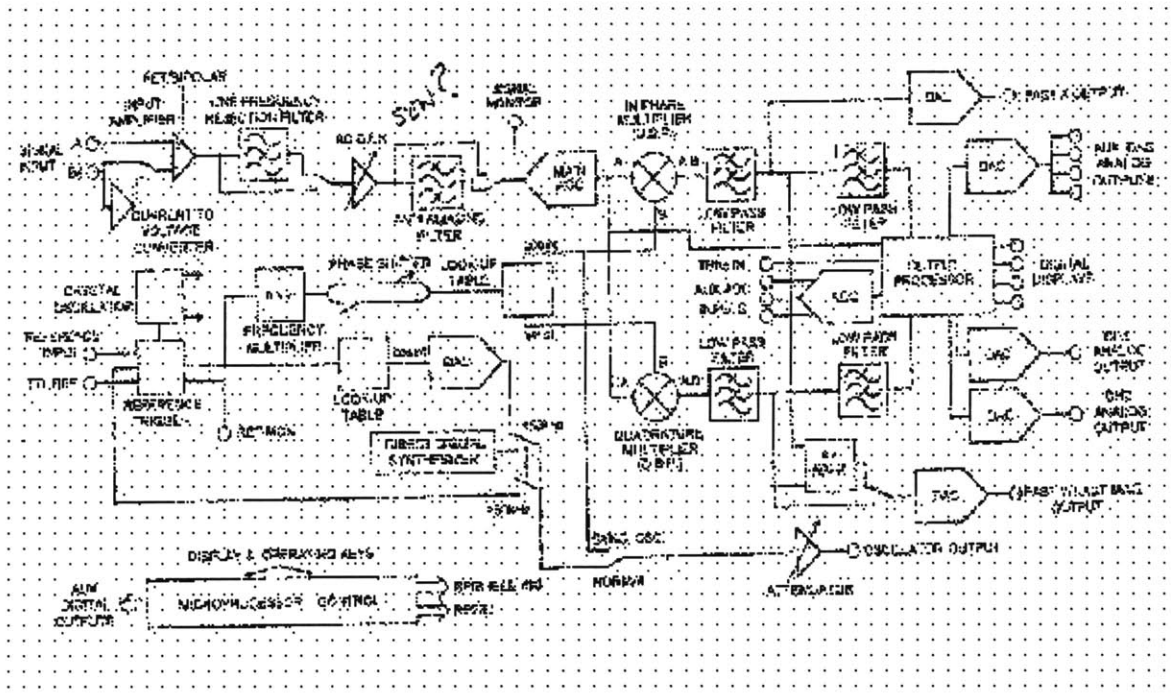

Figure 5-5: Block diagram of lock-in amplifier internal circuitry.

detach the blade from the fluid surface. The balance rests on a platform which could be raised and lowered thus raising and lowering the Wilhelmy plate as shown in figure 5-6.

Surface pressure versus surfactant concentration measurements were made with the aid of an *in-situ* Wilhelmy-Blodgett trough as shown in figure 5-7. This trough can be lowered onto the surface from within the closed tank. It consists of a circular teflon ring with a fixed radial barrier and a movable radial barrier. The movable barrier is controlled via twisting a long rod which extends through the top of the tank. Degrees are marked on the inside edge of the teflon circle so that amount of surface compression can be known.

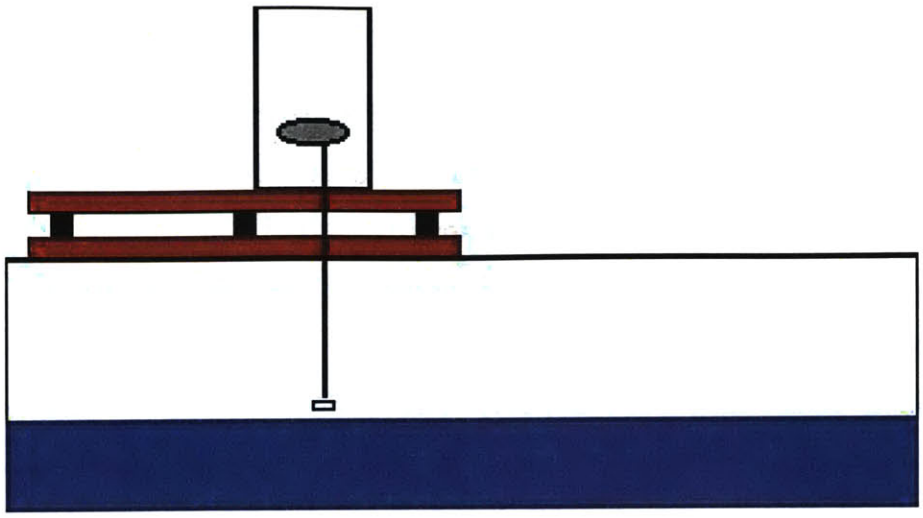

Figure 5-6: Wilhelmy plate - balance set-up.

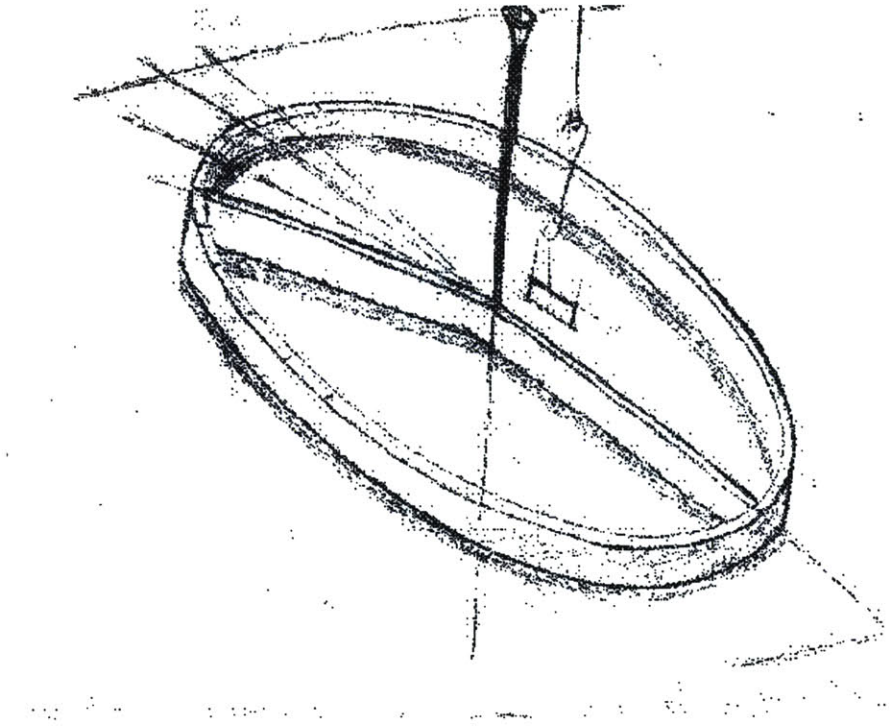

Figure 5-7: In-situ Wilhelmy-Blodgett trough

5.2.2 Extra-laboratory measurement equipment

The laboratory set-up did not include equipment for measuring density or viscosity, nor surface tension as a function of temperature. Measurements of these quantities were made in two other laboratories on campus.

Density was calculated from the specific gravity of the fluid. The specific gravity of the sample was determined using a 10 mL glass pycnometer or specific gravity bottle (Kimble Glass, Inc., Vineland, NJ). This device consists of a small spouted beaker outfitted with a thermometer cap. The beaker is weighed when empty, when filled with distilled water and when filled with the bulk fluid. The fractional weight of the fluid with respect to that of the distilled water gives the specific gravity of the fluid from which the density is easily calculated. The beaker containing the water and the bulk fluid was heated in a water bath to give the specific gravity of water at a variety of temperatures. The spout allows the excess fluid to escape as it expands with temperature, keeping a constant volume for both water and the bulk fluid in the beaker.

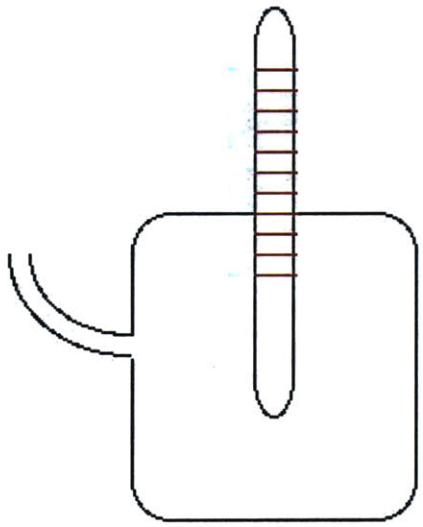

Figure 5-8: Pycnometer.

Dynamic viscosity measurements were made with the aid of a rheometer. The fluid is placed in the gap between two circular plates one of which rotates (usually the upper plate). From a measurement of the torque, T and the angular velocity $\dot{\gamma}$

one can find the viscosity

$$\nu(\dot{\gamma}) = \frac{T/2\pi R^3}{\dot{\gamma}} \cdot \left[3 + \frac{d\ln\left(T/2\pi R^3\right)}{d\ln\dot{\gamma}}\right] \tag{5.2}$$

where R is the radius of the circular places and $\dot{\gamma} = \omega_o R/H$ is the angular velocity of the upper disk with a separation distance of H.

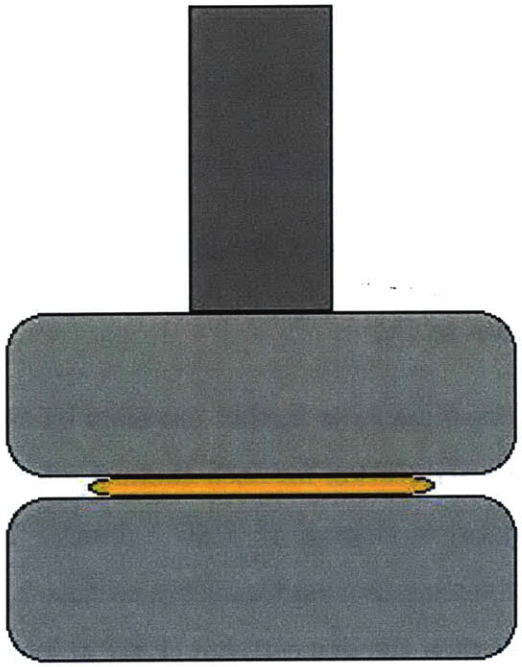

Figure 5-9: Rheometer.

Temperature dependent measurements of surface tension were made with a Kruss K11 tensiometer (Kruss USA, Charlotte, NC) and a platinum Wilhelmy plate. The plate was brought in contact with the sample and the surface tension determined from the resulting force, which is measured by a high-precision force balance. The temperature of the sample was regulated by a sample jacket through which water was pumped from a thermostatically controlled Neslab Model RTE-211 water bath (Neslab Instruments, Inc., Newington NH).

5.3 Description of experimental and data processing methods

5.3.1 Serial communications with the lock-in amplifier

The functions of the lock-in amplifier are controlled via serial communications with a PC. A program was written in C++ to control a multitude of functions. It

- starts and stops the wave maker
- sets the amplitude and frequency of the oscillation of the wave maker
- sets time length of data acquisition for each channel (data from two PSD's)
- sets which types of data will be downloaded
- downloads lock-in data to PC

The amplitude of the wave maker is further modified by the stereo amplifier.

The time length of data acquisition for each channel refers to the need to switch from channel A (PSD 1 data) to channel B (PSD 2 data) . The lock-in amplifier is unable to take data at both channels simultaneously, so data is taken at the upstream location (PSD 1) first, and then the downstream (PSD 2) location. The total length of time for data acquisition is less than the time before reflection of the wave from the far end of the tank returns the wave to the downstream location (PSD 2).

Early experimental measurements used this PSD switching technique to take data. Later measurements were made without switching channels. These data sets were aquired by taking data at a single location with a PSD/laser combination and then moving the combination to a different location and taking data there.

The lock-in amplifier has 20 different options for data taking. Four of them are employed in our experiments: signal magnitude, signal phase, sampled signal from PSD1, sampled signal from PSD2. The signal magnitude and phase are the lock-in's analysis of the sinusoidal signals from the two PSDs. The sampled signals are 200 hertz samples of each of the PSD signals.

5.3.2 Analysis of data

The transverse waves produced in the tank refract the laser beams, the excursion of the incident beam on the position sensing diode results in a current which is translated into a voltage signal and fed into the lock-in amplifier. The lock-in amplifier both samples this signal and using its internal circuitry, calculates its magnitude and phase.

A typical sampled signal is shown in figure 5-10.

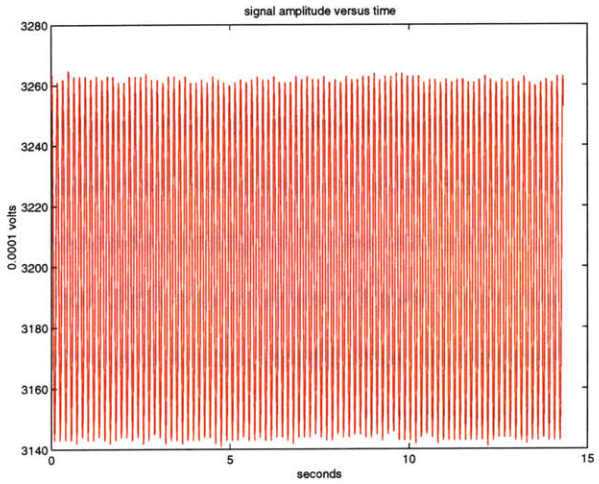

Figure 5-10: Sampled voltage signal in ten thousandths of a volt versus time in seconds.

To verify that the lock-in's magnitude and phase outputs were correct, sampled signals were analyzed via a signal processing program written in Matlab and the magnitude and phase of the signal relative to the wave maker motion were determined. The lock-in magnitude and phase outputs well matched the results from the signal processing.

5.3.3 Analysis of magnitude and phase data

Data collation

For every wave frequency measured, the lock-in amplifier produces data curves of magnitude and phase versus time. The magnitude, phase and sampled signal data for each of these measurements is downloaded to the PC. For early experimental runs which use the channel switching technique, these data appear as the do in figure (5-11) with the first level after two seconds corresponding to the magnitude or phase of the signal at PSD 1 and the second level corresponding to the magnitude or phase of the signal at PSD 2. With later runs that used the single channel technique, the data appear as they do in figure (5-12).

For any given data curve of wave number or damping coefficient versus frequency, there are two hundred odd PSD signal measurements which must be taken. This corresponds roughly to 65 or 70 frequencies, with three measurements taken at each frequency for repeatability. These data are analyzed by a series of Matlab programs as described in appendix A.1. The first set of programs extracts an average magnitude and phase from each of these data sets for each of the PSD locations. The second set of programs collates the magnitude and phase versus frequency data and calculates wave numbers and damping coefficients.

Obtaining wave number and spatial damping coefficient data

The wave number, k_R, is obtained from the phase difference between the two PSD signals,

$$k_R = \frac{(\phi_2 - \phi_1)}{(x_2 - x_1)} - \frac{(n-m)}{(x_2 - x_1)} \tag{5.3}$$

where the phases, ϕ, at each PSD location, x, are

$$\begin{aligned} \phi_1 &= k_R x_1 + n2\pi \\ \phi_2 &= k_R x_2 + m2\pi. \end{aligned} \tag{5.4}$$

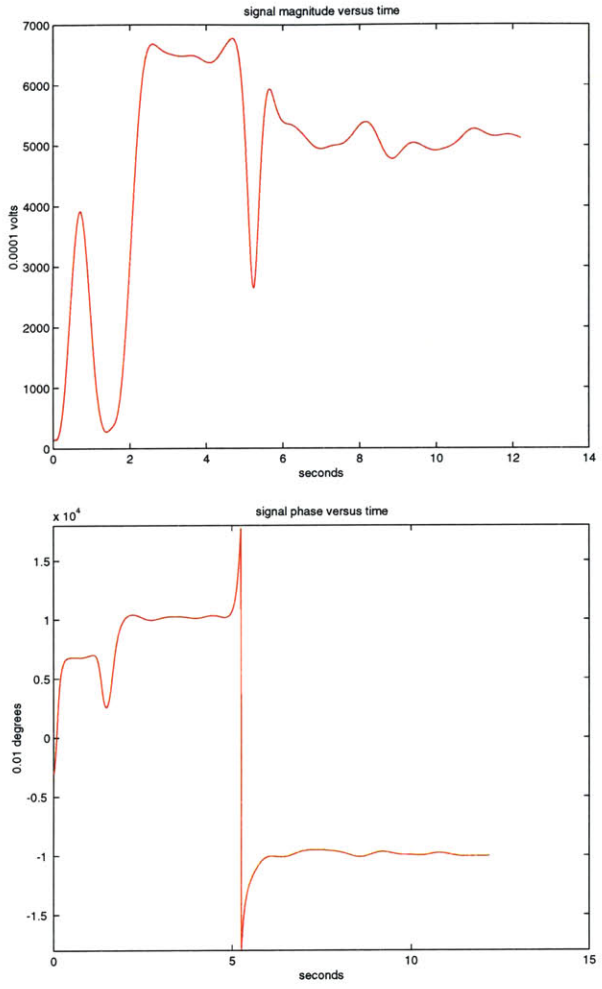

Figure 5-11: Sampled signals, magnitude and phase versus time, for myristic and palmitic acid data sets

where m and n are the winding numbers corresponding to the number of cycles the waves have passed through travelling from the wave maker to the sensor location. These values must be estimated if the first sensor lies more than one wavelength away from the wave maker. This is done by assuming an unbroken phase curve with increasing frequency. This will, indeed, be the case unless the mode of energy

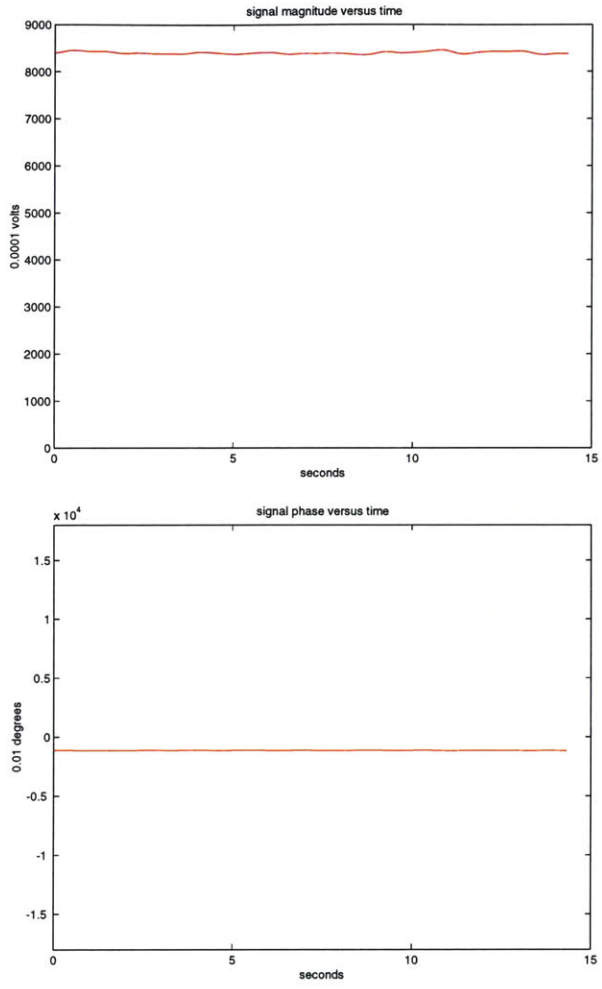

Figure 5-12: Sampled signals, magnitude and phase versus time, for Hercolube C data sets.

transport changes from one wave mode to another. This would be equivalent to the case of a branch cut being passed in the dispersion relation solution space. When this happens, the two modes will separate and a factor of π must be added or subtracted from the expressions in equations 5.4.

The spatial damping coefficient, k_I, is obtained from the amplitude variation

between the two PSD signals,

$$-k_I = \frac{\ln A_2/A_1}{(x_2 - x_1)} \tag{5.5}$$

where the amplitudes, A at each PSD location are

$$A_1 = A_o e^{-k_I x_1} \tag{5.6}$$

$$A_2 = A_o e^{-k_I x_2} \tag{5.7}$$

where A_o represents the capillary wave amplitude at the wave maker.

The wave number and spatial damping coefficient are calculated for each frequency's magnitude and phase data and all of these values are collected into the single data curves of sections 5.5.1, 5.5.2 and 5.5.3.

5.3.4 Calculating group velocity from wavenumber measurements

Group velocity, C_g is defined as

$$C_g = \frac{\partial \omega}{\partial k} \tag{5.8}$$

When the frequency spacing of the data is fine compared with the scale of the effect of resonance on the group velocity, the group velocity can be adequately calculated numerically between either adjacent points

$$C_g(n) = \frac{\omega(n+1) - \omega(n)}{k(n+1) - k(n)}, \tag{5.9}$$

or, between sets of three points

$$C_g(n) = \frac{\omega(n+1) - \omega(n-1)}{k(n+1) - k(n-1)}. \tag{5.10}$$

When the frequency spacing is not very small with respect to the scale of resonance

effects, it is necessary to first fit a polynomial through the wave number data

$$k_R = a_1\omega^{\alpha} + a_2\omega^{\alpha-1} \ldots a_{\beta-1}k_R + a_\beta \tag{5.11}$$

and then to differentiate this polynomial to obtain an estimate of the group velocity. This method gives a somewhat limited accuracy for demonstrating resonance effects associated with the group velocity as the order of the polynomial will affect the curvature of the wave number estimate and will thus affect the appearance of the dips in group velocity curve associated with resonance.

5.3.5 Surface tension measurements

As described in section 5.2.1 platinum Wilhelmy plate is brought into contact with the fluid surface. Surface tension is calculated from the maximum force required to detach the blade.

$$\sigma_o = \frac{gm}{2L} \tag{5.12}$$

where σ_o is surface tension, g, gravity, m, the mass measured by the balance and L the length of the plate.

5.3.6 Calculating static elasticity from in-situ Wilhelmy-Blodgett trough measurements

Elasticity is defined as

$$\epsilon = \frac{\mathrm{d}\sigma_o}{\mathrm{d}\ln A}. \tag{5.13}$$

The Wilhelmy-Blodgett trough measurements give us surface tension, σ_o, in an ever decreasing trough area, A. There are only a few measurements and the scatter

of the data requires that we fit a polynomial through the data

$$\sigma_o = a_1 A^{\alpha} + a_2 A^{\alpha-1} \ldots a_{\beta-1} A + a_{\beta} \tag{5.14}$$

and differentiate this polynomial to obtain an estimate of the static elastic modulus.

5.4 Data quality and modulation of measured signal due to the dilational wave mode

5.4.1 Data modulation

Because each of two wave mode, capillary and dilational has a transverse component, measurements of transverse waves will show capillary wave characteristics modulated by the dilational wave mode. This can be readily seen in the wave slope, damping coefficient and wave number spectra as seen in figures (5-13) and (5-14), respectively.

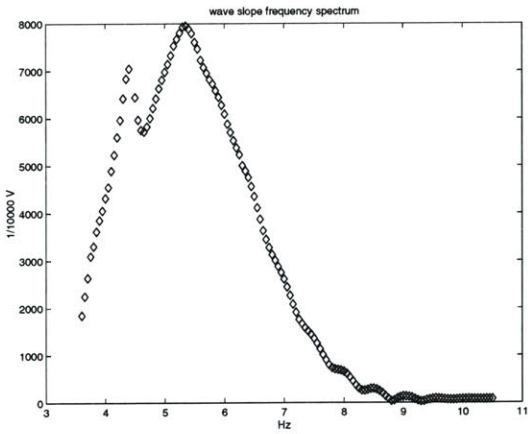

Figure 5-13: Wave slope spectrum, signal magnitude versus frequency, with modulations apparent at the higher frequencies. This figure was constructed from data taken at a single location for 3.5 – 10.5 hertz waves.

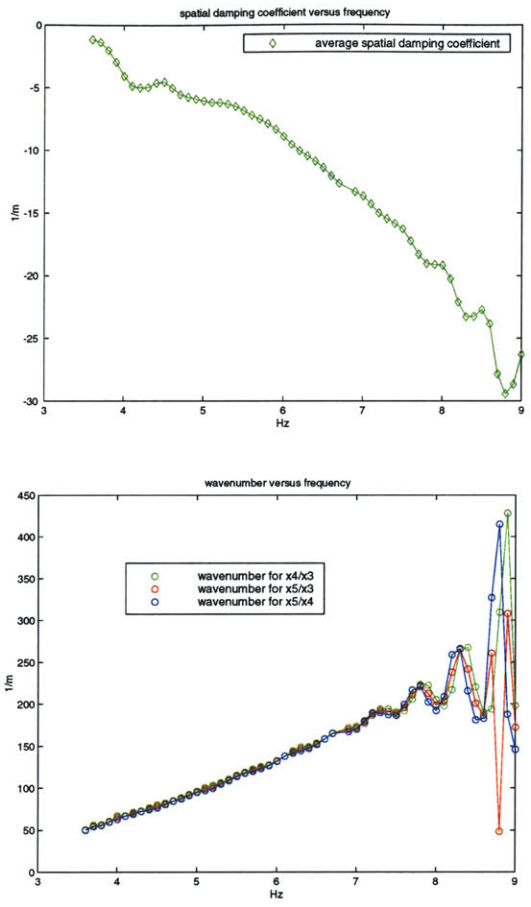

Figure 5-14: Damping coefficient, k_I, and wave number, k_R, versus frequency, $f = \omega/2\pi$, data with modulations apparent at the higher frequencies. These figures were constructed from data taken at three locations for 3.5–10.5 hertz waves.

The spacing of the oscillations is dependent on the placement of the sensors. This phenomenon can be elucidated by the following calculations.

Both the capillary and the dilational wave modes have transverse and dilational components. A wavemaker oscillating at a single frequency will produce both wave modes. The combined surface displacement, η, can be most easily represented as,

$$\eta = Ae^{-\alpha x}e^{i(k_A x+\omega t)} + Be^{-\beta x}e^{i(k_B x+\omega t)}$$

$$= \left[Ae^{-\alpha x}e^{i(k_A x)} + Be^{-\beta x}e^{i(k_B x)}\right] e^{i\omega t} \tag{5.15}$$

where A and B are the amplitudes, α and β are the spatial damping coefficients, and k_A and k_B are the wave numbers of the two wave modes. Let the A wave correspond to the capillary mode and the B wave correspond to the dilational wave mode.

If we take the fast fourier transform (FFT) of this wave, we can extract the magnitude, $|M|$, and phase, ϕ, of the bracketed expression in equation 5.15.

Letting

$$\tilde{A} = Ae^{-\alpha x} \tag{5.16}$$

$$\tilde{B} = Be^{-\beta x} \tag{5.17}$$

the magnitude squared has the form

$$\begin{aligned} |M|^2 &= \left[\tilde{A}\cos(k_A x) + \tilde{B}\cos(k_B x)\right]^2 + \left[\tilde{A}\sin(k_A x) + \tilde{B}\sin(k_B x)\right]^2 \\ &= \tilde{A}^2 + \tilde{B}^2 + 2\tilde{A}\tilde{B}\cos(k_A x)\cos(k_B x) + 2\tilde{A}\tilde{B}\sin(k_A x)\sin(k_B x) \\ &= \tilde{A}^2 + \tilde{B}^2 + 2\tilde{A}\tilde{B}\cos(k_A - k_B)x. \end{aligned} \tag{5.18}$$

Defining $\epsilon = \tilde{B}/\tilde{A}$, this expression simplifies to

$$|M|^2 = \tilde{A}^2\left[1 + \epsilon^2 + 2\epsilon\cos(k_A - k_B)x\right]. \tag{5.19}$$

At the lowest oder of ϵ the magnitude becomes,

$$|M| = \tilde{A}\left[1 + \epsilon\cos(k_A - k_B)x\right] \tag{5.20}$$

and we see that the apparent magnitude of the signal is the magnitude of the primary wave form plus a sinusoidal modulation whose "frequency" is the location of the sensor. It is the wave number that varies, not the sensor location. Thus the sensor location is in a sense the frequency of the sinusoid. The further from the wave maker the sensor is, the higher the "frequency" of modulation. Thus the modulation has a

sort of Doppler effect. This modulation is apparent in figure (5-13).

To find the spatial damping coefficient of the waves we need magnitude information at two locations, x_1 and x_2:

$$|M_1| = Ce^{-\delta x_1} = \tilde{C}(x_1) \tag{5.21}$$

$$|M_2| = Ce^{-\delta x_2} = \tilde{C}(x_2) \tag{5.22}$$

where C and δ are some general expressions for amplitude and damping.

The damping coefficient is then calculated as

$$-\delta = \frac{\ln|M_2| - \ln|M_1|}{x_2 - x_1} \tag{5.23}$$

With the two waves present, the calculation of a damping coefficient is slightly more complicated. The squared wave magnitudes at the two locations are composites of both wave modes are

$$|M_1|^2 = \tilde{A}^2(x_1)\left[1 + \epsilon_1^2 + 2\epsilon_1 \cos(k_A - k_B)x_1\right] \tag{5.24}$$

$$|M_2|^2 = \tilde{A}^2(x_2)\left[1 + \epsilon_2^2 + 2\epsilon_2 \cos(k_A - k_B)x_2\right] \tag{5.25}$$

Noting that

$$\ln|M|^2 = 2\ln|M| \tag{5.26}$$

and

$$\ln|M_2| - \ln|M_1| = \ln\frac{|M_2|}{|M_1|} \tag{5.27}$$

then

$$\ln|M_2|^2 - \ln|M_1|^2 = 2\ln\frac{|M_2|}{|M_1|} = 2\left[\ln|M_2| - \ln|M_1|\right] \tag{5.28}$$

so that the apparent damping coefficient, let's call it $-\gamma$, is:

$$-\gamma = \frac{\frac{1}{2}\left[\ln|M_2|^2 - \ln|M_1|^2\right]}{x_2 - x_1} \tag{5.29}$$

$$= \frac{(|M_2|^2/|M_1|^2)}{2(x_2 - x_1)} \tag{5.30}$$

$$= \frac{1}{2(x_2 - x_1)} \ln\left\{\frac{\tilde{A}^2(x_2)}{\tilde{A}^2(x_1)} \frac{[1 + \epsilon^2(x_2) + 2\epsilon(x_2)\cos(k_A - k_B)x_1]}{[1 + \epsilon^2(x_1) + 2\epsilon(x_1)\cos(k_A - k_B)x_1]}\right\} \tag{5.31}$$

$$= \frac{1}{2(x_2 - x_1)} \ln\left\{\frac{\tilde{A}^2(x_2)}{\tilde{A}^2(x_1)}\right\} + \frac{1}{2(x_2 - x_1)} \ln\left\{\frac{[1 + \epsilon^2(x_2) + 2\epsilon(x_2)\cos(k_A - k_B)x_1]}{[1 + \epsilon^2(x_1) + 2\epsilon(x_1)\cos(k_A - k_B)x_1]}\right\} \tag{5.32}$$

Since

$$\frac{\tilde{A}^2(x_2)}{\tilde{A}^2(x_1)} = \frac{A^2 e^{-2\alpha x_2}}{A^2 e^{-2\alpha x_1}} = e^{-2\alpha(x_2 - x_1)} \tag{5.33}$$

$$\epsilon = \frac{\tilde{B}}{\tilde{A}} = \frac{Be^{-\beta x}}{Ae^{-\alpha x}} = \frac{B}{A} e^{-(\beta - \alpha)x} \tag{5.34}$$

equation 5.32 becomes

$$-\gamma = \frac{1}{2(x_2 - x_1)} \left\{-2\alpha(x_2 - x_1) + \ln \frac{[1 + \epsilon^2(x_2) + 2\epsilon(x_2)\cos(k_A - k_B)x_1]}{[1 + \epsilon^2(x_1) + 2\epsilon(x_1)\cos(k_A - k_B)x_1]}\right\} \tag{5.35}$$

$$= -\alpha + \frac{1}{2(x_2 - x_1)} \ln\left\{\frac{\tilde{A}^2(x_2)}{\tilde{A}^2(x_1)}\right\} + \frac{1}{2(x_2 - x_1)} \ln\left\{\frac{[1 + \epsilon^2(x_2) + 2\epsilon(x_2)\cos(k_A - k_B)x_1]}{[1 + \epsilon^2(x_1) + 2\epsilon(x_1)\cos(k_A - k_B)x_1]}\right\} \tag{5.36}$$

$$= -\alpha + E \tag{5.37}$$

and we find that the apparent damping coefficient comprised the damping coefficient of the capillary mode plus an error function that modulates this value.

The error function can be simplified when the relative amplitude of the transverse component of the dilational wave is small in comparison with the capillary wave so that $\epsilon << 1$. Then

$$
\begin{aligned}
-\gamma \approx -\alpha \quad &+ \quad 2\epsilon_2 \cos(k_A - k_B)x_2 - 2\epsilon_1 \cos(k_A - k_B)x_1 \\
&+ \quad \epsilon_2^2 - \epsilon_1^2 + 4\epsilon_2^2 \cos^2(k_A - k_B)x_2 \\
&- \quad 4\epsilon_1^2 \cos^2(k_A - k_B)x_1
\end{aligned} \tag{5.38}
$$

Neglecting second order effects

$$
\begin{aligned}
-\gamma &\approx -\alpha + 2\epsilon_2 \cos(k_A - k_B)x_2 - 2\epsilon_1 \cos(k_A - k_B)x_1 \\
&= -\alpha + 2\epsilon_2 \cos\left[(k_A - k_B)x_1 + (k_A - k_B)(x_2 - x_1)\right] - 2\epsilon_1 \cos\left[(k_A - k_B)x_1\right] \\
&= -\alpha + 2\epsilon_2 \cos\left[(k_A - k_B)x_1 + \psi\right] - 2\epsilon_1 \cos\left[(k_A - k_B)x_1\right]
\end{aligned} \tag{5.39}
$$

where

$$
\psi = (k_A - k_B)(x_2 - x_1). \tag{5.40}
$$

So, we can see that for a small tranverse contribution of the secondary wave form,, the spatial damping coefficient for the double wave form is the damping coefficient for the primary wave plus a sinusoidal modulation with a "frequency" equal to the location of the first sensor. A sensor at twice the distance of another would have a frequency of modulation twice as large and, in fact, we see exactly this effect in our measurements as seen in figure 5-15. In this figure, the top graph shows the absolute value of an average damping coefficient versus frequency calculated from data taken at three locations 16, 17 and 18 centimeters from the wave maker, respectively. The bottom graph shows the absolute value of an average damping coefficient versus frequency calculated from data taken at three locations 26, 27 and 88 centimeters from the wave maker, respectively. Note that the ratio of the periods of the oscillation of .5/.75 is roughly the inverse of the ratios of the distances of the sensors from the wave maker 17/27. This is exactly what we would expect from our calculations.

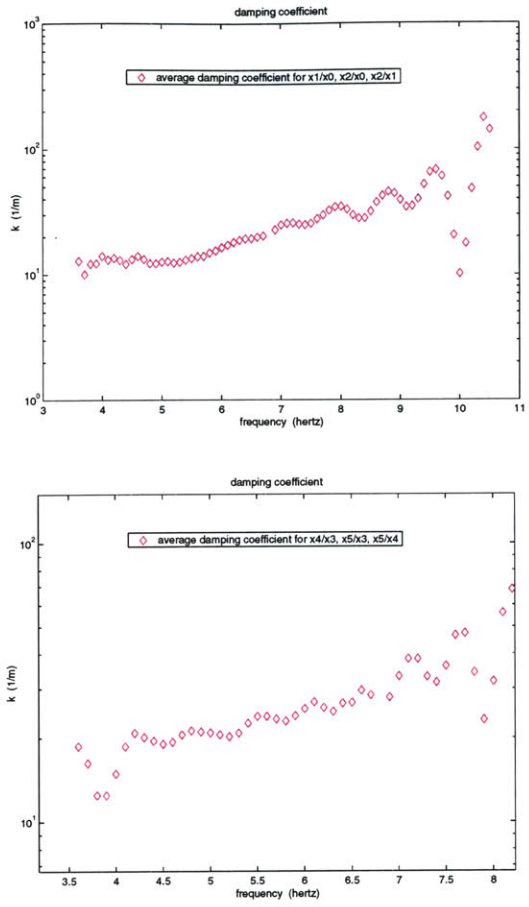

Figure 5-15: The top graph shows an average of the absolute value of the damping coefficient, $|k_I|$, versus frequency, f, calculated from data taken at three locations 16, 17 and 18 centimeters from the wave maker, respectively. The bottom graph shows an average of the absolute value of the damping coefficient, $|k_I|$, versus frequency, f, calculated from data taken at three locations 26, 27 and 28 centimeters from the wave maker, respectively. The inverse ratio of the periods of oscillation corresponds to ratio of the distance of the sensor locations from the wave maker.

To see the modulation of the wave number calculated from measurements, we begin with a calculation of the tangent of the phase of equation 5.15 which has the form

$$\tan\phi \quad = \quad \left[\frac{\tilde{A}\sin k_A x + \tilde{B}\sin k_B x}{\tilde{A}\cos k_A x + \tilde{B}\cos k_B x}\right]$$

$$
\begin{aligned}
&= \left[\frac{\sin k_A x + \epsilon \sin k_B x}{\cos k_A x + \epsilon \cos k_B x}\right] \\
&= \frac{\sin k_A x}{\cos k_A x}\left[\frac{1+\epsilon\frac{\sin k_B x}{\sin k_A x}}{1+\epsilon\frac{\cos k_B x}{\cos k_A x}}\right] \\
&= \tan k_A x E_\phi
\end{aligned} \tag{5.41}
$$

which we see comprise the tangent of the phase of the primary wave modulated by the presence of the secondary wave form. To the first order in ϵ the error function can be represented as

$$
E \approx 1 + \epsilon\left(\frac{\sin k_B x}{\sin k_A x} - \frac{\cos k_B x}{\cos k_A x}\right). \tag{5.42}
$$

The apparent wave number is calculated from

$$
k = \frac{\phi(x_2) - \phi(x_1)}{x_2 - x_1} \tag{5.43}
$$

When the error function is small,

$$
\arctan(E\tan k_A x) \approx E k_A x \tag{5.44}
$$

so we can represent the apparent wave number as

$$
\begin{aligned}
k &\approx \frac{E_2 k_A x_2 - E_1 k_A x_1}{x_2 - x_1} \\
&= \frac{k_A}{x_2 - x_1}\left(E_2 x_2 - E_1 x_1\right) \\
&= \frac{k_A}{x_2 - x_1}\left\{\left[1 + \epsilon_2\left(\frac{\sin k_B x_2}{\sin k_A x_2} - \frac{\cos k_B x_2}{\cos k_A x_2}\right)\right] x_2\right. \\
&\quad \left. - \left[1 + \epsilon_1\left(\frac{\sin k_B x_1}{\sin k_A x_1} - \frac{\cos k_B x_1}{\cos k_A x_1}\right)\right] x_1\right\} \\
&= k_A\left\{1 + \epsilon_2\frac{x_2}{x_2 - x_1}\left(\frac{\sin k_B x_2}{\sin k_A x_2} - \frac{\cos k_B x_2}{\cos k_A x_2}\right)\right. \\
&\quad \left. - \epsilon_1\frac{x_1}{x_2 - x_1}\left(\frac{\sin k_B x_1}{\sin k_A x_1} - \frac{\cos k_B x_1}{\cos k_A x_1}\right)\right\}
\end{aligned} \tag{5.45}
$$

and we see that the apparent wave number, k, is a combination of the primary

wave number, k_A, and a sinusoidal function which can be seen in figure (5-14). In this figure, the sensor positions x_1 and x_2 are close together (approximately one centimeter) and the modulations in the wave number are very apparent. When the sensors are much further apart (approximately ten centimeters), the modulations are greatly ameliorated as seen in figure (5-16).

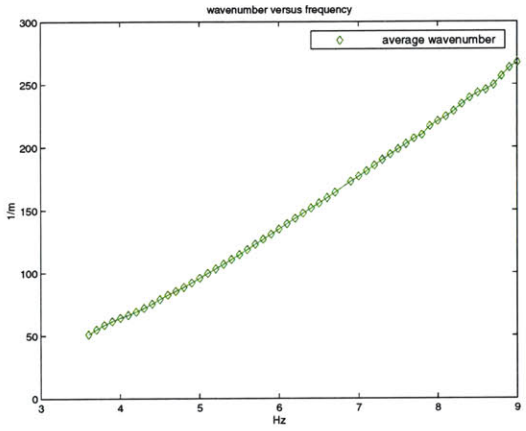

Figure 5-16: Average wave number, k_R, versus frequency, f, calculated from data taken at three locations, each ten centimeters apart.

5.4.2 Data quality

Oscillations pose a difficulty for application of the inverse method to surfactant wave data as will be discussed in chapter 6. However, despite these oscillations, the overall quality of the experimental data is quite good.

To test this quality, measurements of water waves were taken and the damping coefficient calculated from these data compared to theory and other published experimental data. As can be seen figure (5-17), our data is significantly closer to theory than other published data.

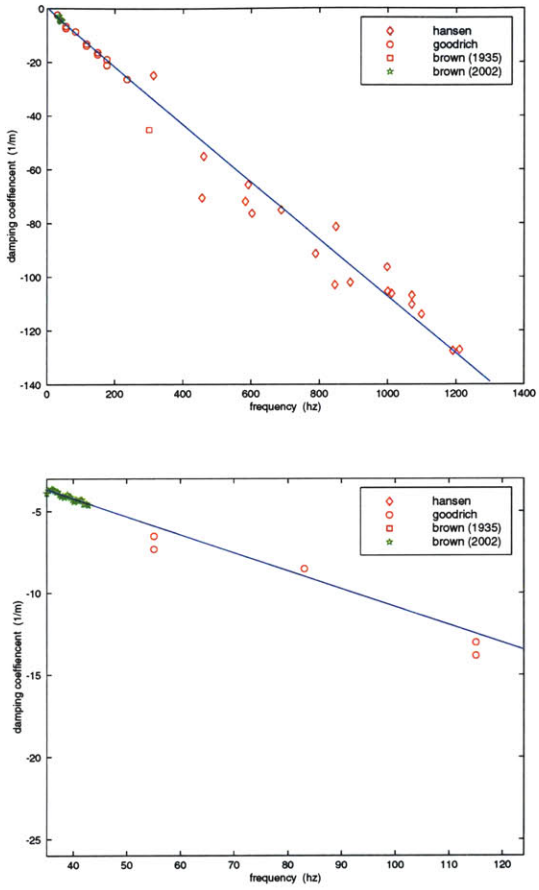

Figure 5-17: My measurements of damping coefficient, k_I, versus frequency, f for water compared to other published experimental data. My measurements are marked in green and all other authors' measurements in red. The blue line represents the analytically predicted spatial damping coefficient of pure water.

5.5 Experimental measurements

Having now described in some detail the experimental set up and data processing techniques, we present the data taken in our laboratory.

Early experiments were done with myristic and palmitic acids surfactant monolayers on a dilute aqueous solution of hydrochloric acid. The bulk fluid was made to be

a dilute aqueous solution of 0.01 N HCl in distilled water. The surfactants films were made of myristic and palmitic acids in hexane solutions. The hexanes allowed the the surfactant solutions to spread across the surface before evaporating and leaving only the myristic and palmitic acid films. The surfactant solutions were deposited on the surface with a micro-liter syringe.

Waves were produced in the 2.5 – 10 hertz range in our tank and data sets comprising time records of the wave slope at two locations, 10 centimeters apart, were taken with the position sensing diodes, PSDs, and the two lasers as described in section 5.2.1. These data sets were processed as described in section 5.3.2 to obtain magnitude, phase, spatial damping coefficient and wave number data versus frequency.

With early measurements, we had trouble obtaining good quality damping coefficient data. Thus the wave data presented for palmitic and myristic acid monolayers on aqueous solutions is comprised solely of plots of wave number versus frequency.

The wave number data were extremely precise with variation of data from repeated measurements generally much less than 1 %. Each wave number data curve presented in this section comes from three measurements taken at each frequency. As the data have so little variation, the symbols for the data from each measurement at a single frequency lie virtually on top of each other. Thus the data is presented without error bars - the error is generally smaller than the size of the symbols. A red line is drawn through the average wave number values for visual clarity.

Wilhelmy-Blodgett trough measurements as described in section 5.2.1 were also made for each surfactant.

5.5.1 Palmitic acid monolayers

The palmitic acid solution became a scaly shiny film on the surface. The film appeared to be made of connected individual patches. This may be the reason why the Wilhelmy-Blogett trough measurements were so discontinuous at different surfactant concentrations.

Wave measurements were taken for six different film densities (concentrations) of

palmitic acid monolayers, 52, 39, 31, 26 and 19 angstroms per molecule.

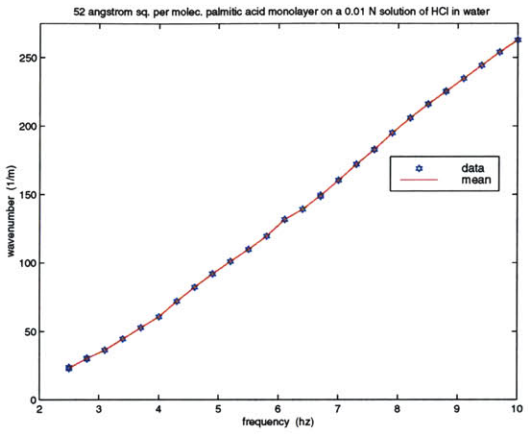

Figure 5-18: Wave number, k_R, versus frequency, f, measurements for waves traveling on a 0.01 N HCl aqueous solution with a palmitic acid film of concentration 52 square angstroms per molecule at a temperature of 21.2 °C. The red symbols denote values of wave number determined from individual measurements. The blue line gives the average values of wave number for all measurements.

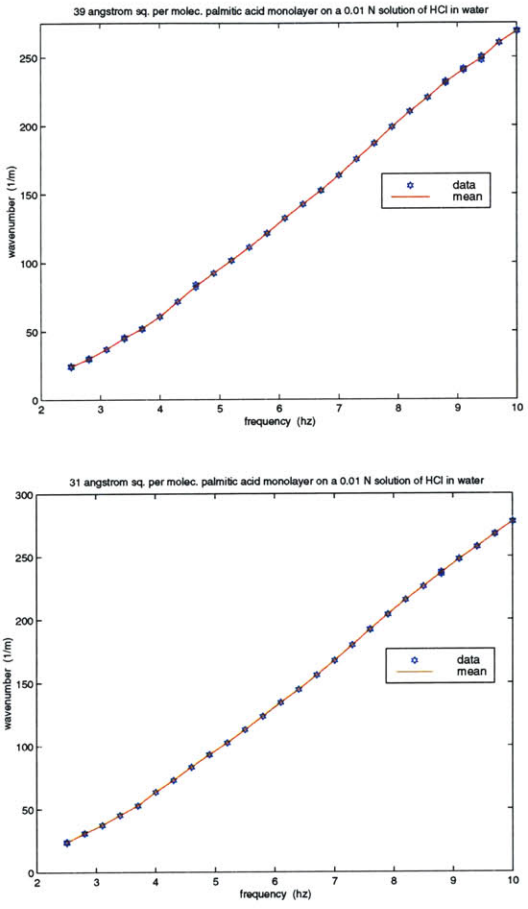

Figure 5-19: Wave, k_R, versus frequency, f, measurements for waves traveling on a 0.01 N HCl aqueous solution with a palmitic acid film of concentrations 39 and 31 square angstroms per molecule, respectively, at a temperature of 21.2 °C. The red symbols denote values of wave number determined from individual measurements. The blue line gives the average values of wave number for all measurements.

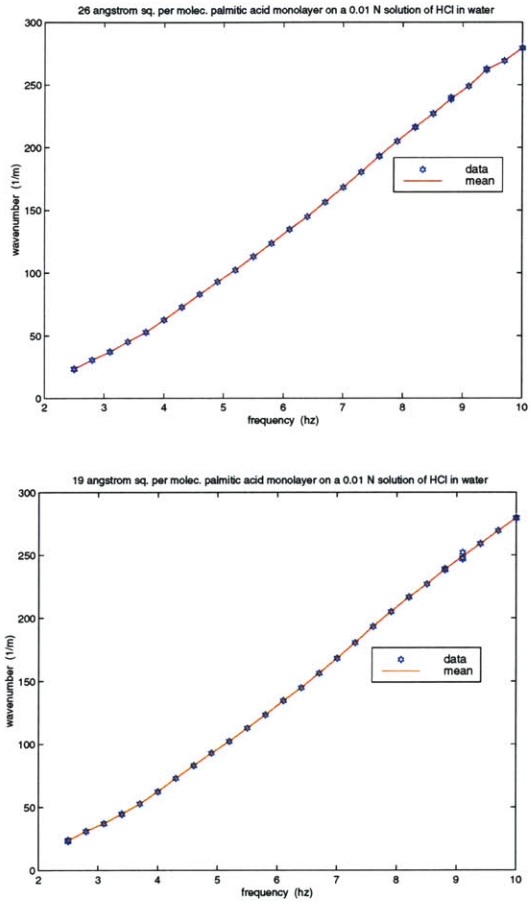

Figure 5-20: Wave, k_R, versus frequency, f, measurements for waves traveling on a 0.01 N HCl aqueous solution with a palmitic acid film of concentrations 26 and 19 square angstroms per molecule, respectively, at a temperature of 21.2 °C. The red symbols denote values of wave number determined from individual measurements. The blue line gives the average values of wave number for all measurements.

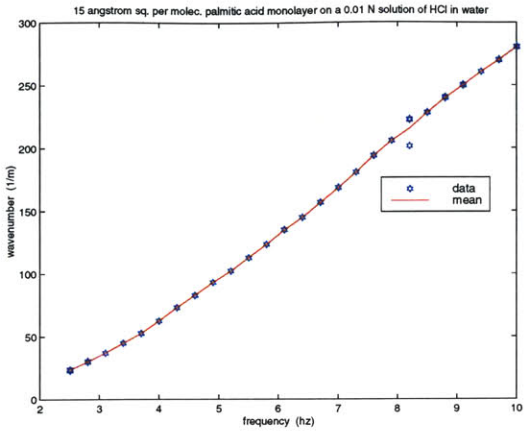

Figure 5-21: Wave, k_R, versus frequency, f, measurements for waves traveling on a 0.01 N HCl aqueous solution with a palmitic acid film of concentration 15 square angstroms per molecule at a temperature of 21.2 °C. The red symbols denote values of wave number determined from individual measurements. The blue line gives the average values of wave number for all measurements.

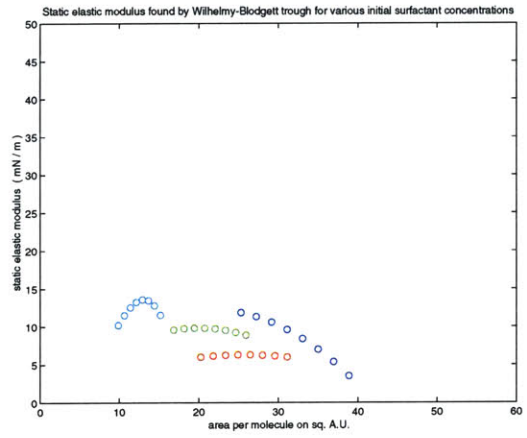

Figure 5-22: Static elastic dilational modulus estimated from measurements of surface tension versus surfactant concentration of palmitic acid monolayers on a 0.01 N HCl aqueous solution made with an *in-situ* Wilhelmy-Blodgett trough at a temperature of 21.2 °C.

5.5.2 Myristic acid monolayers

These monolayers spread very easily and evenly over the surface. The Wilhelmy-Blodgett measurement was made with a single initial surfactant film concentration and thus appears continuous with respect to film concentration.

Wave measurements were taken for three different film densities (concentrations) of palmitic acid monolayers, 36, 29 and 21 angstroms per molecule.

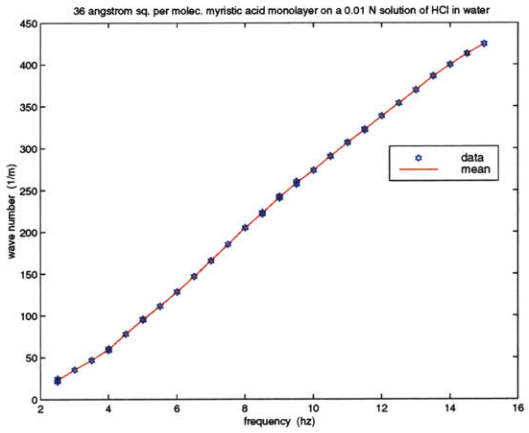

Figure 5-23: Wave measurements for waves traveling on a 0.01 N HCl aqueous solution with a myristic acid film of concentration 36 square angstroms per molecule at a temperature of 21°C. The red symbols denote values of wave number determined from individual measurements. The blue line gives the average values of wave number for all measurements.

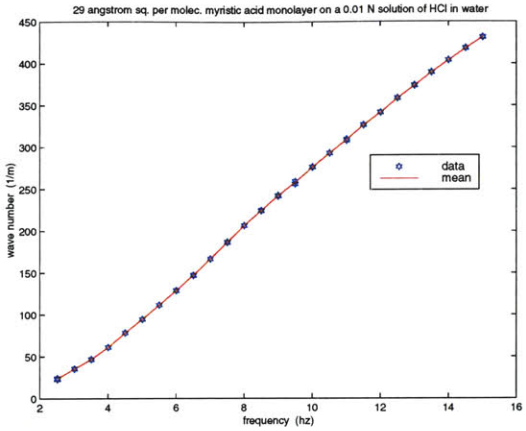

Figure 5-24: Wave measurements for waves traveling on a 0.01 N HCl aqueous solution with a myristic acid film of concentration 29 square angstroms per molecule at a temperature of 21°C. The red symbols denote values of wave number determined from individual measurements. The blue line gives the average values of wave number for all measurements.

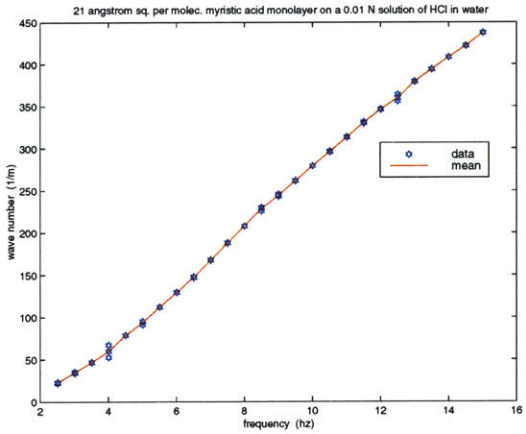

Figure 5-25: Wave measurements for waves traveling on a 0.01 N HCl aqueous solution with a myristic acid film of concentrations 21 square angstroms per molecule at a temperature of 21°C. The red symbols denote values of wave number determined from individual measurements. The blue line gives the average values of wave number for all measurements.

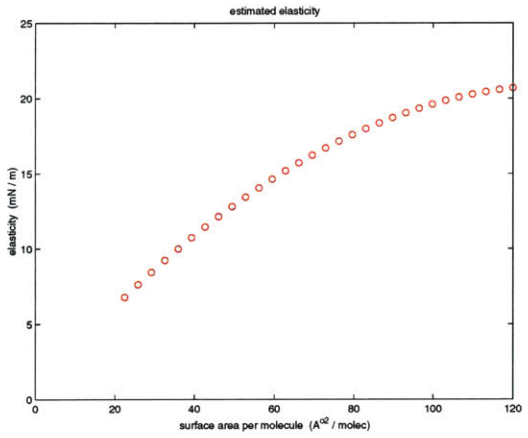

Figure 5-26: Static elastic dilational modulus estimated from measurements surface tension versus surfctant concentrations of myristic acid monolayers on a 0.01 N HCl aqueous solution made with an *in-situ* Wilhelmy-Blodgett trough at a temperature of 21°C.

5.5.3 Hercolube C measurements

One of the only published data sets showing the effect of resonance on the capillary wave damping coefficient was taken from wave experiments on Hercolube C (Bock 1991). The effects of modulation in this data set do not appear to be significant. Unfortunately, Bock did not publish accompanying wave number data. As will be discussed in chapter (6), this would be very useful for the application of the inverse method. To get good quality spatial damping coefficient and wave number data sets simultaneously, we decided to obtain our own sample of Hercolube C.

Hercolube C is a pentaerythritol ester made by the Hercules Chemical Company which is used as a lubricant for jet aircraft engines. It is not a surfactant. It is the bulk fluid in the flume and its interface with air is visco-elastic. We model this interface in the same way as we would one with a surfactant - as a monomolecular depth interface.

Waves were produced in the 2.5 – 10 hertz range in our tank and data sets comprising time records of the wave slope were taken at six locations for three different decibel settings of the wavemaker. Three of the six locations were upstream, each 0.5 centimeters apart: x_0, x_1, x_2, where $x_1 = x_0 + .5$ cm, $x_2 = x_1 + .5$ cm $= x_0 + 1.0$ cm, and three downstream, each 0.5 centimeters apart: x_3, x_4, x_5, where $x_3 = x_0 + 10$ cm, $x_4 = x_3 + .5$ cm, $x_5 = x_4 + .5$ cm $= x_3 + 1.0$ cm. The first downstream location was located 10 centimeters away from the first upstream location.

Like the palmitic and myristic acid data sets, wave number data at a single location were highly repeatable. Variation was of the order of 1%, smaller than the size of the symbols. We were able to improve our measurement technique and thus were also able to obtain good quality spatial damping coefficient as well. The variation of this data was also of the order 1%, smaller than the size of the symbols.

No Wilhelmy-Blodgett data was taken as this method is only applicable to insoluble surfactants.

An initial data set at a single wavemaker decibel setting of -17 and all six locations was taken to establish the amount of variability of the data due to sensor location. The

fluid temperature was 22.5 °C. As can be seen in figure (5-27), there is some variability in the damping data which is exacerbated at the higher end of the frequency spectrum where the effects of modulation are apparent. The dips in the lower end of the frequency measurements will be described in chapter 7, "Experimental measurements of resonance effects". There is less variability in the wave number data, again, the

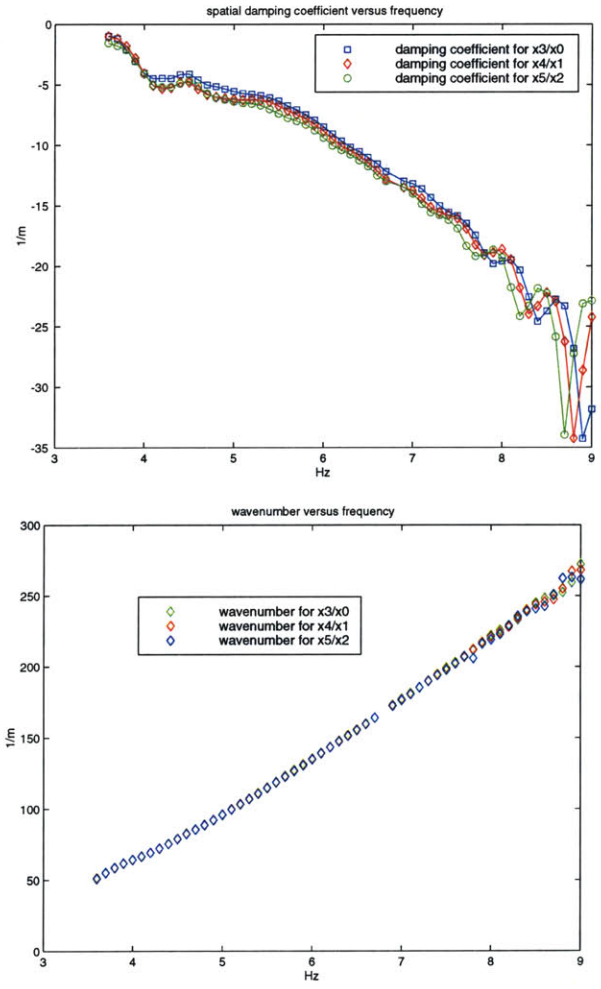

Figure 5-27: The upper graph shows the damping coefficient calculated from experimental data at three different location pairs, x_0/x_3, x_1/x_4 and x_2/x_5, each pair separated by 10 centimeters. The upper graph shows the wave number calculated from experimental data at three different location pairs, x_0/x_3, x_1/x_4 and x_2/x_5, each pair separated by 10 centimeters.

largest variability corresponds to the data at the higher end of the frequency spectrum where modulation is apparent.

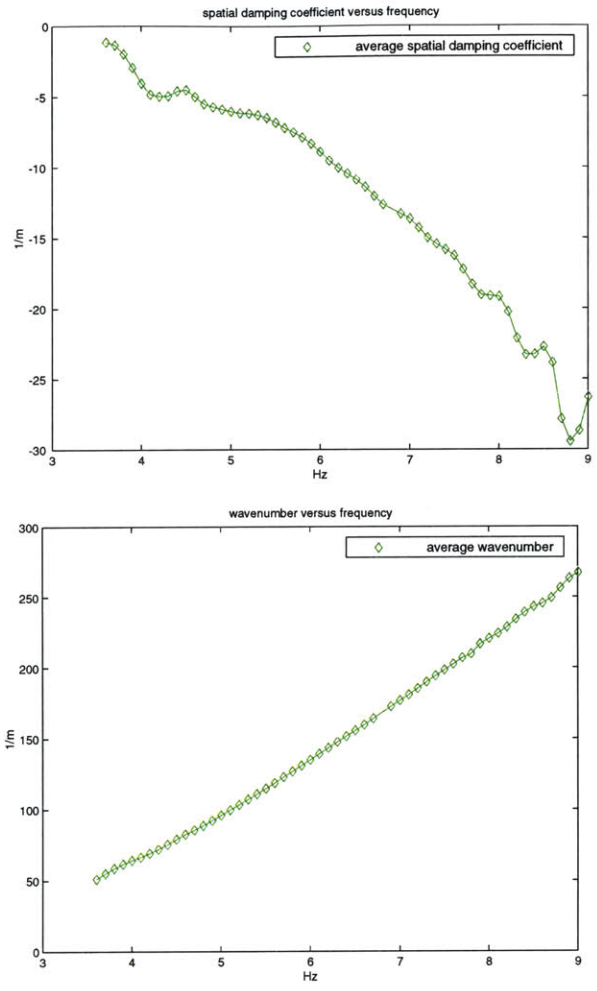

Figure 5-28: The upper graph shows the average damping coefficient calculated from experimental data at three different location pairs, x_0/x_3, x_1/x_4 and x_2/x_5, each pair separated by 10 centimeters. The lower graph shows an average calculated wave number from experimental data at three different location pairs, x_0/x_3, x_1/x_4 and x_2/x_5, each pair separated by 10 centimeters.

The data in figure (5-27) were averaged and the wave number and damping coefficient calculations are shown in figure 5-28. Note that while the effects of modulation are still apparent, they are reduced.

The wave number can also be calculated between the three upstream locations and between the three downstream locations. Figure 5-29 shows these results. Note

that the modulation of the capillary wave signal is very large for these calculations.

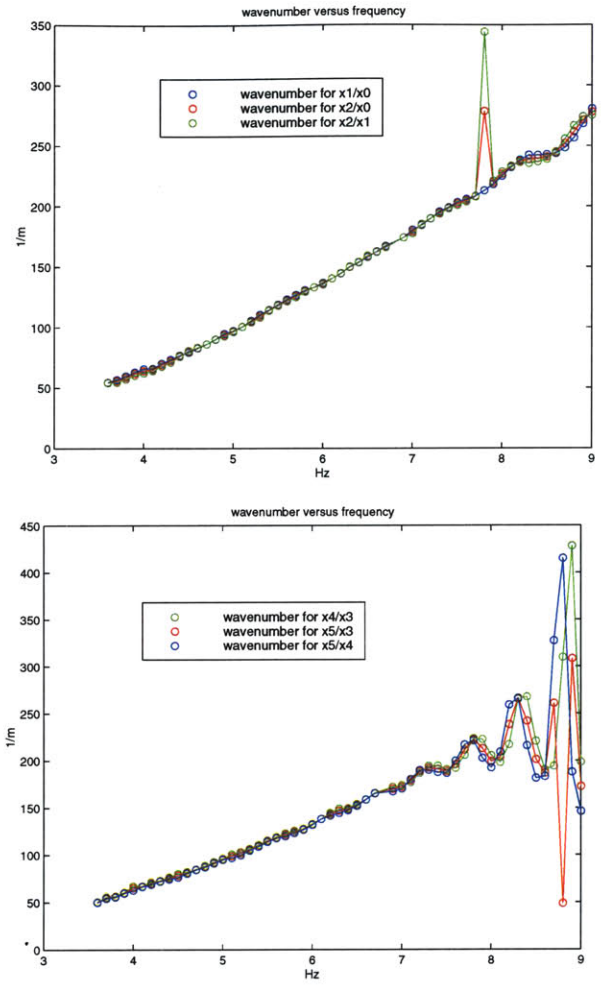

Figure 5-29: The upper graph shows the wave number calculated from experimental data at three different location pairs made of the upstream locations, x_0/x_1, x_0/x_2 and x_1/x_2, separated by 5, 10 and 5 millimeters, respectively. The upper graph shows the wave number calculated from experimental data at three different location pairs made of the downstream locations, x_0/x_1, x_0/x_2 and x_1/x_2, separated by 5, 10 and 5 millimeters, respectively.

The second set of Hercolube C data was taken at wavemaker power levels of -19, -17 and -15 dB. As shown in figure (5-30), the data had no amplitude dependence.

The average of the three amplitude data sets shown in figure (5-30) is shown in figure figure (5-31).

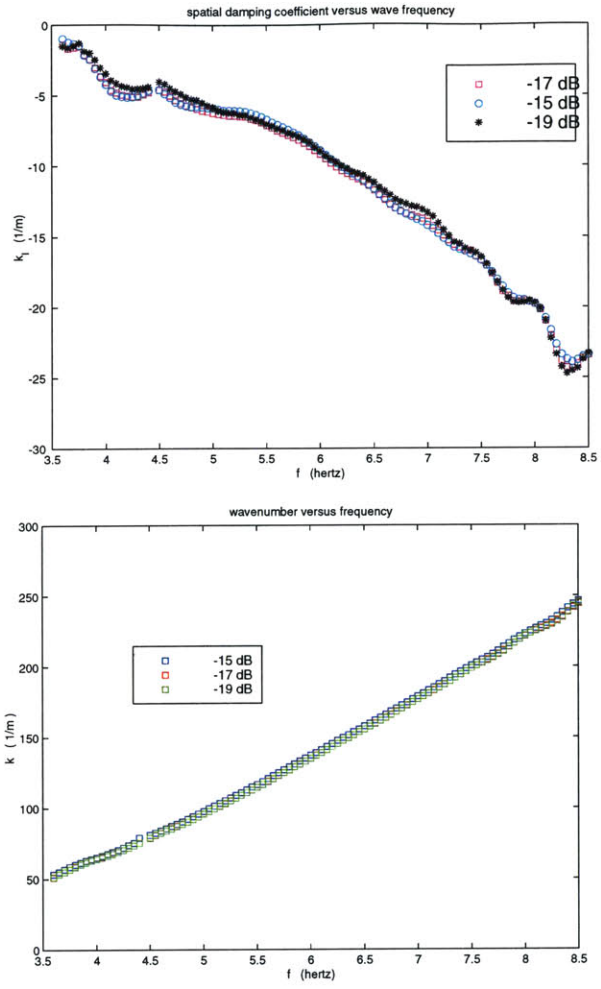

Figure 5-30: The upper graph shows the calculated damping coefficient calculated from experimental data at three different location pairs, each pair separated by 10 centimeters. The lower graph shows the calculated wavenumber from experimental data at three different location pairs.

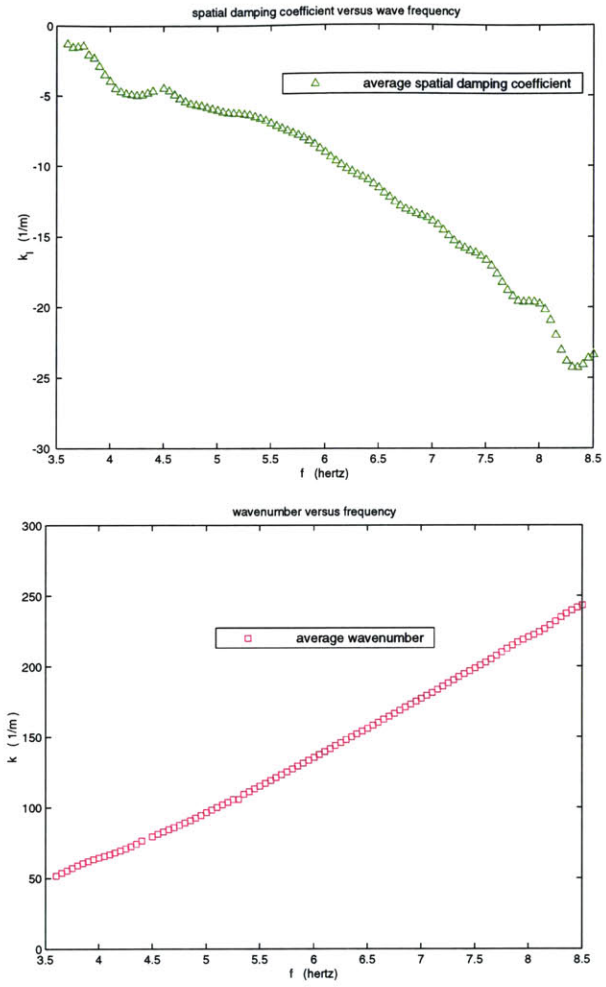

Figure 5-31: The upper graph shows the average calculated damping coefficient calculated from all of the location pairs. The lower graph shows an average calculated wavenumber from all of the location pairs.

Wave slope spectra were produced for each of the six locations.

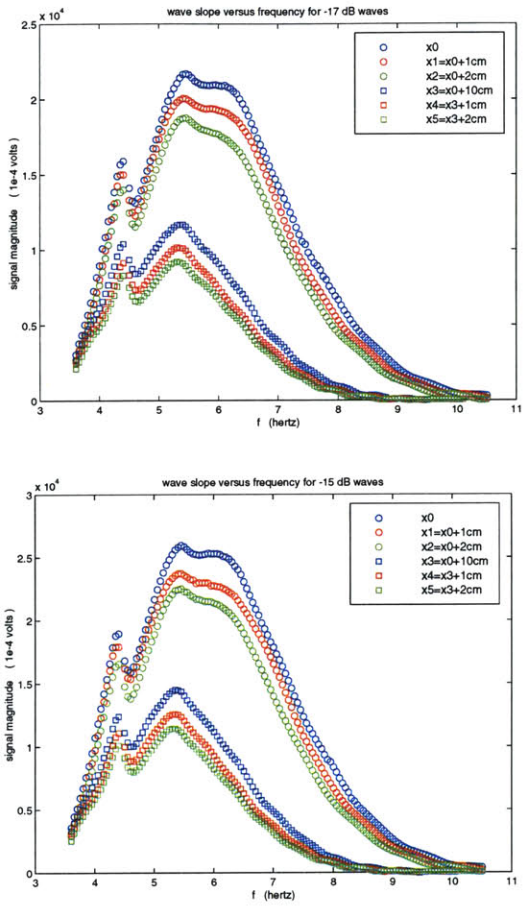

Figure 5-32: Wave slope spectra of Hercolube C at six tank locations. The upper and lower figures were made for wave maker power setting of -15 dB and -17dB, respectively.

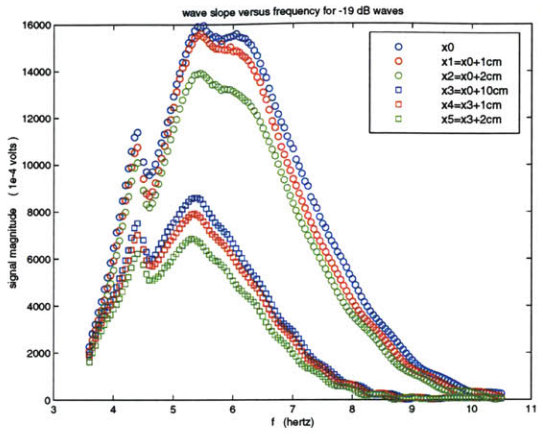

Figure 5-33: Wave slope spectra of Hercolube C at six tank locations. The figure was made for a wave maker power setting of -19dB.

Additional wave slope data was taken at 23, 23.5, 17.5 and 15.5 ° C.

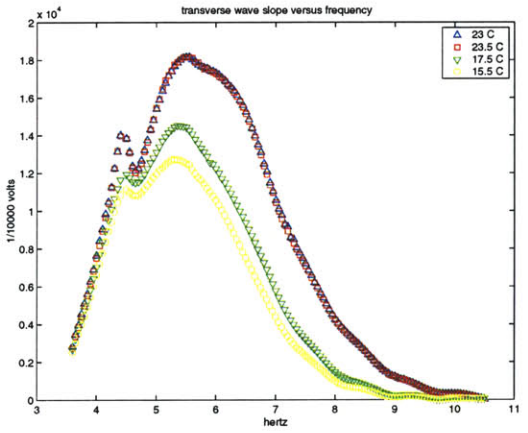

Figure 5-34: Wave slope versus frequency data taken at 23, 23.5, 17.5 and 15.5 ° C.

In addition to the wave data, independent laboratory measurements of surface tension, density and viscosity were made with the equipment described in section 5.2.1.

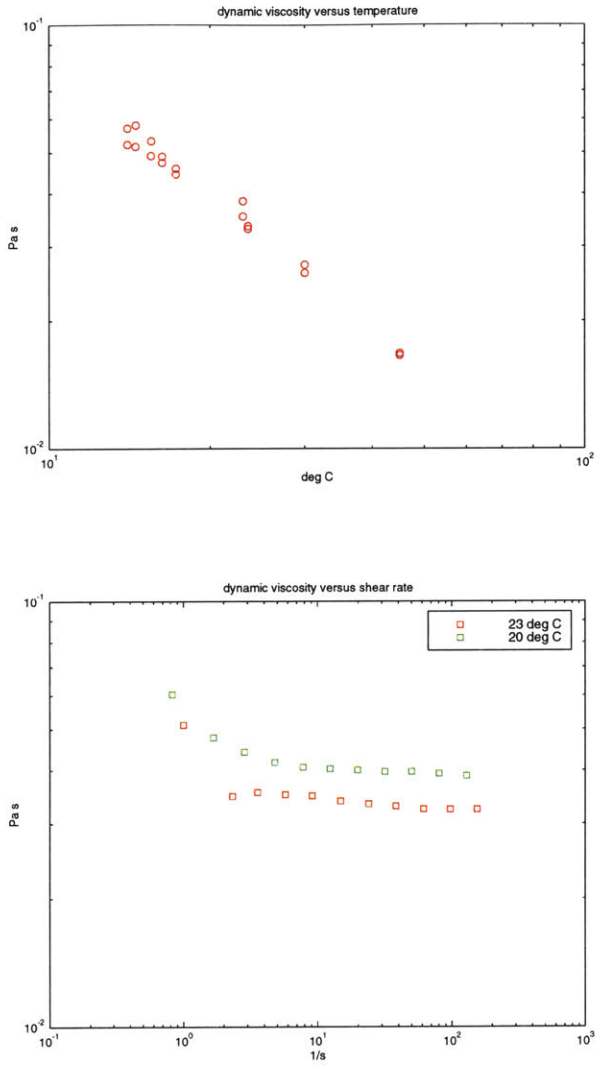

Figure 5-35: Dynamic viscosity versus temperature and dynamic viscosity versus shear rate.

Viscosity measurements showed linearity over most of the shear stress range in figure 5-35 with a small hysteresis at the lower end of the range for fluid at 20 degrees Celsius.

Density and surface tension were linear over the entire temperature range as shown

in figures 5-36 and 5-37. The values obtained for Hercolube C at 23 degrees Celcius

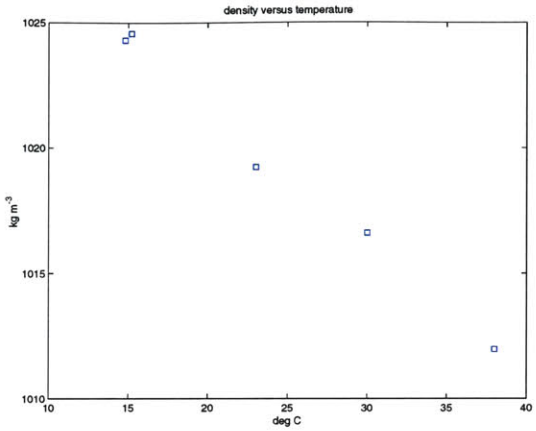

Figure 5-36: Hecolube C density versus temperature.

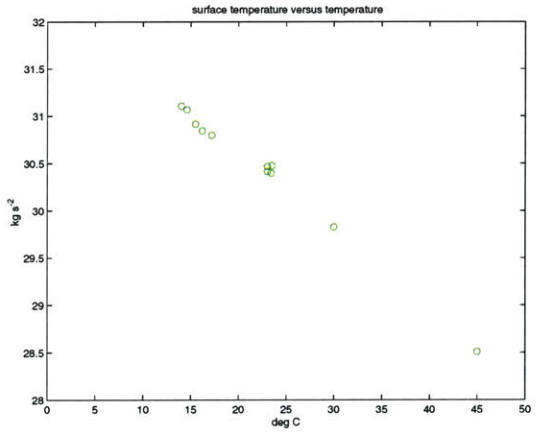

Figure 5-37: Hercolube C – air surface tension versus temperature.

were: surface tension, $\sigma_o = 1019.75$ kg s^{-2}, density, $\rho = 30.42$ kg m^{-3}, and dynamic viscosity, $\mu = 28.34$ kg s^{-1}m^{-1}.

Chapter 6

Inverse method

6.1 Introduction

One of the most interesting applications of the dispersion relation for capillary and dilational waves is using it to determine unknown surfactant film rheological parameters which may be difficult to measure directly. Experimental values can differ depending on whether the measurements are static, quasi-static, or dynamic, sometimes by as much as an order of magnitude (Hühnerfuss *et al.* 1985). A single (complex) parameter can be found by solving the dispersion relation (Jayalakshmi et al. 1994, Giermansta-Kahn, et al. 1999) directly. In this chapter, we will demonstrate that if some of the physical parameters of a system are known or can be obtained apriori, (μ, ρ, σ_o), and we have a data set, (ω, k), it is possible to analytically determine approximate values of multiple unknown parameters, $(\epsilon_o, \epsilon', \sigma')$, over the frequency range of the data by finding the optimal match of the solution space of the dispersion relation to the data set. This work has been previously discussed in Brown *et al.* (2002).

6.2 Description of the inverse method - obtaining surface rheological parameters from wave measurements

Once we have obtained data curves of wave number, k_R, and spatial damping coefficient, k_I versus frequency, ω_R or f, we can find the rheological parameters governing surface behavior by solving an inverse problem. An inverse problem is one in which the solution to an equation is known, but the parameters of the equation are not. In this case, we have a dispersion relation for which we know the wave number, spatial damping coefficient, frequency, temporal damping coefficient, bulk viscosity, bulk density and surface tension, k_R, k_I, ω_R, ω_I, μ, ρ and σ_o respectively, but are ignorant of the surface normal shear viscosity, surface dilational elasticity and apparent surface dilational viscosity, σ', ϵ_o and ϵ', respectively. For experimental data, it is relatively simple to measure the static surface tension, σ_0, and to obtain values for the kinematic viscosity, ν, and density of the underlying bulk fluid, ρ, thus we have considered these as known values. The unknown parameters can be found by solving an optimization problem by which each parameter is "guessed at", the dispersion relation is solved for $k(\omega)$ and compared to the data curve. The best match of the dispersion relation solution space to the data will occur for the correct set of parameters, σ', ϵ_o and ϵ'.

That we can obtain the rheological parameters in this fashion follows from the assumption of uniqueness of the shape of the complex solution space as determined by the physical parameters of the system. Underlying this assumption is the knowledge that the locations of both the mode sheets and the root coalescence points are highly dependent on the values of the parameters. To demonstrate this, we examine figure 6-1. This figure shows the movement of the two wave mode sheets in complex frequency - elasticity, ω-ϵ, space as surface tension, σ_o, is varied. The other parameters have the same values as given in section 4.2. The value of σ_o affects the location of the frequency coalescence point and indeed the shape of the solution space, i.e. the location of the two sheets within the three-dimensional projection space. This strong dependence

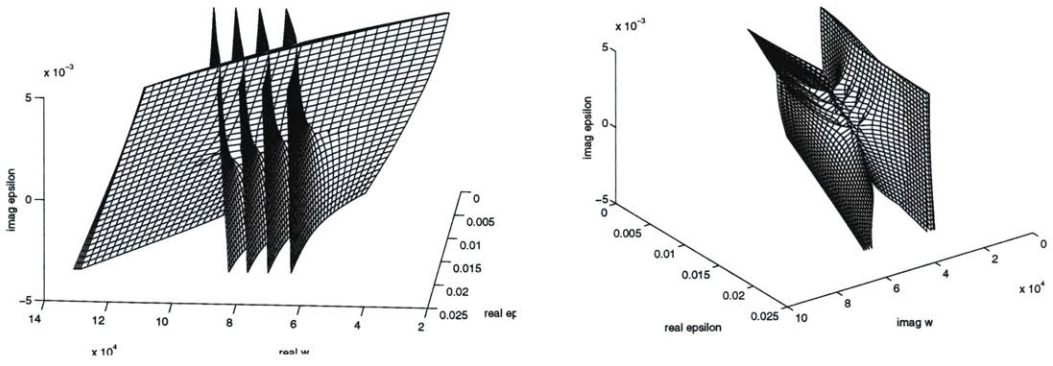

Figure 6-1: Three dimensional projections demonstrating the movement of the sheets of the solution space projected onto complex $\epsilon - \omega$ space due to the variation of surface tension, $\sigma_o = 45.0, 55.0, 65.0, 75.0 \times 10^{-3}$ kg s^{-2}.

on the parameters implies uniqueness of both the solution space and its projection into the data curve parameter space. If the projection is unique, then for a particular combination of the parameters, μ, ρ, k, σ_o and σ', the shape of the solution space of the dispersion relation in ϵ-ω space is uniquely determined. We will discuss later how the inverse method can be used to verify the uniqueness of the solution space and thus the surfactant rheological parameters associated with a data curve.

The optimization program forming to backbone of the inverse method is based on the simplex method (Press *et al.* 1995). It varies the parameter values, solves the dispersion relation for $k(\omega)$, compares each of the five roots to capillary wave data by calculating the error and optimizing the minimum of these values. Our program has three possible error algorithms, two which assume the availability of a single data curve, $Imag(k)$ vs. $Real(\omega)$, or, $Real(k)$ vs. $Real(\omega)$, and one which considers two data curves, $Imag(k)$ vs. $Real(\omega)$ and $Real(k)$ vs. $Real(\omega)$:

$$Error(\epsilon, \sigma, Imag(\omega)) \quad = \quad \sum_n \frac{Imag(k_{data}) - Imag(k)}{Imag(k_{data})}, \tag{6.1}$$

$$Error(\epsilon, \sigma, Imag(\omega)) = \sum_n \frac{Real(k_{data}) - Real(k)}{Real(k_{data})}, \tag{6.2}$$

$$Error(\epsilon, \sigma, Imag(\omega)) = \sum_n \left[\left(\frac{Real(k) - Real(k_{data})}{Real(k_{data})} \right)^2 + \left(\frac{Imag(k) - Imag(k_{data})}{Imag(k_{data})} \right)^2 \right]^{1/2}. \tag{6.3}$$

over n data points.

It is important to note that ϵ is function of ω. Therefore we cannot project the solution space for constant values of $(\epsilon_o, \epsilon', \sigma')$ onto (ω, k) and expect to find an exact match to experimental data, which will have been affected by a variable $\epsilon(\omega)$. When, however, conditions are such that ϵ varies slowly with ω over the data frequency range $\left(\frac{1}{\epsilon(\omega_O)} \frac{\partial \epsilon}{\partial \omega}(\omega - \omega_o) << 1\right)$, we can obtain approximate values of the parameters over this range. In such cases, we are provided with a simple analytical method for determining difficult to measure quantities from relatively easy to measure capillary wave data.

We demonstrate the inverse method by matching the complex solution space first to a simulated data set and then to an experimental data set (Bock 1989).

6.3 Evaluation of inverse method on noisy simulated data

6.3.1 Simulated data

To create the simulated data set pictured in figure 6-2 we chose values of the surface dilational elasticity and surface tension, $\epsilon_0 = 30.0 \times 10^{-3}$ kg/s^2 and $\sigma_0 = 70.0 \times 10^{-3}$ kg/s^2, to fall within typical ranges of published data for naturally occurring ocean surfactants (Wei & Wu 1992, Barger 1991, Garret 1967, Peltzer *et al.* 1992, Frysinger *et al.* 1992, Frew & Nelson 1992). The values of density and kinematic viscosity, $\rho =$ 1024 kg/m^3 and $\mu = 1.1264 \times 10^{-3}$ kg/ms, were chosen to correspond to seawater at 20.0°C. Both the apparent surface dilational viscosity and surface transverse viscosity,

$\epsilon' = 1.0 \times 10^{-5}$ kg/s and $\sigma' = 15.8 \times 10^{-3}$ kg/s, were chosen so as to create a data set near to a frequency coalescence point, little is known for certain about their probable values.

With the above values of the rheological parameters, the dispersion relation was solved for the solution space $k(\omega)$. A transect of this space was taken at $Imag(\omega) = 0.0$ (waves with no temporal damping) to produce the data set pictured in figure 6-2. The curves marked by o's correspond to the capillary wave mode and the curves marked by $\times$'s to the dilational wave mode. This capillary wave root is the simulated data set. The avoided crossing apparent around 5.8 Hz indicates the presence of a nearby root coalescence, in this case wavenumber coalescence, point.

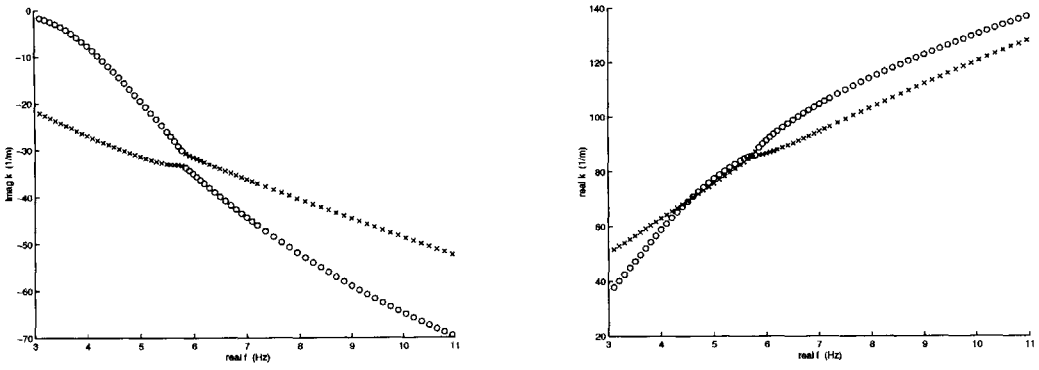

Figure 6-2: Transects at $Imag(f = \omega/2\pi) = 0.0$ Hz corresponding to the simulated data set of $k(\omega)$. The capillary wave data corresponds to the mode marked in $o's$, while the dilational wave data corresponds to the mode marked in $\times$'s.

The inverse method was applied to the simulated data to find the dilational elasticity, apparent surface dilational viscosity and surface normal shear vicosity, ϵ_0, ϵ' and σ', respectively. As the data set was simulated for constant parameter values, there was no frequency dependence of ϵ to be concerned with. The optimization program converged to the exact values of $\epsilon_0 = 30.0 \times 10^{-3}$ kg/s^2, $\epsilon' = 7.0 \times 10^{-5}$ kg/s, and $\sigma' = 100.0 \times 10^{-5}$ kg/s for the full range of data for both algorithms.

As a test for the uniqueness of the solution space, and thus the goodness of the set of rheological parameters that are found from the match of the solution space to the data set, the simplex was initialized to widely disparate initial conditions. For each initialization, the parameters found from the match converged uniquely to the exact values of ϵ_o, ϵ' and σ'. We considered smaller subsets of the data, both near to and away from the effects of wavenumber coalescence. All subsets converged uniquely to the correct parameter values. Away from the effects of the wavenumber coalescence point, no less than 5 data points were required for our optimization program to converge to the correct parameter values when the simplex was very poorly intialized.

6.3.2 Robustness of the inverse method - noisy simulated data

In an experimental data set, noise will be present and will affect the quality of the match. To examine its effect, we have added zero mean gaussian noise to the simulated data set and found optimal matches of the solution space to two smaller subsets of the data: one subset from the middle of the the curve, points (20:40), where the presence of the wavenumber coalescence point is felt, and the other from the high frequency end of the curve, points (50:70), away from the effects of the wavenumber coalescence point. Optimal matches of the solution space to each data set using all three error schemes, (6.1), (6.2, and (6.3), were found for increasing signal to noise ratios. The relative (percent) errors of the parameters compared to their actual values are displayed in in the left hand column of figure 6-4. With no noise present, the match to each of the subsets converged to the exact values of ϵ_o, ϵ' and σ'.

When error scheme (6.1) is used, the matches to data subset (20:40) provide significantly better parameter values than the matches to data subset (50:70). This is the benefit of the presence of the wavenumber coalescence point as a natural marker. In section 4.2, we showed that the solution space is drastically stretched in the region of a root coalescence point - the roots of the dispersion relation becoming infinitely sensitive to variations in the parameter values as this point is approached. The

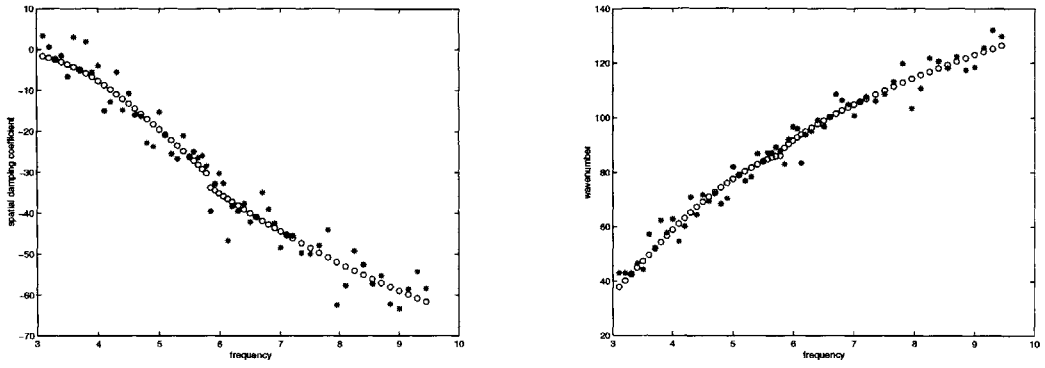

Figure 6-3: Capillary wave data, wave number and spatial damping coefficient versus frequency, $k(\omega)$, with added noise. Data points can be considered numbered 1:70, from the lowest frequency point to the highest frequency point. Points 20:40 are centered around the area most affected by the nearby presence of a wavenumber coalescence point while 50:70 are higher frequency data points away from the effects of wavenumber coalescence.

streching near this point makes it an unusual feature within the solution space - making it thereby easier to match the solution space to a data set within this region than to match it to a data set in a relatively flat region away from the effects of root coalescence. However, it also follows that because of this increased sensitivity, the match of the solution space to a data set near root coalescence is correspondingly more sensitive to noise.

Let us imagine a data set with some noise, $(k_N = k + N_k, \omega_N = \omega + N_\omega)$, for which we are trying to find the correct value of the constant in the mapping $\frac{\omega-\omega_o}{\sqrt{k-k_o}} = \gamma$. With our data we calculate

$$\gamma_N = \frac{\omega_N - \omega_o}{\sqrt{k_N - k_o}} = \frac{\omega + N_\omega - \omega_o}{\sqrt{k + N_k - k_o}} = \frac{\omega - \omega_o}{\sqrt{k - k_o}} \frac{1 + \frac{N_\omega}{\omega-\omega_o}}{\sqrt{1 + \frac{N_k}{k-k_o}}} = \gamma \frac{1 + \frac{N_\omega}{\omega-\omega_o}}{\sqrt{1 + \frac{N_k}{k-k_o}}}. \tag{6.4}$$

If the noise is small or if we are far from the wavenumber coalescence point, then $\gamma_N \approx \gamma$. But if the noise is large or if we are very close to the wavenumber coalescence point, we will be unable to get a good match. Thus, it is necessary to balance the

benefit from the wavenumber coalescence point providing a natural marker for the best match against increased sensitivity to noise in this region. We found that increasing the number of data points by extending the range of the data subset beyond the immediate area of the wavenumber coalescence point was effective in ameliorating the noise. The same benefit comes from matching both the wavenumber and the spatial damping data sets using error scheme (6.3) rather than by matching only the spatial damping data set using error scheme (6.1). The former doubles the number of data points, thereby reducing the sensitivity of the match on the noise present.

When error scheme (6.3) is used, the matches to the surface dilational viscosity and surface normal shear viscosity, ϵ_o and σ', are excellent for both data subsets, both near to wavenumber coalescence, (20:40), and away from its effects, (50:70). The match to the apparent surface dilational viscosity, ϵ', is not nearly as good, even in the region of the wavenumber coalescence point. This indicates that the shape of the solution space throughout this region and the mapping of the roots to the parameters at the wavenumber coalescence point are all relatively insensitive to this parameter. (Recall that the simulated data set was created for a constant value of ϵ' and therefore variation with respect to ω has no effect on this match.) The relative insensitivity of the match to this parameter means that, for this particular frequency range, it is obtained with less accuracy than the other parameters.

In general, for all parameters, the surface dilational elasticity, surface apparent dilational viscosity and surface normal shear viscosity, ϵ_o, ϵ' and σ', respectively, we find that error scheme (6.3) utilizing both wave number and spatial damping coefficient data gives much better results than either error scheme (6.2) or (6.1). Error scheme (6.1) gives better results than (6.2) for ϵ_o and (6.2) better than (6.1) for σ'. This implies that the values of the spatial damping coefficient are more dependent on ϵ_o and the values of the wave number more dependent on σ'. Note also that all schemes give much better results for σ' in the 20:40 range than in the 50:70 range. This implies that σ' is more important at the lower end of the frequency range where gravity-capillary resonance occurs. As was seen in section 4.3, it has little to do with capillary-dilational resonance. None of the error schemes gives a particularly good

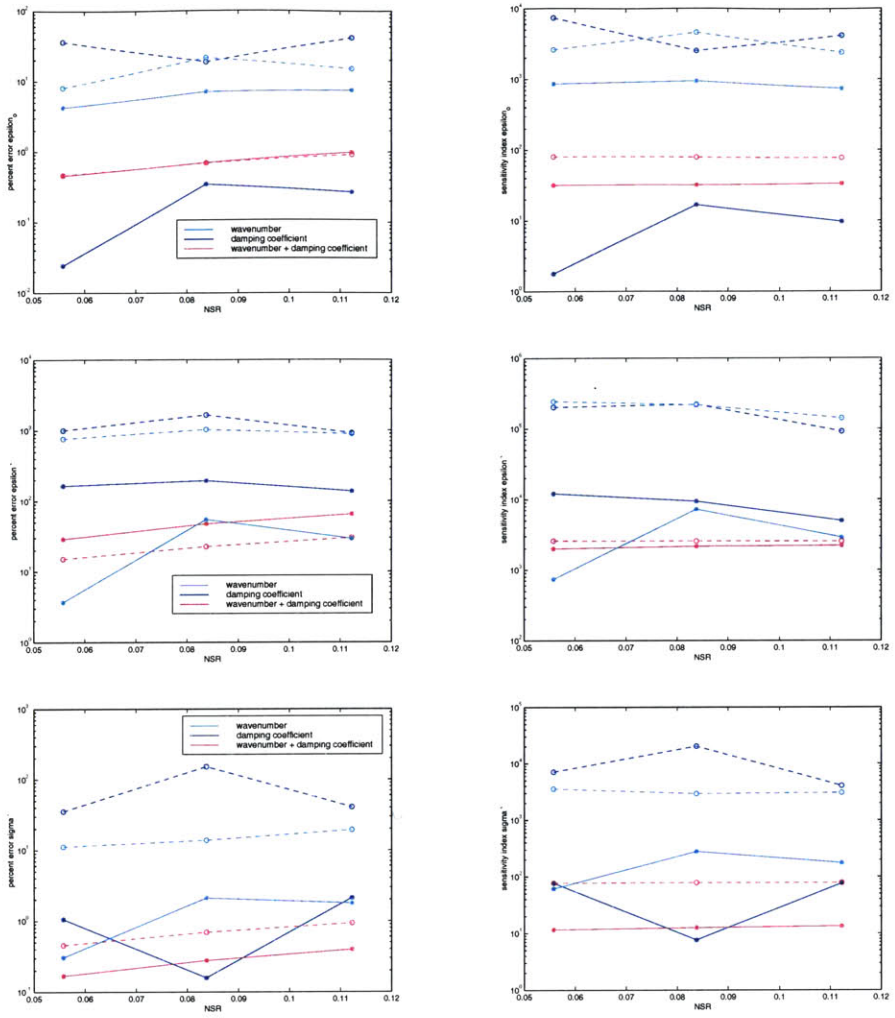

Figure 6-4: In the left hand column are plotted the relative, or percent, errors of optimized values of the surface dilational elasticity, surface apparent dilational viscosity and surface normal shear viscosity, ϵ_o, ϵ' and σ', obtained by the inverse method when compared to the actual values of the simulated data set versus the noise to signal ratio (NSR) of the data set. In the right hand column are plotted the sensitivity indices of ϵ_o, ϵ' and σ' versus the NSR of the data set. The solid lines indicate the set of data points taken from the region of the simulated data set affected by the presence of a nearby wavenumber coalescence point. Relative errors and sensitivity indices for this portion of the simulated data set are marked with $*$'s. The dashed lines indicate points taken from the higher frequency range of the simulated data set which is away from the effects of wavenumber coalescence. Relative errors and sensitivity indices for this portion of the simulated data set are marked with $\circ$'s. The cyan lines indicate relative errors and sensitivity indices found for the error scheme (6.2), the blue lines indicate relative errors and sensitivity indices found for the error scheme (6.1), and the dashed line indicate the same found for error scheme (6.3).

results for ϵ'.

We can calculate a noise sensitivity index for each of the parameters for each of

the error schemes above, where we define this index as:

$$SI = \left| \frac{\frac{E_Q}{Q}}{\frac{\sigma_N}{\overline{k}}} \right| \tag{6.5}$$

where E_Q is the error in the estimate of parameter Q, σ_N is the standard deviation of the noise in the signal and $\overline{k}$ is the mean value of the data without any noise present. These values are presented in the right hand column of figure 6-4. We see that the noise sensitivity index corresponds well with the relative error of the parameters.

6.3.3 Application of inverse method on published experimental data

Next we will look at a match to an experimental data set. Both the effects of noise and variation of the parameters with respect to frequency will now effect the quality of the match, and therefore the values of the parameters obtained.

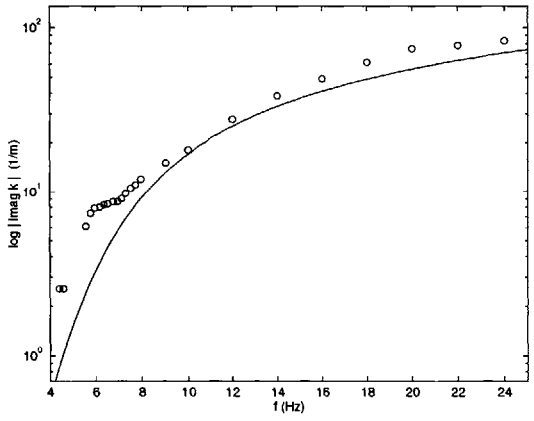

Figure 6-5: Reproduction of a data set (Bock 1989) showing variation of spatial damping, $(Imag(k))$, with frequency, $(f = \omega/2\pi)$, for capillary waves propagating across the surface of Hercolube C at 45°C. The data set is marked in o's. The solid line corresponds to Bock's fit of the dispersion relation to his data assuming that both f and σ are real and $\epsilon = 0.0$.

The experimental data set shown in figure 6-5 is reproduced from a plot of this data in Bock (1989). Bock offered the following properties of the surfactant, Hercolube C, a pentaerythritol ester, at 45.0 °C as surface tension = 27.7 $\times 10^{-3}$ kg/s^2, density = 940

kg/m^3 and kinematic viscosity = 14.1 $\times 10^{-6}$ m^2/s. In the experiment, capillary waves were produced at the air-surfactant interface by a vibrating metal bar at a known frequency, $Real(\omega)$. Complex k was measured using a laser slope gauge. Bock's fit of the dispersion relation to his data assumed $\epsilon = 0.0$, with neither σ nor ω considered to be complex. As we can see in the figure, this fit is unable to account for the small bump appearing in his data near 6.0 Hz which he attributes to resonance between the capillary and dilational wave modes.

Although it is not necessary to solve a fully complex dispersion relation to obtain a match (for example, an experimental data set may be assumed to have negligible temporal damping, $Imag(\omega) = 0.0$), it is propitious to do so. As we will see below, a small amount of damping may have a significant effect on the shape of the dispersion relation solution space. Allowing $Imag(\omega)$ to vary may not only result in a significant improvement to the match to the data, but in this case allowed us to capture the physics of the experimental waves when the match with the assumed real paramenters, w, ϵ and σ, by the author could not.

To try to find a better match to Bock's data using our optimization program, we varied four parameters, σ', ϵ_o, ϵ' and $Imag(\omega = 2\pi f)$. As we only had the curve of spatial damping versus real wave frequency available, we used error scheme (6.1) for the match. In table 6.1 we display the parameter values from matching both the entire data set and subsets both near and away from the wavenumber coalescence point.

This data set is in many ways unfortunate. There is no wavenumber data to aid in the match. Although there are a good number of closely spaced points near the region of the wavenumber coalescence point, the higher frequency points are spaced much further apart making it difficult to distinguish the effects of noise from parameter variation. Both the increased number of data points and the increased senstivity of the solution space in the region of the bump near 6.0 Hz cause this feature to dominate the match of the full data set. In fact, as we can see in figure 6-6, we are unable to obtain any match to the data which passes neatly through the higher frequency points.

ϵ_0 (10^{-3} kg/s^2)	ϵ' (10^{-5} kg/s)	σ' (10^{-5} kg/s)	$Imag(f)$ (Hz)
Data Set:	1	2	3
Data Point Range:	3:24	3:15	16:24
Parameters			
ϵ_0	59.1	62.5	64.7
ϵ'	-70.4	-84.1	-61.2
σ'	0.542	-3.453	.979
$Imag(f)$	0.176	0.23	.61

Table 6.1: This table gives the values of ϵ_0, ϵ', and σ', determined by an optimal match of the solution space to three data ranges, each denoted a:b. Data points can be considered numbered 1:24, from the lowest frequency point to the highest frequency point. The first range is the entire set neglecting the first two points, the second and third ranges run over points near to a wavenumber coalescence point, the last range is located away from the effects of the wavenumber coalescence point.

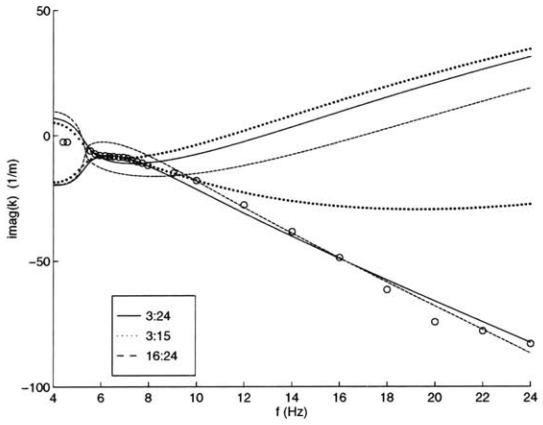

Figure 6-6: This figure presents the fits to Bock's data, damping coefficient, $Imag(k)$, versus frequency, f, from the parameters found from the matches of the solution space to the data ranges listed in table 6.1.

From our efforts with the simulated data set, we have learned that when using error scheme (6.1) the optimal data set is one which is near to a root coalescence point but also has several points extending beyond this region to ameliorate the effects of noise. This most nearly corresponds to our match to the entire data set. We also note that the values obtained for ϵ_o and ϵ', the parameters which depend on frequency, do not vary significantly over the short data ranges, [(3:15),(16:24),(3:24)], despite the incompleteness of the data set and the probability of noisy high frequency data. This implies that the inverse method is applicable to this data set - the values obtained

for ϵ_o and ϵ' can be thought of as approximate values over this frequency range. The variability of σ', which does not depend on the frequency of the disturbance, indicates that the solution space is relatively insensitive to this parameter in this frequency range.

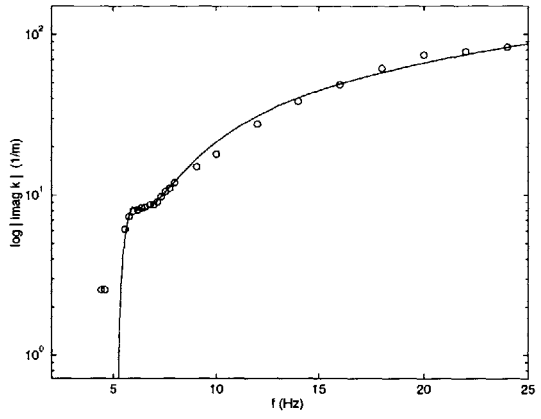

Figure 6-7: Comparison on a semilog scale of capillary wave temporal damping vs. wave frequency between the measured data, o (Bock, 1989), and the best fit to the entire data set, $-$, obtained by the optimization program.

This best fit, depicted in figures 6-7 and 6-23, was found for $\epsilon_0 = 59.1 \times 10^{-3}$ kg/s^2, $\epsilon' = -70.4 \times 10^{-5}$ kg/s, $\sigma' = 0.542 \times 10^{-5}$ kg/s and $Imag(f) = 0.176$ Hz and accounts well for the small bump near 6.0 Hz. Note that it was necessary for both σ and ω to be complex to achieve this fit as was also true for all the other fits listed in table 6.1. This implies that the surface normal shear viscosity is important to the match of the solution space to this experimental data. Despite the relative insensitivity of the solution space to this parameter as compared to other parameters, it cannot be neglected. Furthermore, we see that the assumption of the production of constant amplitude waves was not correct. For whatever reason, the vibration of the bar did not remain steady, but produced waves of slightly lower amplitude as time passed. Thus ω was complex and the waves decayed in time as well as space.

We can understand the match to the data by examining figures 6-23(a) and 6-9. In figure 11(a), we see an avoided crossing. The two modes appear to exchange character around 5.5 Hz. In figure 6-9 we see that it is this frequency at which

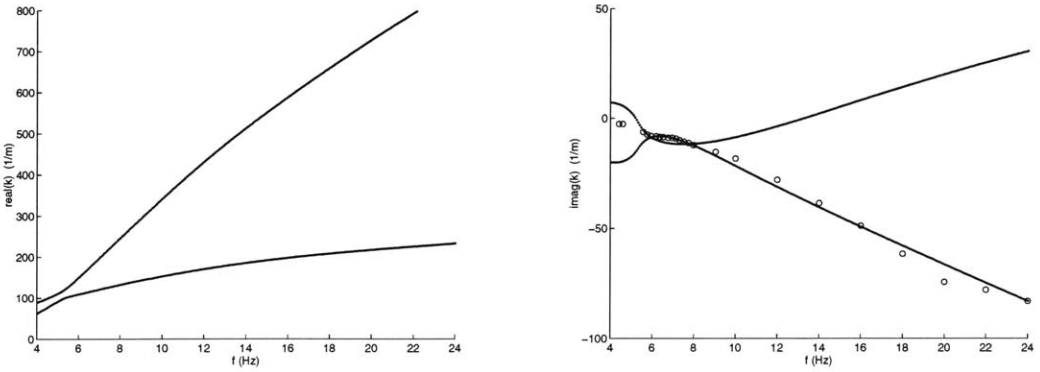

Figure 6-8: These plots show the results of the optimization program to find the best match to the entire range of Bock's data (1989), marked in o's. CWM and DWM correspond to the capillary and dilational wave modes respectively. The optimization program found $\epsilon_0 = 59.1 \times 10^{-3}$ kg s^2, $\epsilon' = -70.4 \times 10^{-5}$ kg s, $\sigma' = 0.542 \times 10^{-5}$ kg s and $Imag(f) = 0.176$ Hz and accounts well for the small bump near 6.0 Hz.

the branch cut lies, the branch or frequency coalescence point occuring at a larger imaginary frequency. Because of the cut at this location, the physical waves exchange modal solutions. We can see in figure 6-23(b) that the root which passes through the data points at low frequencies is not the same root which passes through the data points at high frequencies. It is at the cut around 5.5 Hz where the physical modal solution switches roots, ensuring that the roots which pass through the data points at frequencies both greater and less than 5.5 Hz do, indeed, correspond to the capillary wave mode.

Unfortunately little is known or can be said about the properties of Hercolube C. While roots of the dispersion relation for the parameters obtained well match the data curve, the expected values for these parameters are unknown. In addition, very few experiments with other surfactants are conducted at the low frequency range we are investigating. At best we can say that the value obtained for the surface dilational elasticity, ϵ_o, is of the order of magnitude of values found for experiments with other surfactants at a variety of frequency ranges (Earnshaw *et al.* 1988, Frew and Nelson 1992, Hühnerfuss *et al.* 1985, etc.), and that the magnitudes of the values obtained for the apparent viscosity term, ϵ', and the surface normal shear viscosity, σ', are

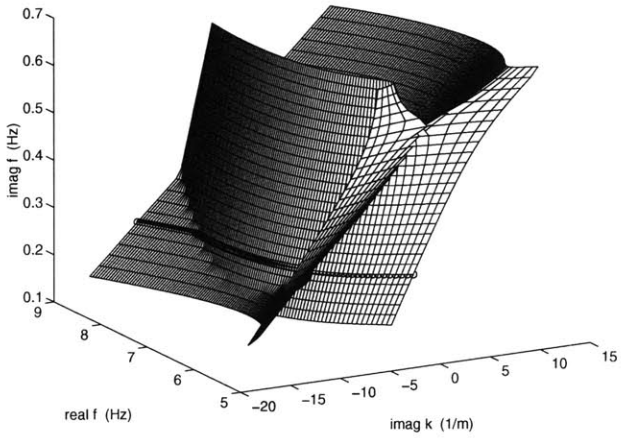

Figure 6-9: Projection of the 'best match' solution space of $\Delta(\omega, k, \epsilon, \sigma) = 0$ onto $(Real(f), Imag(f), Imag(k))$ three space. A frequency coalescence point is visible at the top of the figure. The transect at $Imag(f) = 30.0$, marked by o's, corresponds to the best match to the measured data (Bock, 1989).

several orders of magnitude larger than values found for other surfactants with wave disturbances of $\mathcal{O}(10^4\text{Hz})$ (Earnshaw *et al.* 1988, Haard and Neumann, 1981).

The negative sign attached to the value of ϵ' is entirely possible within the context of its development:

$$\epsilon = \mid \tilde{\epsilon} \mid e^{i\theta} + i\omega(\kappa + \eta) = \mid \tilde{\epsilon} \mid \cos\theta + i\omega \left(\mid \tilde{\epsilon} \mid \frac{\sin\theta}{\omega} + \kappa + \eta \right) \tag{6.6}$$

If the phase difference between $\delta\sigma_D$ and δA, θ, is between $\frac{3\pi}{2}$ and 2π, then $\mid \tilde{\epsilon} \mid e^{i\theta}$ will make a positive contribution to ϵ_o and a negative contribution to ϵ'. If the negative contribution of $\mid \tilde{\epsilon} \mid \sin\theta/\omega$ to ϵ' is larger than that of $\kappa + \eta$, then ϵ' will be negative. This implies a relaxation time of the order .1 s, roughly the period of the waves.

6.4 Recommendations for field data analysis

Field samples of surfactant films are often analysed *ex-situ* and presented in terms of $\pi - A$, , $|\epsilon| - A$, or $\pi - |\epsilon|$,isotherms with the eventual goal of developing models

for microlayer films to predict the viscoelastic effect they will have in the field (Frew & Nelson, 1992). These isotherms are found in terms of quasi-static quantities: the modulus of elasticity, $|\epsilon|$ corresponding to ϵ with zero phase (no sinusoidal dilation of the interface); surface pressure, $\pi = \sigma_e - \sigma_o$ where σ_e refers to the static surface tension of a fluid uncontaminated by a surfactant film, and film surface area A which is varied stepwise.

The difficulty is that these quasi-static isotherms are not generalizable to dynamic conditions. For these conditions, we need in addition to determine the phase of ϵ as well as the surface viscosities, η_N and η. These parameters can be found from examining *ex-situ* sample dynamically. Assuming that bulk viscosity, μ, and density, ρ, are known for the lower bulk fluid, with measurements of frequency and wave number, $\omega(k)$, and static surface tension, $\sigma_o(c,T)$, (where c and T refer to concentration and temperature), the values of surface dilational elasticity, ϵ_o, surface apparent dilational viscosity, ϵ', and surface normal shear viscosity, σ', can be found by matching the complex solution space to the data. Once $\epsilon_o = \varepsilon_o$ is found, it should be possible to obtain the phase of the complex elasticity parameter, θ, by using the value obtained for $|\epsilon|$ from the $\pi - |\epsilon|$ isotherm using the expression $|\epsilon| \cos\theta = \epsilon_o$. It is possibilities to measure the sum of the surface dilational and shear viscosity, $\kappa + \eta$, directly using a method such as Hirsa *et al.* (1997), or to measure κ and η separately (see Edwards *et al.* 1991 for example). With these data, it is possible to find the relaxational elasticity, ε', from

$$\epsilon = \epsilon_o + i\omega\epsilon' = \varepsilon_o + i\omega(\varepsilon' + \kappa + \eta). \tag{6.7}$$

6.5 Application of inverse method on experimental data

The inverse method was applied to the palmitic and myristic acid and Hercolube C data sets. The palmitic and myristic data sets only have good quality wave number data. This meant that the application of the inverse method was limited to the use

of algorithm

$$Error(\epsilon, \sigma) = \sum_n \frac{Real(k_{data}) - Real(k)}{Real(k_{data})}. \tag{6.8}$$

As discussed in section 6.3.2, when using only wave number data, we expect an accurate estimate of σ', a less accurate estimate of ϵ and a poor estimate of ϵ'.

6.5.1 Palmitic acid monolayers

The inverse method converged excellently to all six data sets with the error criterion for the match of the dispersion relation solution space to the data curve less than 2 percent in all cases. These matches are depicted in figures 6-10 – 6-12.

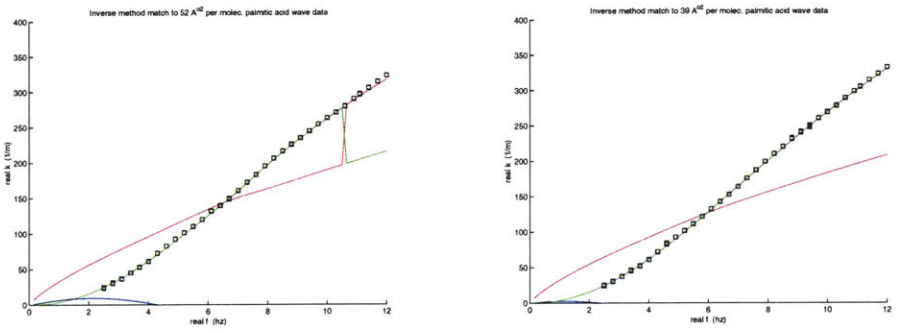

Figure 6-10: Matches of inverse method to wave number versus frequency data for waves traveling on a 0.01 N HCl aqueous solution with a palmitic acid film of concentration 52 and 39 square angstroms per molecule, respectively.

The values of ϵ_o, as shown in figure (6-13) and given in table (6.2) are remarkably flat across the frequency spectrum and relatively small. This was unexpected, given the results of Adam (1932) in figure 6-14b which predicts much higher values of the static elastic modulus at similar surfactant concentrations. However, it is consistent with the *in-situ* Wilhelmy-Blodgett measurements shown in figure 6-14a. There is no data for comparison with the obtained values of surface relaxational elasticity or surface tangential elasticity. Note that we expect values of the surface tangential elasticity to be good due to its strong dependence on wave number data as this is

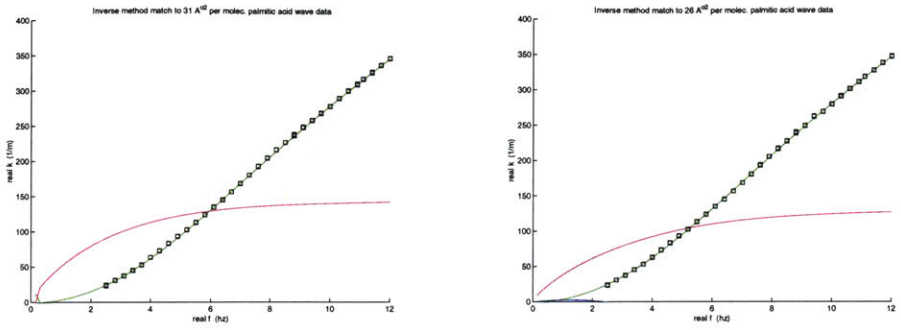

Figure 6-11: Matches of inverse method to wave number versus frequency data for waves traveling on a 0.01 N HCl aqueous solution with a palmitic acid film of concentrations 31 and 26 square angstroms per molecule, respectively.

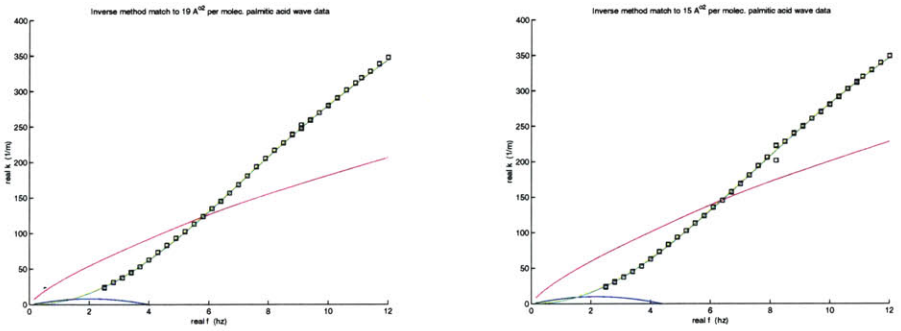

Figure 6-12: Matches of inverse method to wave number versus frequency data for waves traveling on a 0.01 N HCl aqueous solution with a palmitic acid film of concentrations 19 and 15 square angstroms per molecule, respectively.

the data used in algorithm 6.2. Also, Wilhelmy-Blodgett measurements are of static elasticity while the inverse method finds dynamic elasticity.

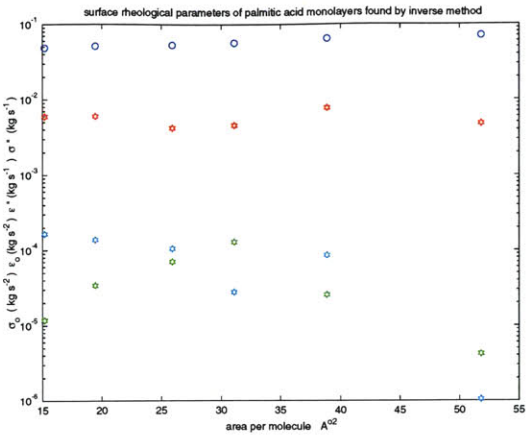

Figure 6-13: Values for the surface rheological parameters for different concentrations of palmitic acid monolayers found by applying the inverse method to wave data.

A^{o2}/molec.	σ_0 mN/m	ϵ_0 mN/m	ϵ' N s / m	σ' N s/m
51.785	71.07	0.48	0.4238e-5	0.10595e-5
38.839	64.81	0.78	2.5912e-5	8.6757e-5
31.071	57.1	0.46	12.927e-5	2.7964e-5
25.892	53.49	0.42	7.0375e-5	10.494e-5
19.419	51.5	0.6	3.4441e-5	13.901e-5
15.157	48.8	0.6	1.1874e-5	16.695e-5

Table 6.2: Results of the inverse method: rheological parameters for various concentrations of palmitic acid monolayers on 0.01 N HCl aqueous solution.

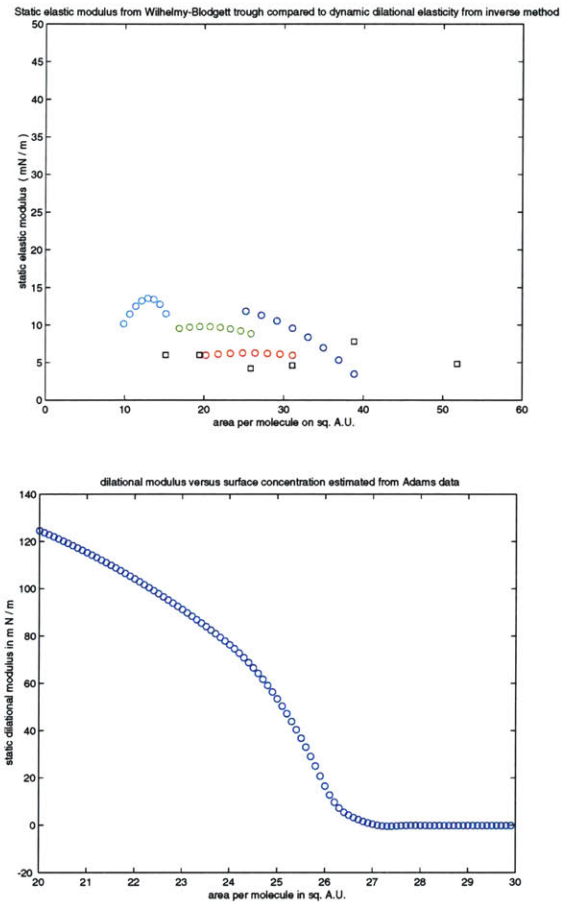

Figure 6-14: The upper plot is a comparison of static elastic modulus measurements made with the *in-situ* Wilhelmy-Blodgett trough (colored symbols) to dynamic dilational elasticity measurements found from applying the inverse method to wave data (black squares). The lower plot shows static elastic modulus calculated from surface tension measurements made by Adams (1932).

6.5.2 Myristic acid monolayers

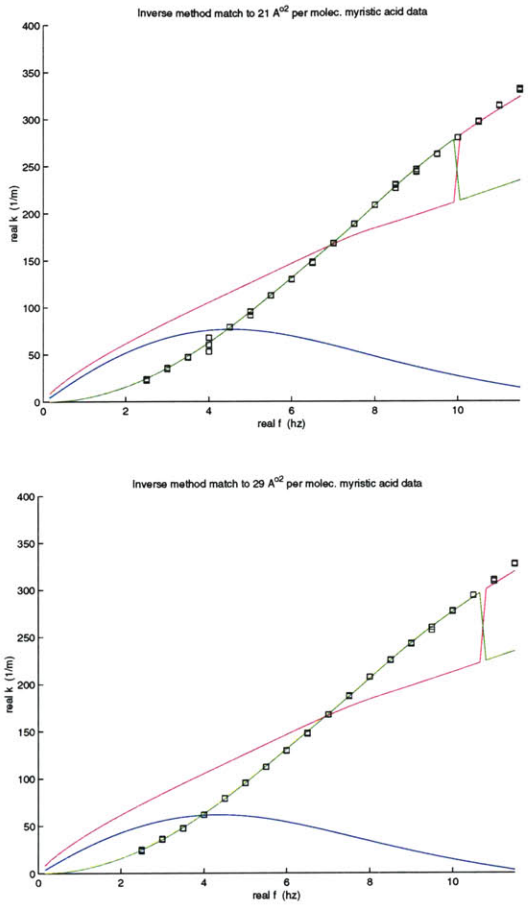

Figure 6-15: Matches of inverse method to wave number versus frequency data for waves traveling on a 0.01 N HCl aqueous solution with a myristic acid film of concentrations 21 and 29 square angstroms per molecule, respectively.

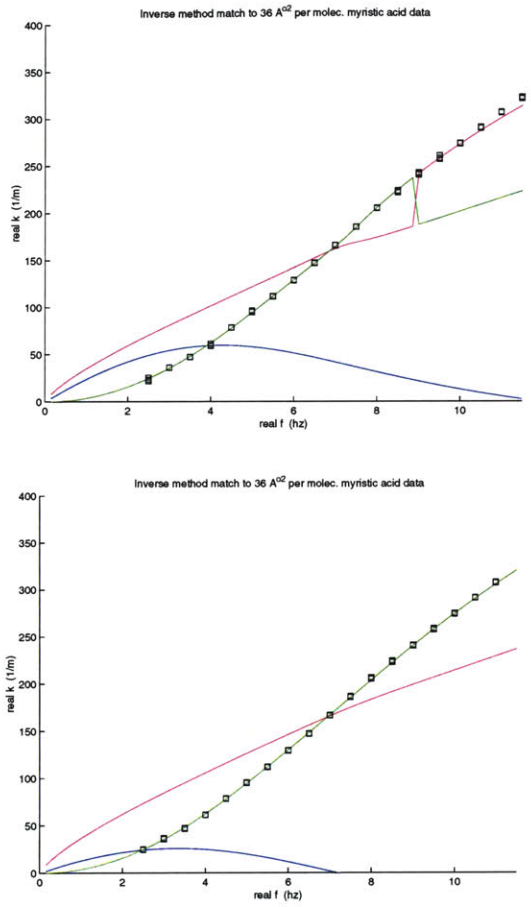

Figure 6-16: Matches of inverse method to wave number versus frequency data for waves traveling on a 0.01 N HCl aqueous solution with a myristic acid film of concentrations 36 and 46 square angstroms per molecule, respectively.

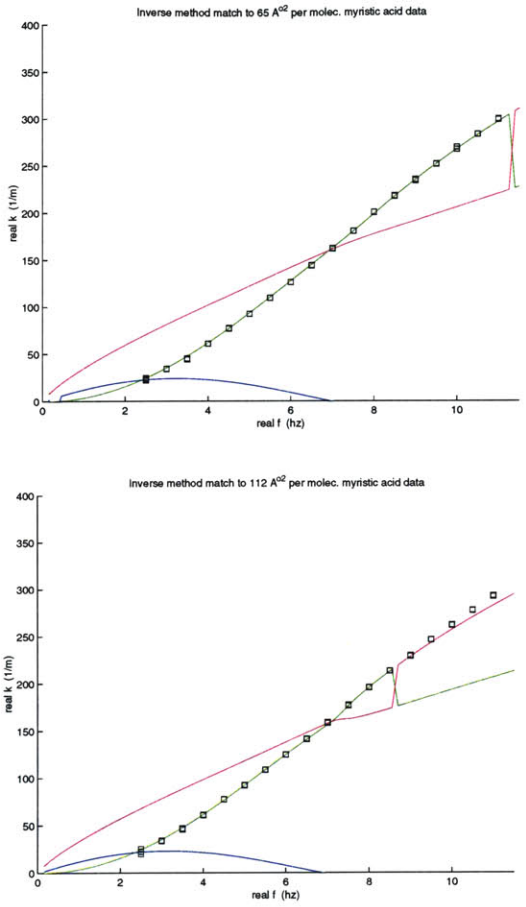

Figure 6-17: Matches of inverse method to wave number versus frequency data for waves traveling on a 0.01 N HCl aqueous solution with a myristic acid film of concentrations 65 and 112 square angstroms per molecule, respectively.

Like the results with palmitic acid, the values of the dilational elasticity,ϵ_o, as shown in figure (6-13) and given in table (6.3) are remarkably flat across the frequency spectrum and relatively small. They are consistent with the *in-situ* Wilhelmy-Blodgett measurements shown in figure 6-19a. The values of static elastic modulus calculated from the surface tension measurements of Adam (1932) have a wholly different trend. There is no data for comparison with the obtained values of surface

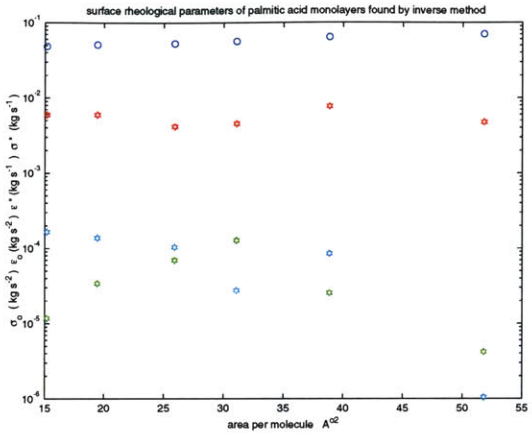

Figure 6-18: Values for the surface rheological parameters for different concentrations of myristic acid monolayers found by applying the inverse method to wave data.

relaxational elasticity or surface tangential elasticity. Again we expect values of the surface tangential elasticity to be good due to its strong dependence on wave number data as this is the data used in algorithm 6.2. And again, Wilhelmy-Blodgett measurements are of static elasticity while the inverse method finds dynamic elasticity.

A^{o2}/molec.	σ_0 mN/m	ϵ_0 mN/m	ϵ' N s / m	σ' N s/m
112.07	6.96	1.17	-7.42e-5	87.3e-5
65.37	5.66	1.07	-3.42e-5	6.52e-5
46.15	4.84	0.98	-1.00e-5	5.35e-5
35.66	4.32	1.09	-4.95e-5	76.8e-5
29.06	3.97	1.0	-2.13e-5	68.5e-5
21.20	3.54	1.0	-2.59e-5	68.0e-5

Table 6.3: Results of the inverse method: rheological parameters for various concentrations of myristic acid monolayers on 0.01 N HCl aqueous solution.

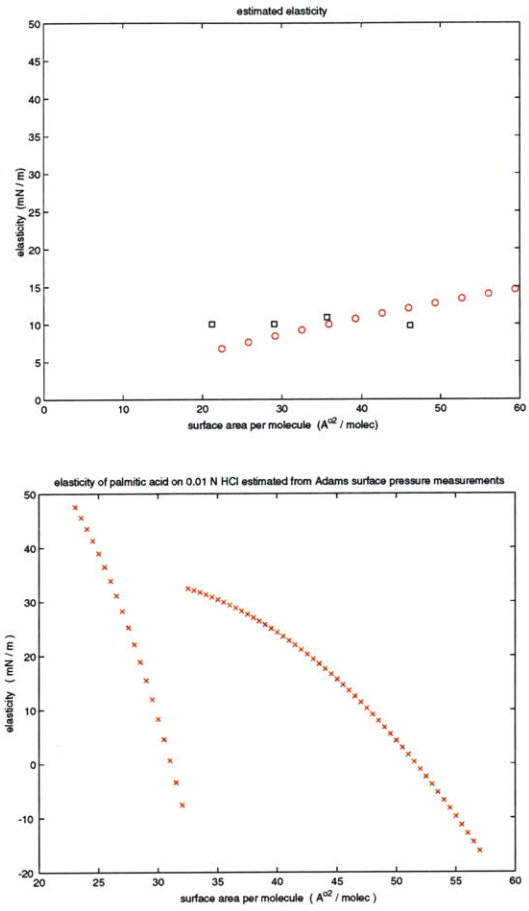

Figure 6-19: The upper plot is a comparison of static elastic modulus measurements made with the *in-situ* Wilhelmy-Blodgett trough (colored symbols) to dynamic dilational elasticity measurements found from applying the inverse method to wave data (black squares). The plot shows static elastic modulus calculated from surface tension measurements made by Adams (1932).

6.5.3 Hercolube C

Rather surprisingly, the inverse method was not able to converge to the data set as it was. It was not possible to converge to the entire range of the damping coefficient data (figure 6-20) at the same time that it converged to the entire range of the wave number data (figure 6-21). A convergence to the wave number could only be found for the lower end of the range.

Furthermore, there was the issue of the the match capturing the physics - did the resulting solution space from these matches of the inverse method to the data show the resonances near 4.5 and 5.5 hertz that were apparent from the wave slope spectrum in figure 6-22?

The answer was no. The match to the damping coefficient data had a resonance event near 4 hertz and the match to the lower portion of the wave number data had one at 5.5 hertz. But neither match described both the precipitous dip in the wave slope spectrum near 4.5 hertz as well as the small dip near 5.5 hertz.

So, what was happening? The data were highly repeatable and amplitude independent. The modulation was small enough to have little effect on the inverse method's ability to unambiguously match a curve. The inverse method itself had been rigorously tested on simulated data, published data and experimental data. The input parameters, surface tension, dynamic viscosity and density of the bulk fluid, had been carefully measured in outside laboratories. Even efforts at varying these parameters had not improved the match of the solution space to the data.

The answer lies in the presence of a branch/saddle point in the solution space near 5 hertz. It was often noted while varying the above rheological parameters in the hope that one of these might have ill affected the inverse method's ability to match the data, that the wave number curve above approximately 5 hertz of the solution space generally paralleled the data curve. The distance between the parallel curves was generally of the order of about 30 1/m, roughly π divided by the distance between sensors, 0.1 m.

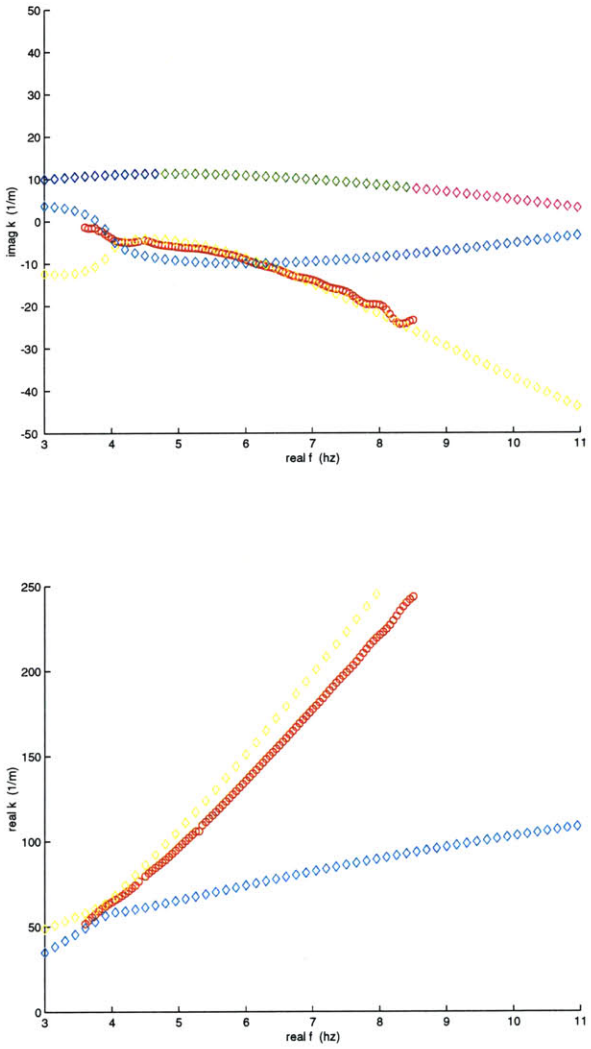

Figure 6-20: Match of the inverse method to damping coefficient data.

The reader will recall that the wave number is calculated as

$$k_R = \frac{\phi_2 - \phi_1}{x_2 - x_1} + \frac{n2\pi}{x_2 - x_1}. \tag{6.9}$$

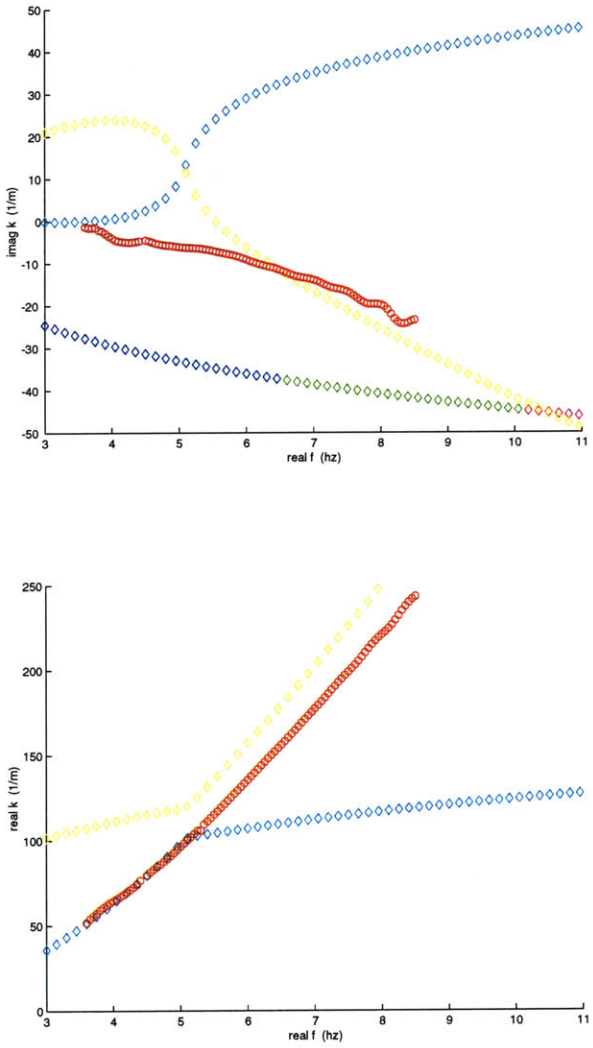

Figure 6-21: Match of the inverse method to the lower end of the wave number data range.

Factors of 2π have to do with the number of wave lengths between the signal measured at the two sensor locations. The winding number, n, is estimated to make the curve appear smooth along the whole frequency range.

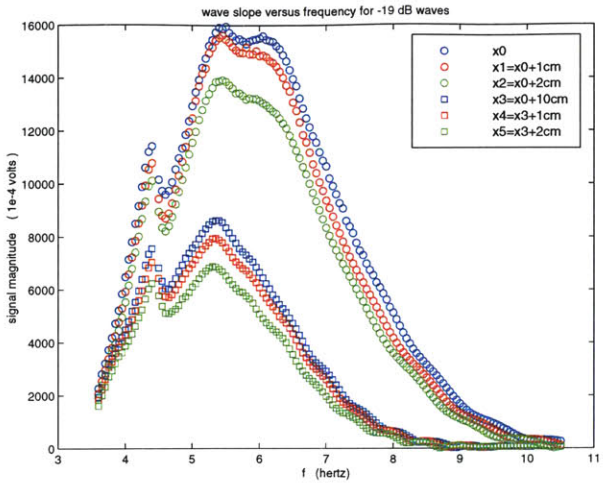

Figure 6-22: Wave slope spectra of Hercolube C at six tank locations. The figure was made for a wave maker power setting of -19dB.

To see if, indeed, a factor of π, rather than 2π, would affect the ability of the inverse method to match the data, the wave number data was recalculated as

$$k_R = \frac{\phi_2 - \phi_1}{x_2 - x_1} + \frac{n2\pi + \pi}{x_2 - x_1}. \tag{6.10}$$

above 4.7 hertz. The result was a nearly perfect match of the solution space to the data as shown in figure 6-23 with $\epsilon_o = 0.545$ kg s^{-2}, $\epsilon' = -0.0019$ kg s^{-1} and $\sigma' = 2.052 \times 10^{-5}$ kg s^{-1} for Im$(f) = 0.2$ hertz at a temperature of 23 deg C. These parameters compare favorably to the parameters found for the match to Bock's (1987) Hercolube C data at 45 deg C: $\epsilon_o = 0.0591$ kg s^{-2}, $\epsilon' = -0.0007$ kg s^{-1} and $\sigma' = 0.542 \times 10^{-5}$ kg s^{-1} for Im$(f) = 0.176$ hertz.

Taking a look at the solution space from this match projected into $k - \omega$ space in figure 6-24, we see the presence two root coalescence points. They are apparent in the upper figure (projection) in the righthand two Riemann sheets. One point is above the real frequency axis and the other below. In the lower figure (projection), the two points appear on either side of the real wave number axis.

To see the location of these two points along the real frequency axis, we examine

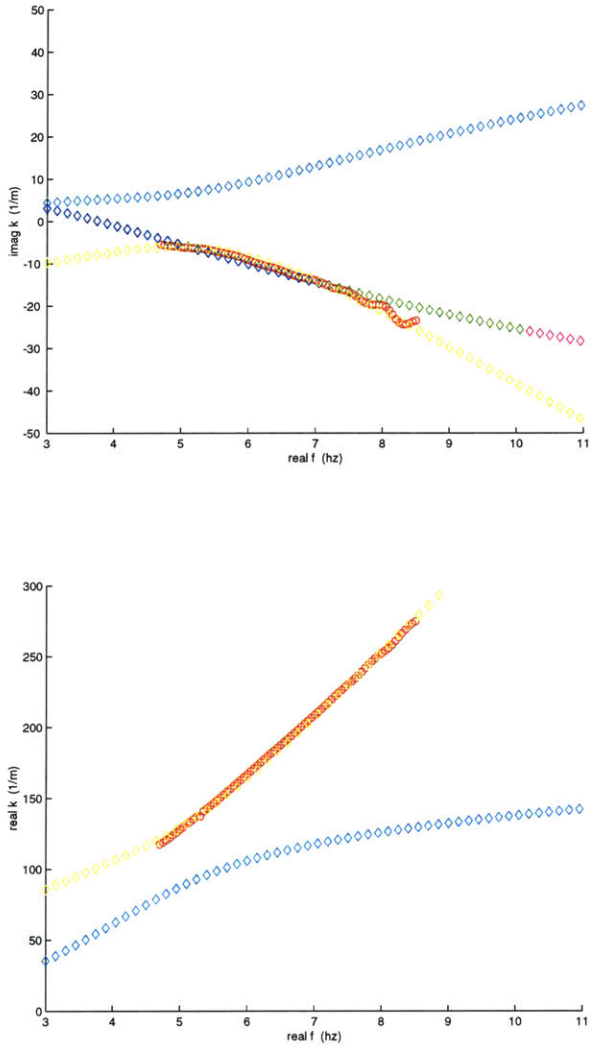

Figure 6-23: Match of the inverse method to the data range above 4.7 hertz with the wave number calculated with an extra factor of $\pi/.1$

the lower figure (projection) of figure 6-24 from above in figure 6-25. From this vantage point, we can see that the upper root coalescence point is near 5.2 hertz and the lower root coalescence point near 5.0 hertz.

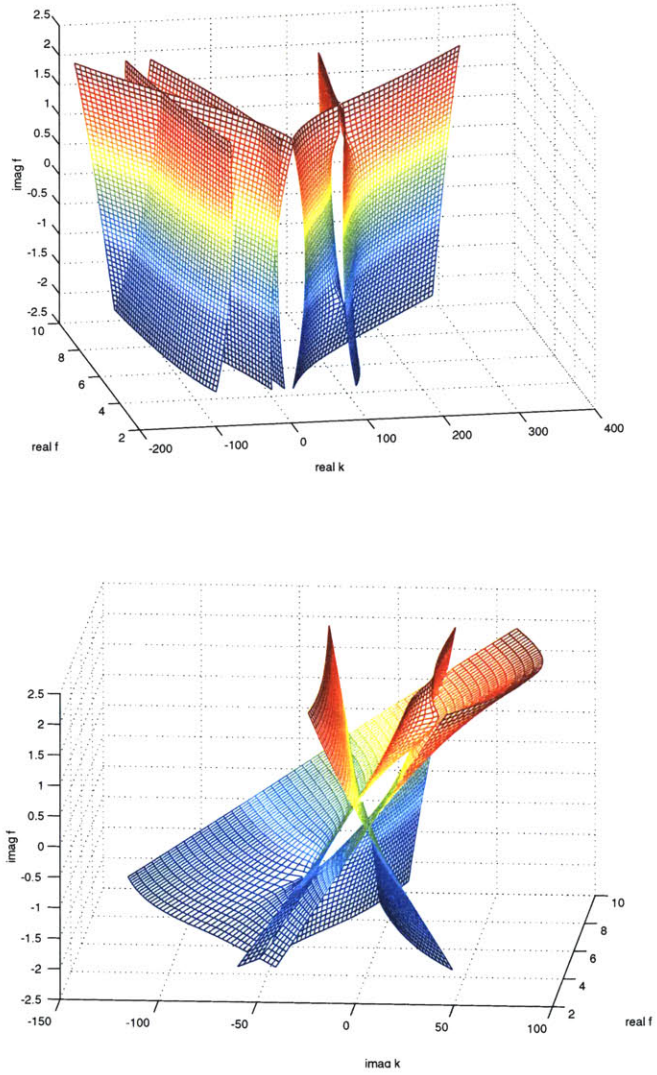

Figure 6-24: Projections of the dispersion relation solution space found for match of the inverse method to the data range above 4.7 hertz with the wave number calculated with an extra factor of $\pi/.1$ The upper figure (projection) shows all five roots of the dispersion relation, the lower figure (projection) only shows 3 roots to preserve the scale of the root coalescence.

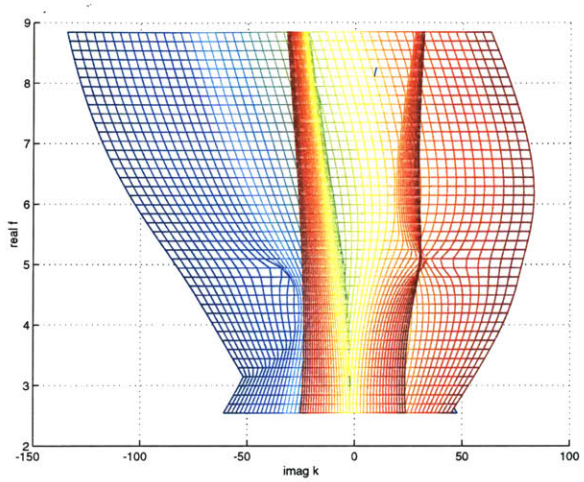

Figure 6-25: Above view of the lower projection in figure 6-24.

The match to the solution space found by the inverse method characterized the appearance of resonance near 5.5 hertz very well. The actual root coalescence point lay at $5.15 + 1.02i$ hertz, and it is at 5.35 hertz that the dip in the wave slope spectra shown in figure 6-22 begins.

It is interesting to note in figure 6-26 that the solution space matches the wave number data below 4.3 herz (not altered by a factor of π). It does not, however, match the damping coefficient data.

This brings us to that region between 4.3 hertz and 4.7 hertz where we see the precipitous dip in the wave slope spectrum. It is unlikely that gravity-capillary resonance causes the enormity of this dip. If we look at figure 6-27, we see that gravity-capillary resonance occurs out near $4.2(1 \pm i)$ hertz. Gravity-capilllary resonance is apparent in the upper plot of this figure between two Reimann sheets furthest to the right. The capillary-dilational resonance which was visible in figure 6-24 is hidden the the cluster of three sheets in the center of the plot. Both resonances are visible in the

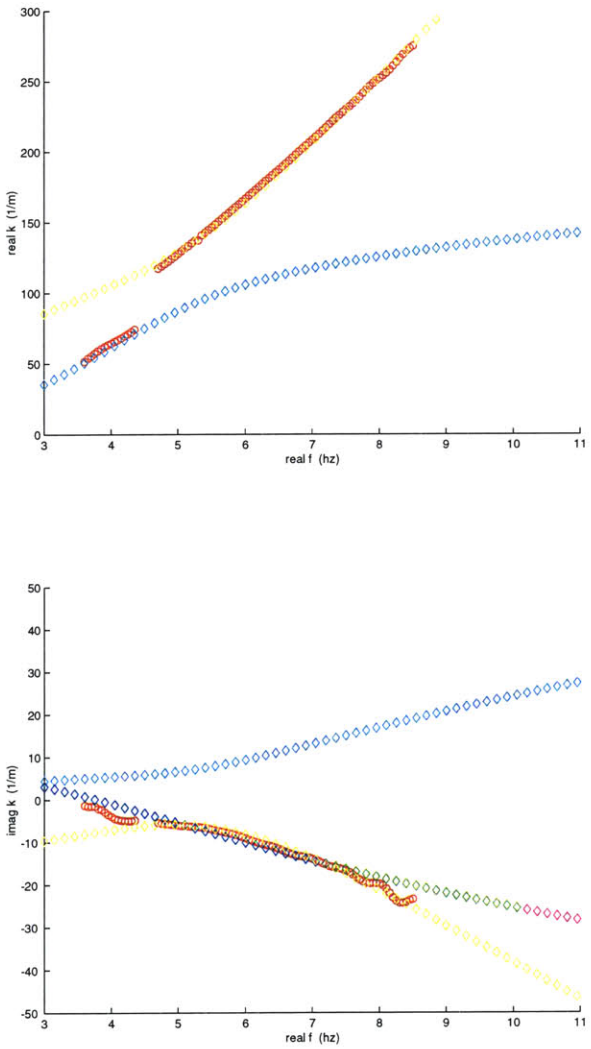

Figure 6-26: Match of the solution space to data below 4.3 hertz and above 4.7 hertz.

lower plot. Capillary-dilational resonances are visible at the ends of the small oblong opening between the two most left hand sheets. Gravity-capillary resonance can be seen at the top of the plot where the two outermost sheets stretch together. The three innermost sheets cross over the neighboorhood of resonance, partially obscuring the

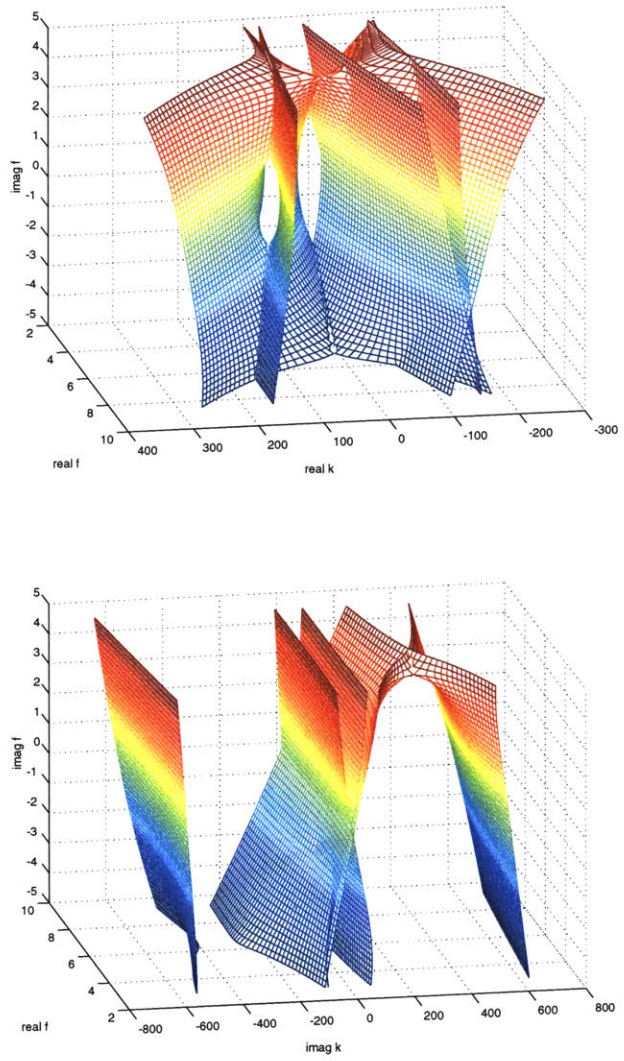

Figure 6-27: Two projections of the dispersion relation solution space showing gravity-capillary and capillary-dilational resonances.

view.

The curvature of the space due to gravity-capillary resonance is small near $\mathrm{Im}(f) = 0.2$ hertz, having virtually no effect on the damping coefficient. The typical effect of

this resonance is to cause an inflection point in the wave number curve and thus a dip in the group velocity near this frequency. While this reduction in group velocity should translate into a small dip in the wave number (related to energy) spectrum, it is unlikely to cause such a large effect as we see in the data.

Gravity-capillary resonance is also predicted for pure water. If this resonance would cause a large dip in a water wave energy spectrum, we would expect to see it, and yet in the data of Hühnerfuss (1981) shown in figure 6-28, we see only a small

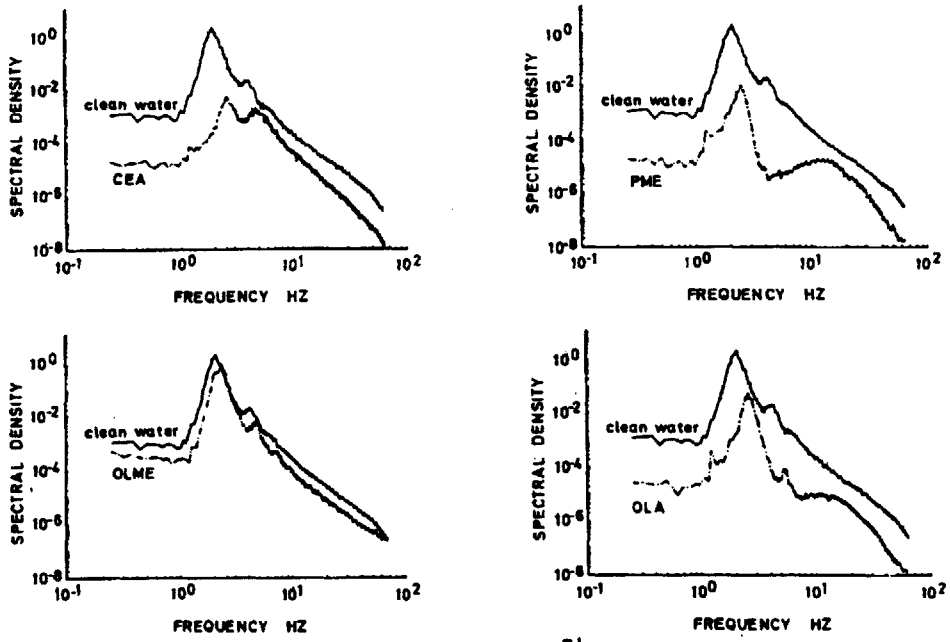

Fig. 1. Wind wave spectra (wind speed U = 8 ms^{-1}, fetch about 16 m, degrees of freedom 66) of a clean water surface (solid lines), and in the presence of a hexadecanol (CEA), hexadecanoic acid methyl ester (PME), 9-octadecenoic acid methyl ester, Z-isomer (OLME), and 9-octadecen-1-ol, Z-isomer (OLA) surface film.

Figure 6-28: Wind-wave spectra from a study by Hühnerfuss *et al.* , 1981. Each figure shows the measured spectra for water compared to that of a surfactant film spread upon the water.

dip near 4 hertz for the water spectra - the large dips in Hühnerfuss' data are not apparent until a surfactant has been spread upon the surface.

If the large dip in the wave slope spectrum is not entirely due to gravity-capillary resonance, then there must be another cause. If we look at figure 6-29 where the roots to the dispersion relation are shown for a transect at $\mathrm{Im}(f) = 0.0$ hertz, we see that

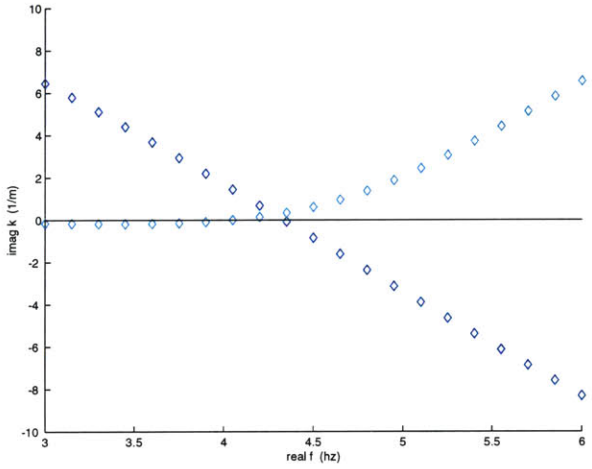

Figure 6-29: The gravity mode going unstable near 4.25 hertz.

the gravity mode, marked in cyan, crosses the real wave number axis around 4.3 hertz and goes unstable. (Recall that, for waves travelling in the $-x$ direction represented by phase $kx + \omega t$, a value of $\mathrm{Im}(k) > 0$ is unbounded in $-x$ and, therefore, unstable.)

Somewhere between 4.3 and 4.7 hertz, the primary mode of energy transport switched from the cyan root to the yellow root of the dispersion relation in figures 6-26 and 6-29. The most likely explanation is that it happened when the cyan root went unstable. This would offer one possible explanation for the sudden drop in the wave slope spectrum beginning at 4.3 hertz - the gravity mode goes unstable and the primary mode of energy transport is now the (yellow) capillary mode. As the total energy is split between the capillary and dilational modes, the transverse waves measured experimentally are smaller - they have less energy.

At this point, it might be helpful to identify the various wave modes. Figure 6-30 shows the damping coefficients of three of the five roots calculated both for the match of the inverse method to the data with $\epsilon_o = 0.0513$ kg s^{-2} marked by

diamonds and with $\epsilon_o = 0.06$ kg s^{-2} marked by hexagons. The tricolored root is a dilational mode - this can be seen by the change in it's value for a change in ϵ_o - a change in it's dependence on elasticity. The same can be said for the yellow root for frequencies less than about 7 hertz and the cyan root for frequencies above about 4.5 hertz. The yellow and cyan roots are forming an avoided crossing around 5 hertz with the dilational character of one root "jumping" to the other across the intervening space. This is occurring because these roots lie on a transect between two the two capillary-dilational root coalescence points as seen in figure 6-24. The other parts of the yellow and cyan curves, cyan below 4.5 hertz and yellow above 7 hertz have a gravity-capillary character. The cyan curve below 4.5 hertz behaves asymptotically as a gravity root and the yellow curve above 7 hertz asymptotically as a capillary root. Again, the jump between these curves occurs because the transect they lie on is between the two capillary-dilational root coalescence points. The gravity and capillary curves for part of the two Riemann sheets corresponding to the gravity and capillary modes which resonate near $4.2(1 \pm i)$ hertz.

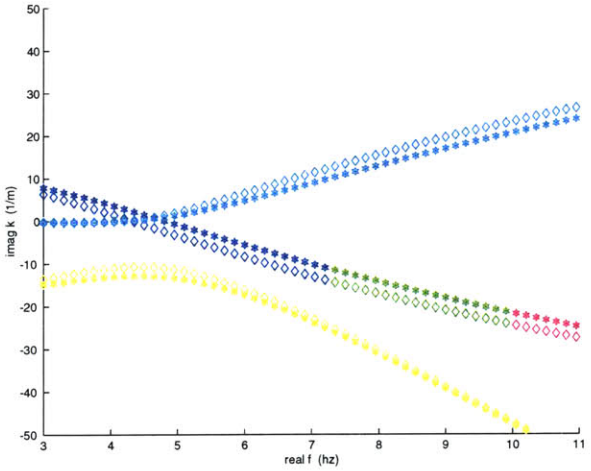

Figure 6-30: Change of the positions of the roots of the dispersion relation for variation of elasticity. The portions of the roots whose positions change are identified as dilational while those which do not are identified as gravitational and capillary.

So, we have a gravity-dilational root (cyan) which goes unstable near 4.25 hertz

and a dilational-capillary root (yellow) which is always stable. The experimental data, follows the gravity portion of the gravity-dilational root to around 4.3 hertz, then jumps to follow the capillary portion of the the dilational-capillary root above 4.7 hertz. In other words, we see a transverse displacement when the gravity mode is present below 4.3 hertz and a smaller transverse displacement when the capillary mode is present above 4.7 hertz - hence the large dip in the wave slope spectrum between 4.3 and 4.7 hertz.

This brings us to an interesting point. We see modulation in the wave slope data. However, above 4.25 hertz, the solution space only has one stable mode for our rheological conditions - the capillary mode. For most of our data range the dilational mode is unstable, $\mathrm{Im}(k) > 0$. In order for there to be modulation, two modes must exist - this implies that the unstable dilational mode is present in our experiments. For an unstable mode to grow in space, it needs an energy source. The only source available is the capillary mode. In this case we would expect to see a rapidly decaying capillary mode and a fairly constant or growing dilational mode. If we examine figure 6-31, this is exactly what we do see. The wave slope spectrum damps rapidly at the higher end of the frequency spectrum, but the modulations do not.

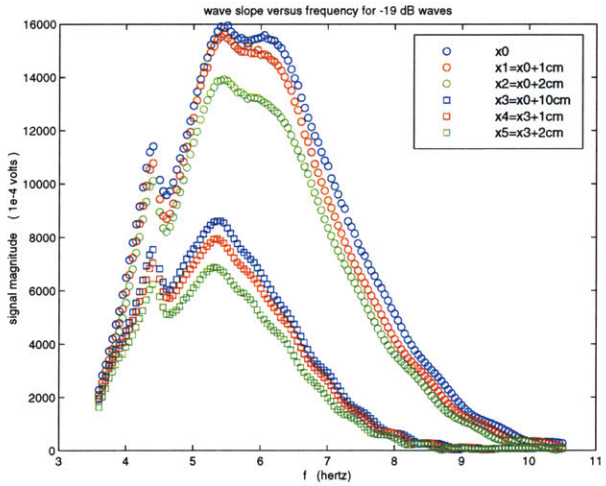

Figure 6-31: Wave slope spectra of Hercolube C at six tank locations. The figure was made for a wave maker power setting of -19dB.

The presence of an unstable dilational mode is quite surprising as it is generally accepted that the dilational mode is far more damped than the capillary mode. If this is, indeed, the proper interpretation of what is happening with the various wave modes, then it provides a starkly different vision of what happens to wind waves when there is a film upon open water. Given a film with similar rheology to the one we have just been studying, gravity-capillary waves would, upon encountering a film, to split their energy between a capillary and a dilational mode. The capillary mode would be more strongly damped than it would be upon open water. The dilational mode would bleed energy from the capillary mode until no energy was available, at which point the dilational waves must die out as well. This picture provides a much more general mechanism for energy decay than simply loss of energy from the capillary mode due to resonant wave interaction.

Chapter 7

Experimental measurements of resonance effects

7.1 Introduction

In chapter 4 we discussed three types of resonance effects: dips in the wave slope (energy) spectrum, peaks and troughs in the wave damping coefficient spectrum and dips in the wave group velocity. For certain rheological conditions we can expect to see two types of resonance in the 3 - 10 hertz range: gravity-capillary and capillary-dilational.

Finding a surfactant or bulk fluid with these rheological conditions, turned out to be a bit difficult. Section 4.3 allows us to estimate which sets of rheological parameters will yield root coalescence (resonance) near the real k and ω axes (wave number and frequency). Resonance near the real axes would provide the most experimentally amenable conditions to measuring resonance effects. Although there may be many surfactants whose rheology would give rise to wave mode resonance and although there are many reported values for rheological parameters in the literature, due to a paucity of published values of complete sets of surface tension, surface normal shear viscosity, surface dilational elasticity and surface apparent dilational viscosity, $\sigma_o, \sigma', \epsilon_o$, and ϵ', respectively, in the 3-10 hertz range, it was unclear which surfactants would provide us with the most experimentally amenable conditions to measuring

resonance. Thus the only two-fluid systems we knew for sure to have experimentally demonstrable resonance effects were those published by Bock (1987) for Hercolube C and by Hühnerfuss for palmitic acid methyl ester and oleyl alchohol.

It was hoped that the application of the inverse method to measurements of palmitic and myristic acids might yield the correct conditions for an experimental demonstration of resonance. As will be seen in sections 7.2.1 and 7.2.2, estimation of the group velocity from wavenumber measurements yielded an evidence of both gravity-capillary and capillary-dilational resonances, however this indication was not strong. This was likely due to another difficulty in measuring resonance effects: extricating the effect of wave mode modulation from the often subtle appearance of dips in the group velocity and damping coefficients due to capillary-dilational resonance. For this reason only a very strong capillary-dilational resonance event will be clearly demonstrable by a dip in the group velocity. This difficulty is not much of a concern for gravity-capillary resonance. This resonance is strong and appears regularly in measurements of the group speed of water waves.

The strongest demonstration of capillary-dilational resonance at a viscoelastic interface is seen in our measurements of wave slope spectra and damping coefficient for Hercolube C will be seen section 7.2.3. Dips in the group velocity for these waves are, like those of the curves for palmitic and myristic acids, not strong and clearly affected by the modulation of the amplitude and phase measurements.

7.2 Measurements

7.2.1 Palmitic acid

Group velocity

The following plots of group velocity versus frequency were calculated using the method outlined in section 5.3.4 from the experimental wave number versus frequency curves obtained for palmitic acid shown in section 5.5.1.

All of these figures show dips near 4 and 7 hertz where we would expect gravity-

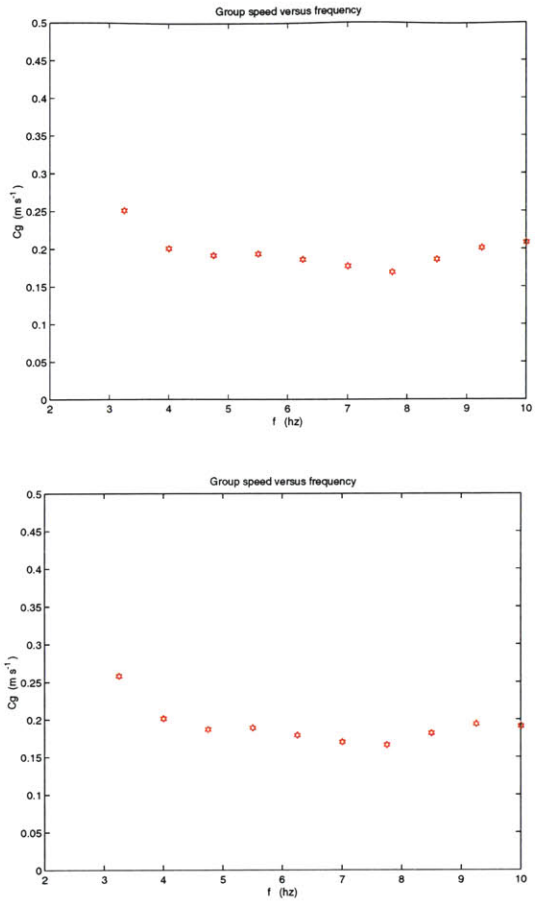

Figure 7-1: Group velocity, Cg, versus frequency, f, of capillary waves traveling on a 0.01 N HCl aqueous solution with a palmitic acid monolayer of concentrations 52 and 39 square A.U. per molecule, respectively.

capillary and capillary-dilational modal resonances to be. As any modulation effects in the palmitic acid wave number data were very small, it is possible that theses dips do, indeed, indicate gravity-capillary and capillary-dilational resonances.

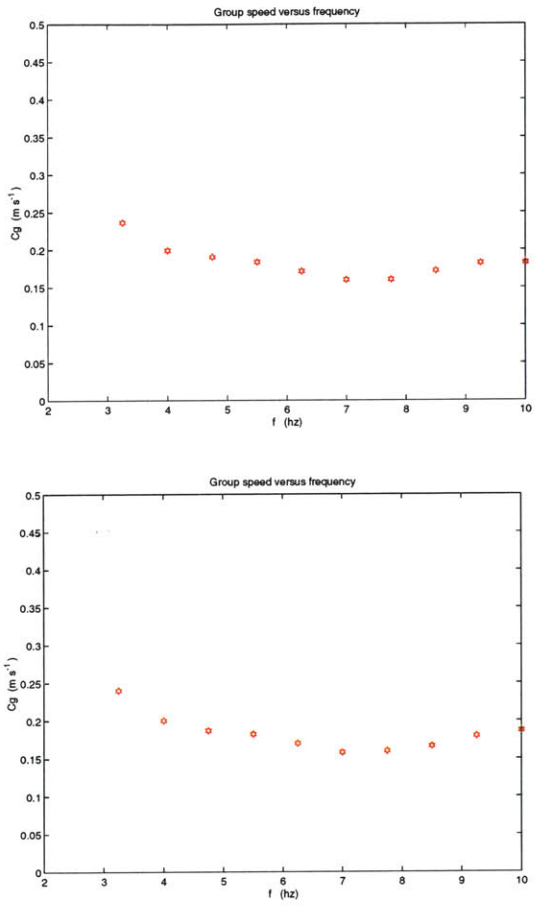

Figure 7-2: Group velocity, Cg, versus frequency, f, of capillary waves traveling on a 0.01 N HCl aqueous solution with a palmitic acid monolayer of concentrations 31 and 25 square A.U. per molecule, respectively.

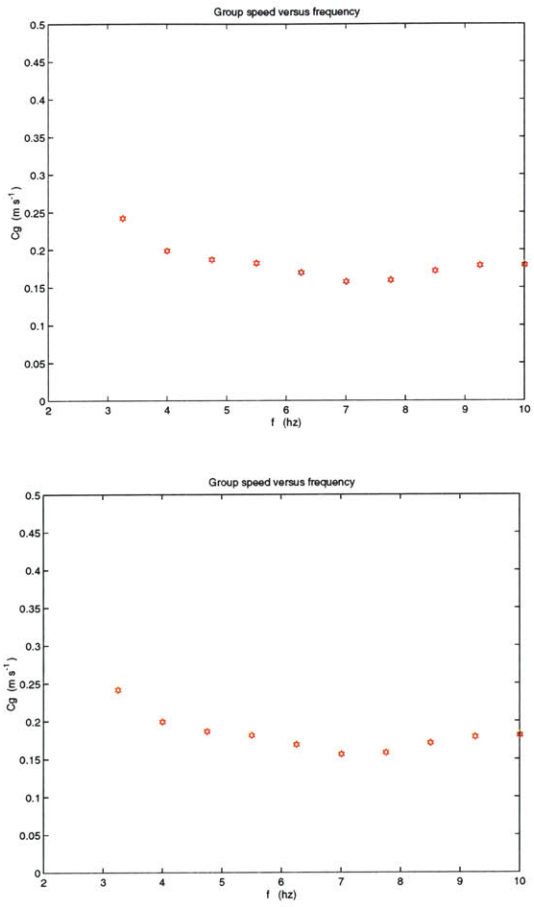

Figure 7-3: Group velocity, Cg, versus frequency, f, of capillary waves traveling on a 0.01 N HCl aqueous solution with a palmitic acid monolayer of concentrations 19 and 15 square A.U. per molecule, respectively.

7.2.2 Myristic acid

Group velocity

The following plots of group velocity versus frequency were calculated using the method outlined in section 5.3.4 from the experimental wave number versus frequency curves obtained for palmitic acid shown in section 5.5.2.

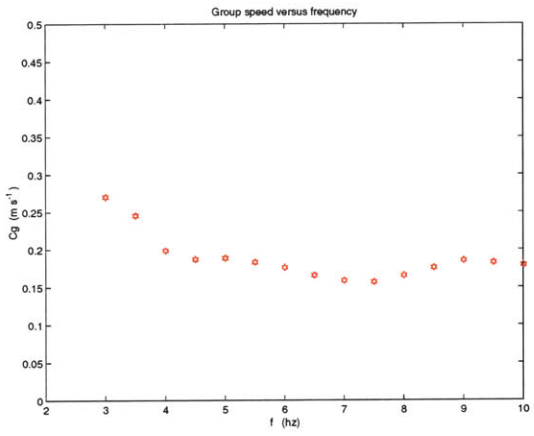

Figure 7-4: Group velocity, Cg, versus frequency, f, of capillary waves traveling on a 0.01 N HCl aqueous solution with a myristic acid monolayer of concentration 36 square A.U. per molecule.

All of these figures show dips near 4 and 7.5 hertz where we would expect gravity-capillary and capillary-dilational modal resonances to be. As, like the palmitic acid data, any modulation effects in the myristic acid wave number data were very small, it is possible that theses dips do, indeed, indicate gravity-capillary and capillary-dilational resonances.

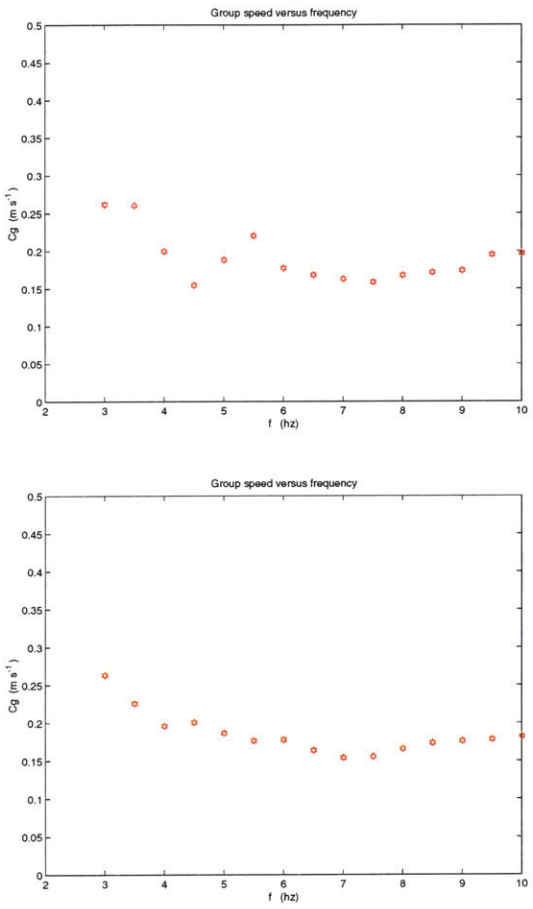

Figure 7-5: Group velocity, Cg, versus frequency, f, of capillary waves traveling on a 0.01 N HCl aqueous solution with a myristic acid monolayer of concentrations 29 and 21 square A.U. per molecule, respectively.

7.2.3 Hercolube C

From the numerical studies in section 4.3, we expected to see evidence of gravity–capillary resonance near 4 hertz and capillary–dilational resonance somewhere between 3 and 8 hertz.

Wave slope spectra

The wave slope spectra of the Hercolube C measurements show the effect capillary-dilational resonance quite clearly near 5.4 hertz. As described in section 6.5.3, they also show the effect of the gravity mode going unstable around 4.3 hertz and the transition of energy transport to the capillary mode - an effect of gravity–capillary resonance.

Figures 7-6 and 7-7 show, at six locations in the tank, the spectra resulting from a single power setting of the wave maker.

Figure 7-8 shows spectra taken at four separate temperatures, 23, 23.5, 17.5 and 15.5° C. We are able to see that lowering the temperature alters the rheological conditions and that this reduces the appearance of the effect of capillary–dilational resonance near 5.4 hertz on the spectrum. Gravity–capillary resonance and the switch from the gravity mode to the capillary mode as the primary mode of energy transport around 4.3 hertz is much less affected by changes in temperature.

Damping coefficient

It is unclear whether the small peak in the damping coefficient seen in figure 7-9 is due to ravity-capillary resonance or energy bifurcation. In either case, this peak corresponds to a reduction in the damping coefficient in the measured transverse wave mode. Capillary-dilational resonance is a much more subtle effect occurring near 5.4 hertz. This resonance is apparent only by the inflection point in the curve at this frequency. The change in general curvature at this location is more easily seen in figure (7-10).

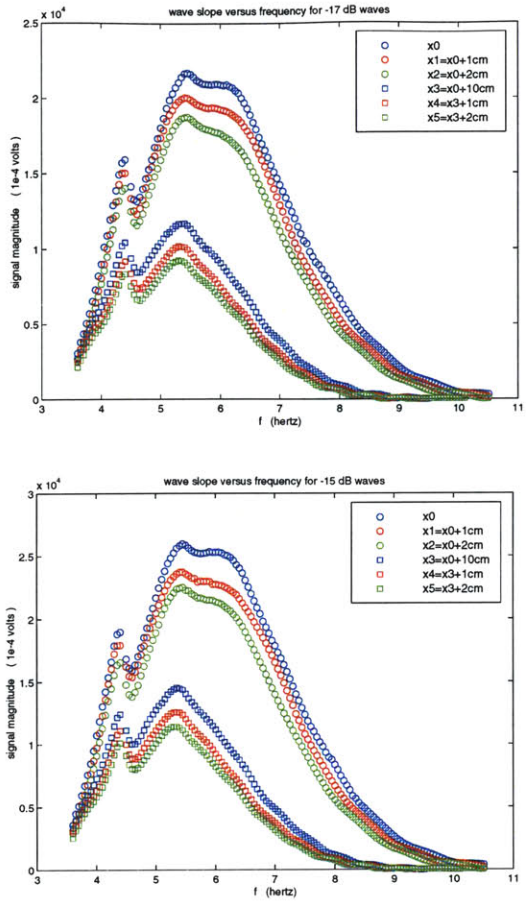

Figure 7-6: Wave slope spectra of Hercolube C at six tank locations. The upper and lower figures were made for wave maker power setting of -15 dB and -17dB, respectively.

Group velocity

The two resonances are not apparent in the curve of group velocity versus frequency shown in figure 7-11. The effects of wave mode modulation are too strong for the subtle effect of a dip in the group velocity to be successfully extracted.

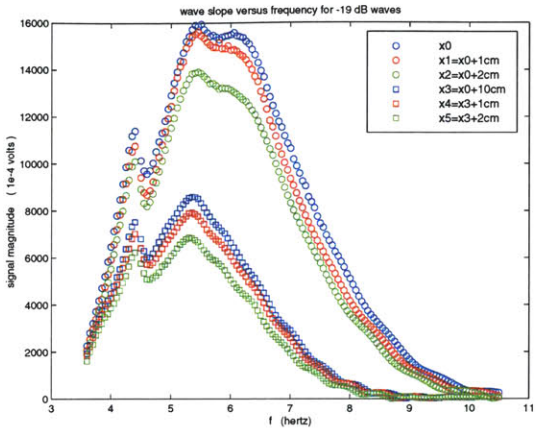

Figure 7-7: Wave slope spectra of Hercolube C at six tank locations. The figure was made for a wave maker power setting of -19dB.

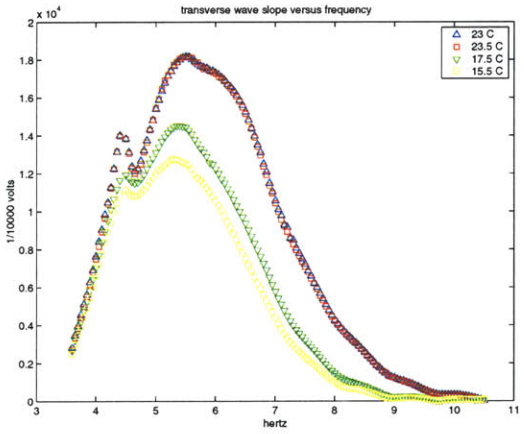

Figure 7-8: Wave slope versus frequency data taken at 23, 23.5, 17.5 and 15.5° C.

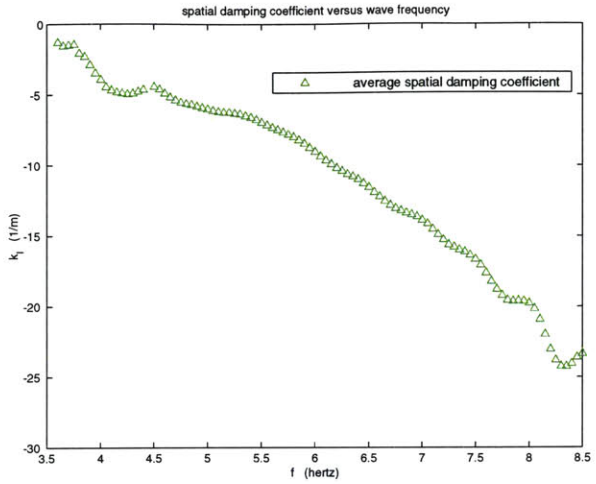

Figure 7-9: The average calculated damping coefficient versus frequency for Hercolube C.

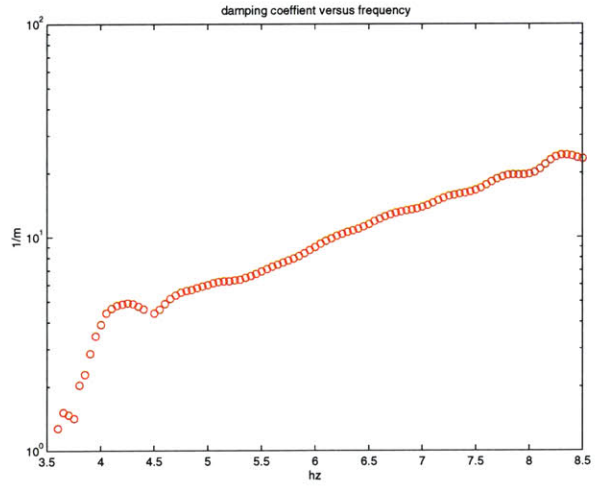

Figure 7-10: Semilog plot of the absolute value of the average calculated damping coefficient versus frequency for Hercolube C.

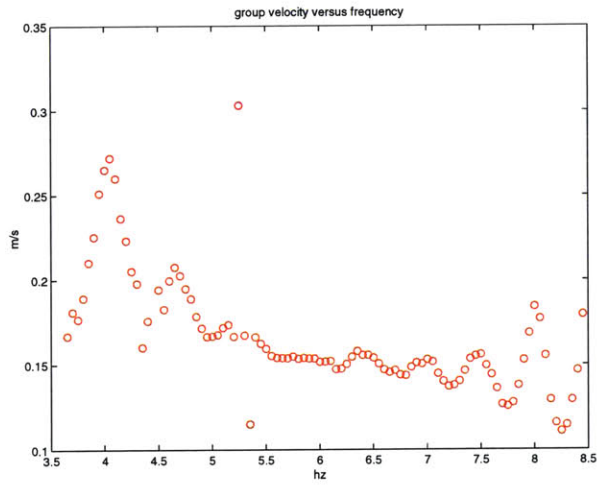

Figure 7-11: Group velocity calculated from wave number measurements.

Chapter 8

Conclusions

This thesis was a study of first order resonance between gravity, capillary and dilational wave modes occurring at a visco-elastic interface between two fluids, described by a single linear dispersion relation. In it, we described resonance as coalescence of the roots of the dispersion relation in complex frequency and wave number space and used this description to explain numerical and experimental resonance phenomena noted in previous studies.

We classified the roots of the dispersion relation as primarily gravity, capillary or dilational modes. These roots appeared as Reimann sheets when we displayed the dispersion relation solution space in parameter space.

We numerically determined the dependence on interfacial rheology of root coalescence (resonance) and the boundaries of spatial stability of the modes and then used these diagnostic tools to characterize the conditions for both gravity-capillary and capillary-dilational modal resonances. It was determined that for a wide variety of typical rheological conditions for naturally occuring surfactants gravity–capillary resonance should occur in the neighborhood of 4 hertz and that capillary–dilational resonance might occur anywhere between 3 and 8 hertz.

We developed an inverse method from which interfacial rheological parameters can be determined from experimental measurements of wave number, frequency and spatial damping coefficient. We used this tool to construct the dispersion relation solution space corresponding to experimental conditions a with which, together with

the classification of the roots of the dispersion relation, we would be able to interpret the experimental results. We tested the inverse method's ability to obtain the correct rheological parameters on noisy simulated data sets and then applied it to published experimental data sets.

We designed an experimental set-up to measure wave number, spatial damping coefficient, and wave slope data for a 3 – 10 hertz frequency range of transverse and longitudinal waves in a clean enclosed flume. We used kimball-mounted lasers whose beams passed through optical glass in the tank and lid to capture transverse wave motion. We used a balance and Wilhelmy plate to measure in-situ surface tension. The experimental conditions included waves traveling on fatty acid monolayers on aqueous solutions and also waves traveling on a visco-elastic fluid at a variety of temperatures.

Analyzing the experimental data, we demonstrated the effects of modulation of one wave mode on another. We obtained the rheological parameters for these experimental systems by the inverse method. We used the inverse method to construct the dispersion relation solution space corresponding to the experimental conditions. We used the diagnostic tools for root classification, spatial stability together with the graphical representation of the dispersion relation solution space found from the inverse method to understand the physics underlying our experiments.

We demonstrated resonance phenomena experimentally with the wave data from the visco-elastic fluid and confirmed this resonance numerically: gravity – capillary resonance near 4.2 hertz and capillary – dilational resonance near 5.3 hertz as predicted.

Appendix A

Description of numerical codes and methods used throughout thesis

A.1 Signal processing

To compare the data independently sampled by the lock-in amplifier to the MAG and PHA data it calculates from the analog signal, I wrote a simple signal processing program. This program takes the fast fourier transform of the sinusoidal wave slope signal obtained from each position sensing diode (PSD). The resulting spectra is filtered by a variable width window and the magnitude and phase of the signal estimated from the inter-window spectral data.

A.2 Description of the inverse method

A.2.1 Flow chart

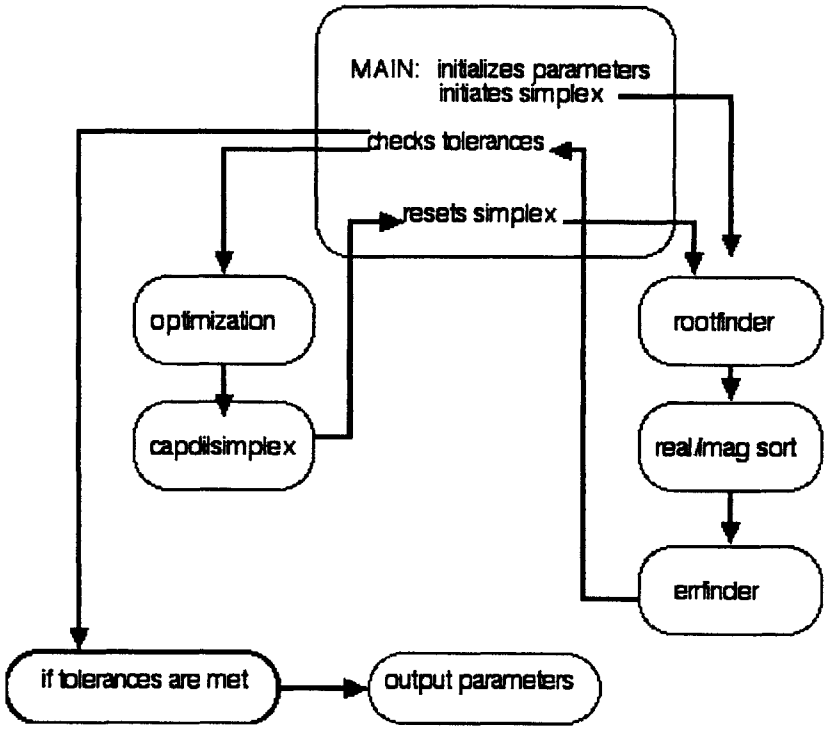

Figure A-1: Flow chart of functions of inverse method program

A.2.2 Main program body

At the beginning of this program, values are set for any parameters which are not being calculated by the inverse method and the data being matched by the inverse method is inputted. The parameters and data are then non-dimensionalized as a non-dimensional form of the dispersion relation will be used in the subsequent programs.

The simplex is initialized. The simplex is a matrix of non-dimensional values corresponding to the non-parameters the inverse method is searching for. These values are initialized to encompass the entire range of possible parameter values. The values in this simplex will be subsequently optimized until they converge upon the set of values which provides the best match of the solution space to the data.

Roots of the dispersion relation are calculated via the program *rootfinder* and an error condition is found for each of the roots via the program *errfinder*. The main program then checks the tolerances for these error conditions, if the tolerances are not met, then the program enters a *while* loop in which it begins to optimize the simplex via *optimizationprog*. Because the simplex method is robust but not adaptive, it is necessary to reinitialize the simplex to new values (keeping the best value from the previous optimization) and run through the optimization scheme until the change in the values satisfies a set tolerance. In this way, the inverse method converges upon the best answer. Tests with noisy numerical data sets show that the inverse method converges unambiguously to the correct answer with no dependence on the initialization of the simplex other than it be adequate to encompass the entire range of parameters.

A.2.3 Rootfinder

This program calculates roots of a non-dimensionalized version of the dispersion relation. In it's fully expanded form, the dispersion relation has 10 roots in non-dimensional wave number , k^*. Five of the roots are spurious and result from squaring the term

$$m = \left(k^2 + \frac{i\omega\rho}{\mu}\right)^{1/2} \tag{A.1}$$

in the dispersion relation. To separate the spurious from the good roots, positive and negatives values of non-dimensional m, m^*, are calculated for each of the roots in k^* and the two values are put back into the dispersion relation. If the positive value of m^* together with k^* satisfies the dispersion relation better than the negative value of m^* together with k^*, then the root is good, if not, it is spurious. Good roots must satisfy the condition that $m > 0$.

Once the five good roots in k^* have been ascertained, they are sorted in ascending order by either their real or their imaginary parts. This will be useful later when making plots of the solution space.

An option for discarding non-physical $k_R < 0$ and unstable $k_I > 0$ roots exists in this program.

A.2.4 Errfinder

There are several error schemes used in the errfinder algorithm - one for matching wave number data, one for matching damping coefficient data and another for matching both.

The schemes are are simple and merely calculated the percent different of the real, imaginary or real and imaginary parts of each root to each data point at that data point's frequency. The root contributing the minimum error is saved and all of these minimum errors summed to give an error index for the optimization scheme.

A.2.5 Optimizationprog

The optimization program is the heart of the inverse method. This program varies the values of the simplex, calls the rootfinder and errfinder programs and checks how well the variation went. This program internally checks tolerances for each optimization run (the run between reinitializations of the simplex). This program is based on the simplex method published in Press *et al.* , 1995.

A.2.6 Capdilsimplex

This subroutine to the optimization program replaces the simplex values with largest error and sees if the new values have a smaller error.

A.3 Noisy simulated data and the inverse method

To test the inverse method we used noisy simulated data. We examined the robustness of the inverse method by applying it to two portions of the data set, the first subset, labeled 20:40, near a resonance event, the second subset, labeled 50:70, at a higher frequency range. Three different error schemes were used to determine goodness

	σ_S	
Data Set: Parameters	20:40	50:70
$\sigma_s(k_I)$	7.04	5.44
$\sigma_s(k_R)$	7.27	7.05

Table A.1: This table gives the values of the standard deviations for both real and imaginary k data, $\sigma_s(k_R)$, and $\sigma_s(k_I)$, for the data set subranges 20:40 and 50:70.

of fit of the final answer. These error schemes considered wave number, k_R, spatial damping, k_I, and both wave number and spatial damping coefficient data respectively. These results are presented in section 6.3.

The challenge of making a comparison between the three error schemes for the two portions of the data set was that the conditions of the data must be comparable. The noise to signal ratio (NSR) must be the same for both the wave number and spatial damping data for both the 20:40 and the 50:70 frequency ranges of the data. This meant that, in reality, different amounts of noise must be added to both the wave number and damping coefficient data sets for each NSR for both of the frequency ranges.

The data sets were created in Matlab in the the following manner. A simulated data set of wave number, k_R, and spatial damping coefficient, k_I, was created for $\epsilon_0 = 30.0 \times 10^{-3}$ kg/s^2 and $\sigma_0 = 70.0 \times 10^{-3}$ kg/s^2, $\rho = 1024$ kg/m^3 and $\mu = 1.1264 \times 10^{-3}$ kg. The standard deviations, σ_S for both k_R and k_I were calculated for each of the data set subranges 20:40 and 50:70. These are given in table A.1.

Next, noise was manufactured using Matlab's random number generator, RANDN, which generates a matrix of random numbers with mean zero and variance one. The standard deviation of the noise, σ_N, was calculated and, from this, the

$$NSR = \frac{\sigma_N^2}{\sigma_S^2}. \tag{A.2}$$

To modify the standard deviation of the noise, and thus the NSR, the noise was

	k (1/m)	
Data Set: Parameters	20:40	50:70
$\overline{k_I}$	-31.62	-61.30
$\overline{k_R}$	89.20	126.14

Table A.2: This table gives the values of the mean values for both real and imaginary k data for the

weighted by a factor, n, so that

$$\sigma_N = \sigma(nR) \tag{A.3}$$

where R is the random number set. Three noise to signal ratios were examined, 0.056, 0.084 and 0.112. To produce the same NSR for each of the two data curves k_R and k_I, and two data subranges, 20:40 and 50:70, twelve different values of n were applied to the random number set. The modified random number sets were then added to the simulated data, producing the twelve noisy data sets used for analysis of the inverse method.

The sensitivity index,

$$SI = \frac{E_Q/Q}{\sigma_N/\overline{k}} = \frac{\%error}{\sigma_N/\overline{k}} \tag{A.4}$$

was calculated with

$$\sigma_N/\overline{k} = \sigma_N/\overline{k_I} \tag{A.5}$$

$$\sigma_N/\overline{k} = \sigma_N/\overline{k_R} \tag{A.6}$$

$$\sigma_N/\overline{k} = \sqrt{\left(\sigma_N/\overline{k_I}\right)^2 + \left(\sigma_N/\overline{k_R}\right)^2} \tag{A.7}$$

for each of the three error schemes with the following values:

A.4 Resonance

To find the combinations of rheological and wave characteristic parameters for which modal resonance occurs, the following criteria were applied:

$$\Delta = 0 \tag{A.8}$$

$$\frac{\partial \Delta}{\partial k} = 0 \tag{A.9}$$

where Δ indicates the dispersion relation and k is the wave number.

These caculations use two nested programs. Both programs used non-dimensionalized versions of the two above criteria to reduce the number of variables which must be searched to find all of the combinations of rheological and physical parameters resulting in wave modal resonance.

The outer program looped through large ranges of each of the non-dimensional parameters. Using a range of the wavenumber, k as an input parameter, it calculated the roots (all in ω) of the second criterion above, subjecting them to all of the physicality, stability and sorting criteria of the rootfinder algorithm. These roots (in ω) were then used as the input to the second program. This program calculated the roots (all in k) of the first criterion above and compared these roots to the values of k inputed into the outer program. When the roots matched, the non-dimensional parameters were dimensionalized and the dimensional parameters stored.

A.5 Stability

A heuristic method was used to determine which of the 81 sets of non-dimensional parameters were most helpful in describing the bounds of stability of the roots of the dispersion relation. The dispersion relation was non-dimensionalized repeatedly and expanded in Maple. Programs looped through the parameters sets and calculated the roots of the non-dimensional dispersion relation and counted the number of physical $k_R > 0$ and stable $k_I < 0$ roots. Color coded symbols of the number of stable roots were then plotted in three dimensional non-dimensional parameter space where they

could be evaluated for dependence on the axes parameters.

SYMBOLS LIST

Chapter 2

ρ density

v velocity

t time

p pressure

x, y, z principal directions of inertial reference frame

g gravity

ϕ potential

ψ divergence

A, B amplitudes

k wave number

m divergence vertical decay coefficient

ω frequency

ζ vertical displacement

ξ tangential displacement

E, S parameters

σ_D surface tension of deformed interface

κ surface tangential dilational viscosity

η_N surface normal shear viscosity

η surface tangential shear viscosity

A_e area

s arc length

σ_o static surface tension

$\sigma' = \eta_N$

$\sigma = \sigma_o + i\omega\sigma'$

ε_o dilational elasticity

ε'' relaxational elasticity

$\epsilon_o = \varepsilon_o$

ϵ' apparent dilational elasticity

$\epsilon = \epsilon_o + i\omega\epsilon'$

δR change in work done in displacing surface

δf change in surface area

p_{ij} viscous stress tensor

τ_{ij} interfacial stress tensor

δ_{ik} delta function

$\delta n \delta t$ area of interfacial element

μ, μ^* 1st and 2nd coefficients of bulk viscosity

Chapter 3

P_i non-dimensional parameters

DVE non-dimensional parameter: dilational viscous retardation to elastic propagation of energy

BVE non-dimensional parameter: bulk viscous retardation to elastic propagation of energy

BIE non-dimensional parameter: bulk inertial retardation to elastic propagation of energy

θ phase

Chapter 4

π parameters

α, β, γ coefficients

k_R wave number

k_I spatial damping coefficient

$k = k_R + ik_I$

ω_R frequency

ω_I temporal damping coefficient

$\omega = \omega_R + i\omega_I$

f frequency

T_d non-dimensional time factor

L_d non-dimensional length factor

λ wave length

Cg group velocity

F_o force

k_i spring constant

x_i displacement

m_i mass

δ_{st} static displacement

Chapter 5

C_i currents

I current

ν kinematic viscosity

T torque

R radius

$\dot{\gamma}$ angular velocity

H separation distance

ϕ phase

n, m winding numbers

x_i position

π pi

A_i amplitudes

m mass

L Wilhelmy plate length

A area

a_i coefficients

A, B amplitudes

α, β coefficients

M magnitude

k_i wave numbers

x_i positions

$\delta, \gamma, \epsilon, E$ parameters

Chapter 6

N noise

γ mapping constant

γ_N mapping constant with noise

SI sensitivity index

E_Q error in the estimate of Q

Q parameter

σ_N standard deviation of noise in signal

$\overline{k}$ mean value of data

θ phase of ϵ

π surface pressure

Appendix A

NSR noise to signal ratio

σ_S standard deviation of the signal

R random number set

n coefficient

REFERENCES

Adam, N.K , 1922. The Properties and Molecular Structure of Thin Films. Part III. Expanded Films, *Pro. Roy. Soc. Ser. A*, **101**, No. 713, 516-531.

Adam, N.K and Harding, J.B., 1932. The Structure of Surface Films. Part XVI. Surface Potential Measurements on Fatty Acids on Dilute Hydrochloric Acid, *Pro. Roy. Soc. Ser. A*, **138**, No. 835, 411–430.

Adam, N.K and Jessop, G, 1926. The Structure of Thin Films. Part VIII. Expanded Films, *Pro. Roy. Soc. Ser. A*, **112**, No. 761, 362-375.

Aitken, 1883. On the Effect of Oil on a Stormy Sea, *Pro. Roy. Soc. Edin.*, **xii**, 56–75.

Barger, W.R. 1991. A Review of Experimental Observations and Remaining Questions Concerning Formation, Persistence, and Disapppearance of Sea Slicks, NRL Report 9313.

Baus, M. 1982. Elastic moduli of a liquid-vapor interface, *J. chem. Phys.*, **76**, 2003–2009.

Bock, E.J., 1987. On Ripple Dynamics I. Microcomputer-aided measurement of ripple propagation, *J. Coll. Int. Sci.*, **119**, No. 2, 326–334.

Bock, E.J., 1989. On Ripple Dynamics IV. Linear Propagation of Plane-Wave Packets: Observation, *J. Coll. Int. Sci.*, **131**, No. 1, 38–46.

Boussinesq, M.J. 1913. *Ann. Chim. Phys.*, **29**, 349, 357, 364.

Brown, R.C., 1936. The ripple method of measuring surface tension, *Proc. Phys. Soc. Lond.*, **48**, 312–322.

Brown, R.C., 1936. A method of measuring the amplitude and damping of ripples, *Proc. Phys. Soc. Lond.*, **48**, 323–328.

Brown, S.J., Triantafyllou, M.S. and Yue, D.K.P., 2002. Complex analysis of resonance conditions for coupled capillary and dilational waves, *Pro. Roy. Soc. Ser. A*, **458**, 1167–1187.

Cini, R., Lombardini, P.P., Manfredi, and Cini, E., 1987. Ripples Damping Due to Monomolecular Films, *J. Coll. Int. Sci.*, **119**, No. 1, 74–80.

da Vinci, 1490. Scientific notes.

Dorrestein, R., 1951. *Proc. Kon. Ned. Akad. Wetensch., Ser. B*, **54**, 260.

Dorsey, N.E., 1897. The surface tension of water and of certain dilute acqueous solutions, determined by the method of ripples. I., Phys. Rev., **5**, 170–230.

Earnshaw, J.C. and McGivern, R.C., 1987. Photon correlation spectroscopy of thermal fluctuations of liquid surfaces, *J. Phys. D*, **20**, 82–92.

Earnshaw, J.C., McGivern, R.C. and Winch, P.J. 1988. Viscoelastic relaxation of insoluble monomolecular films, *J. Phys. France*, **49**, 1271–1293.

Earnshaw, J.C. and McLaughlin, A.C. 1991. Waves at liquid surfaces: coupled oscillators and mode mixing, *Proc. R. Soc. Lond. A*, **433**, 663–678.

Edwards, D.A., Brenner, H., and Wasan, D.T., 1991. *Interfacial Transport Processes and Rheology,* Butterworth-Heinemann: Boston, MA.

Franklin, B. 1774. *Phil. Trans.*, **64**, 445.

Frew, N.M., and Nelson, R.K., 1992. Isolation of Marine Microlayer Film Surfactants for ex Situ Study of Their Surface Physical and Chemical Properties *JGR*, **97**, No. C4, 5281–5290.

Frysinger, G.S., Asher, W.E., Korenowski, G.M., Barger, W.R., Klusty, M.A., Frew, N.M., and Nelson, R.K., 1992. Study of Ocean Slicks by Nonlinear Laser Processes 1. Second-Harmonic Generation, *JGR*, **97**, No. C4, 5253–5269.

Garrett, W.D. 1963. Capillary-wave damping by insoluble organic monolayers, *J. Coll. Sc.*, **18**, 798–801.

Garrett, W.D. 1967. Damping of capillary waves at the air-sea interface by organic surface-active material, *J. Mar. Res.*, **25**, 279–291.

Ghia, P.L., and Trivero, P., 1988. On the Vibration Modes of the Air-Water Interface in the Presence of Surface Films, *Il Nuovo Cimento*, **11 C**, No. 3, 305–315.

Giermanska-Kahn, J., Monroy, F., Langevin, D., 1999. Negative effective surface viscosities in insoluble fatty acid monolayers: Effect of phase transitions on dilational viscoelasticity, *Phys. Rev.* E, **60**, No. 6, 7163–7173.

Goodrich, F.C., 1961. The mathematical Theory of Capillarity, Part I–III, *Proc. R. Soc. Lond.* A, **260**, 481–488, 489–501, 502–509.

Goodrich, F.C., 1981. The theory of capillary excess viscosities, *Proc. R. Soc. Lond.*

A, **374**, 341–370.

Hansen, R.S. and Mann, A.A., 1964. Propagation characteristics of capillary ripples I. The theory of velocity dispersion and amplitude attenuation of plane capillary waves on viscoelastic films, *J. Applied Physics*, **35**, vol. 1, 152–158.

Høard, S. and Neuman, R., 1981. Laser Light-Scattering Measurements of Viscoelastic Monomolecular Films, *J. Coll. Int. Sci.*, **83**, No. 2, 315–334.

Høard, S. and Neuman, R., 1986. Viscosity of Monomolecular Films: A Laser Light-Scattering Study, *J. Coll. Int. Sci.*, **120**, No. 1, 15–29.

Hennenberg, M., Chu, X.-L., Sanfeld, A and Velarde, M.G., 1992. Transverse and Longitud inal Waves at the Air-Liquid Interface in the Presence of an Adsorption Barrier, *J. Coll. Int. Sci.*, **150**, No. 1, 7–21.

Hühnerfuss, H., Lange, P.A., and Walter, W., 1985. Relaxation Effects in Monolayers and Their Contribution to Water Wave Damping, *J. Coll. Int. Sci.*, **108**, No. 2, 430–441.

Jayalkshmi, Y., Ozanne, L., and Langevin, D., 1995. Viscoelasticity of Surfactant Monolayers, *J. Coll. Int. Sci.*, **170**, 358–366.

Kramer, L., 1971. Theory of Light Scattering from Fluctuations of Membranes and Monolayers, *J. Chem. Phys.*, **55**, no. 5, 2097–2105.

Lamb, H., 1932. *Hydrodynamics*, New York: Dover, 380.

Langevin, D., 1981. Light-Scattering Study of Monolayer Viscoelasticity, *J. Coll. Int. Sci.*, **80**, no. 2, 412–425.

Langevin, D. and Griesmar, C., 1980. Light-Scattering study of fatty acid monolayers, *J. Phys. D: Appl. Phys.*, **13**, 1189–1199.

Langmuir, I., 1917. The constitution and fundamental properties of solids and liquids II. Liquids, *J. Am. Chem. Soc.*, **39**, 1848–1906.

Laplace, P.S., 1806. *Mechanics Celestial*, **IV**, 685.

Levich, V.G., 1941. *Acta Physicochim.*, **41**, 307, 321.

Levich, G.G., 1962. *Physicochemical Hydrodynamics*, Engelwood Cliffs N.J. : Prentice-Hall, 372–394.

Liu, X. and Duncan, J.H., 2003. The effects of surfactants on spilling breaking waves,

, *Nature*, **421**, 520–523.

Lucassen, J., 1968. Longitudinal Capillary Waves, Parts 1 and 2, *Trans. Faraday Soc.*, **64**, 2221–2229; 2230–2235.

Lucassen, J. and Hansen, R. S., 1967. Damping of Waves on Monolayer-Covered Surfaces. II. Influence of Bulk-to-Surface Diffusional Interchange on Ripple Characteristics, *J. Coll. Int. Sci.*, **23**, 319–328.

Lucassen-Reynders, E.H., and Lucassen, J. 1969. Properties of capillary waves, *J. Coll. Int. Sci.*, **80**, 412–425.

Lucassen-Reynders, E.H., 1981. *Anionic Surfactants Physical Chemistry of Surfactant Action*, New York: M. Dekker Inc., 173–221.

Mann Jr., J. A. and Hansen, R.S., 1963. Propagation characteristics of capillary ripples, II. Instrumentation for measurement of ripple velocity and amplitude, *J. Coll. Sc.*, **18**, 757–771.

Mass, J.T. and Milgram, J.H., 1998. Dynamic behavior of natural sea surfactant films, *JGR*, **103**, *C8*, 15,695–15,715.

Peltzer, R.D., Griffin, O.M., Barger, W.R., and Kaiser, J.A.C., 1992. High-Resolution Measurement of Surface-Active Film Redistribution in Ship Wakes, *JGR*, *97*, No. C4, 5231–5252.

Plinius. AD 77. *Historia Naturalis*, Lib II, Cap. **103**.

Press, W.H., Teukolsky, S.A., Vetterling, W.T. and Flannery, B.P. 1995 *Numerical recipes in C*, Cambridge University Press, 408–412.

Scriven, L.E. 1960. *Chem. Eng. Sci.*, **12**, 98.

Shuleikin, 1933. *Physica Moria.*

Rao, S.S., 2004. *Mechanical Vibrations,* Upper Saddle River, New Jersey: Pearson Prentice Hall, 4th ed., 704.

Rednikov, A.Ye., Colinet, P., Velarde, M.G., and Legros, J.C., 1998. Two-layer Bénard-Marangoni instability and the limit of transverse and longitudinal waves, *Phys. Rev.* E, **57**, No. 3, 2872–2884.

Reynolds, O. 1880. On the Effect of Oil in destroying Waves on the Surface of Water, *Brit. Ass. Rept.*. [*Papers*, **i.**, 409.]

Sohl, C.H., Miyano, K. and Ketterson, J.B., 1978. Novel technique for dynamic surface tension and viscosity measurements at liquid-gas interfaces, *Rev. Sci. Instrum.*, **49**, *10*, 1464–1469.

Thompson, W. 1871. The influence of wind on waves supposed frictionless, *Phil. Mag.*, **42**, 368.

Thompson, W. 1871. On the Equilibrium of Vapour at a Curved Surface of Liquid, *Phil. Mag.*, **42**, No. 282, 448–452.

Triantafyllou, M.S. and Triantafyllou, G.S. 1991. Frequency Coalescence and Mode Localization Phenomena: A Geometric Theory, *J. Sound and Vibration,* **150**, 485–500.

van den Tempel, M., and Lucassen-Reynders, E.H. 1983. Relaxation Processes at Fluid Interfaces, *J. Coll. Int. Sci.*, **18**, 281–301.

van den Tempel, M., and van de Riet, R.P. 1965. J. Chem. Phys., **42**, 2769.

Wantke, K., Fruhner, H., Fang, J. and Lunkenheimer, K., 1998. Measurements of the Surface Elasticity in Medium Frequency Range Using the Oscillating Bubble Method, *J. Coll. Int. Sc.*, **208**, 34–48.

Watson, F.R., 1901. Surface tension at the interface of two liquids determined experimentally by the method of ripple waves, Phys. Rev., **12**, *5*, 257–278.

Wei, Y., and Wu, J., 1992. In Situ Measurements of Surface Tension, Wave Damping, and Wind Properties Modified by Natural Films, *J. Geophys. Res*, **97**, No. C4, 5307–5313.